Magnetic Nanoparticles for Targeted Cancer Theranostics

Zachary R. Stephen

A dissertation

submitted in partial fulfillment of the

requirements for the degree of

Doctor of Philosophy

University of Washington

2016

Reading Committee:

Miqin Zhang, Chair

James Park

Qifeng Zhang

Program Authorized to Offer Degree:

Materials Science and Engineering

University of Washington

Abstract

Magnetic Nanoparticles for Targeted Cancer Theranostics

Zachary R. Stephen

Chair of the Supervisory Committee:
Professor Miqin Zhang
Materials Science and Engineering

Nanotechnology has given scientists new tools for the development of advanced materials for the detection, diagnosis and treatment of disease. Superparamagnetic iron oxide nanoparticles (SPIONs) in particular have been extensively investigated as novel magnetic resonance imaging (MRI) contrast agents due to a combination of favorable superparamagnetic properties, biodegradability, and surface properties that allow modification for improved *in vivo* kinetics and multifunctionality. SPIONs favorable characteristics have further led to their investigation as promising theranostic agents, which combine imaging and therapeutic capabilities in a single nanovector. The combination of imaging and therapy could allow for real-time monitoring of drug delivery and the tailoring of treatment for individual patients with the promise of improved clinical outcomes for patients suffering from cancers such as glioblastoma (GBM). This dissertation is intended to address limitation of conventional clinical

cancer treatment including current cancer targeting limitations and poor pharmacokinetic of hydrophobic chemotherapeutics that lead to unacceptable side effects. First, SPIONs were coated with cross-linked, redox-responsive copolymers composed of chitosan and polyethylene glycol (PEG), functionalized with cancer targeting agent chlorotoxin (CTX), and modified with O^6-benzylguanine (BG), an O^6-methylguanine-DNA methyltransferase (MGMT) inhibitor to improve temozolomide based treatments of GBMs. It was found that CED of the BG loaded SPION were more tolerable than free drug and increased survival 3-fold over untreated animals in an intracranial GBM mouse model. Next, analogs of BG were evaluated for their inhibitory efficacy and modified to allow for polymerization on the SPION surface *via* hydrazone linkages to facilitate improved drug loading and controlled drug release. Finally, a new synthesis and functionalization strategy for theranostic agents is presented that demonstrated streamlined production, allowed for great control over the display of functional moieties on the SPION surface, increased batch to batch consistency, and provided improved magnetic properties.

TABLE OF CONTENTS

LIST OF FIGURES

LIST OF TABLES

ACKNOWLEDGEMENTS

I would like to express my sincere appreciation and thanks to my advisor, Miqin Zhang, for her mentorship, support and immense knowledge that has helped guide me through the pursuit of this degree. Her relentless passion and excitement for research was an inspiration through the inevitable challenges presented in my work. I would also like to thank my committee members, James Park, Qifeng Zhang, Richard Ellenbogen, and Qiuming Yu, how took time out of their busy schedule to provide valuable feedback and support on my graduate work. In addition, I would like to thank John Silber for his sound advice on research and on life.

I am indebted to all the Zhang lab members who contributed to this work. From the undergraduate volunteers who were always eager and full of questions to the graduate student and post docs who I worked alongside and provided invaluable guidance and support throughout my graduate career. Through my experience in the Zhang lab I have developed life-long friendships and laid groundwork for future collaborations.

A special thanks to my family whose unwavering support and unconditional love sustained me through my degree. Words cannot express how grateful I am to my mother-in-law, father-in-law and my parents, Jeannie and Mark for the sacrifices they have made on my behalf. Additionally, thank you to my siblings and their families for their support and for providing an escape from my PhD work when needed. At the end, I would like to express appreciation for my beloved wife, Heather, who endured through the trials of my graduate career yet never wavered in her suppor

1 Introduction and rationale

Worldwide, cancer remains the third leading cause of death behind heart and infection diseases with 14 million new cases and 8.2 million cancer related deaths reported in 2012.[1] In the United States alone, it's estimated that approximately 1.7 million new cases will be diagnosed and nearly 600,000 people will die of the disease in 2015.[2] These numbers have seen minimal improvement despite the vast amounts of research dedicated to better understand the biological causes of cancer, development of improved treatment strategies, and a national expenditure for cancer care in the United States of $125 billion in 2010 with an estimated increase to $156 billion by 2020.[2] It is clear that new approaches to treatment are needed to augment or replace traditional methods that typically comprise a combination of surgery, radiation, and chemotherapy. These approaches suffer from many limitations that include inadvertent removal of healthy tissue during surgery, ionizing radiation that can be a cause of cancer itself and systemic delivery of poorly water soluble chemotherapeutic drugs that lead to unacceptable side effects.

Many limitations of conventional cancer treatment can be addressed by the emerging field of nanomedicine. Advancements in nanomedicine have led to the development of theranostic nanoparticles (NPs) capable of providing diagnostic imaging and therapeutic capabilities in a single nanovector. Theranostic NPs are typically comprised of three main components; a core that in the case of superparamagnetic iron oxide NPs (SPIONs) provides contrast in magnetic resonance imaging (MRI), a surface coating that provides stability and biocompatibility, and functional moieties such as cancer targeting agents and therapeutic drugs. These components work in concert to provide real-time monitoring of drug delivery and improve

biodistribution profiles through increased circulation time of delivered therapeutics, protection from therapeutic degradation, and specific targeting of cancer cells.[3]

This research is expected to address current clinical limitation of cancer treatment with rationally designed theranostic SPIONs. This dissertation is organized as follows:

Chapter 1 provides an introduction to and rationale for this research.

Chapter 2 reviews the application of SPIONs in MR imaging and design parameters that need to be met for successful *in vivo* application. MRI basics and applicable imaging sequences for improved SPION contrast are discussed as well as the origins of SPIONs unique magnetic properties. Design parameters such as methods for core synthesis, polymer coating options and targeting strategies are discussed in regards to diagnostic MR imaging.

Chapter 3 reviews the application of SPIONs as theranostic agents. The importance of SPION quantitation for real-time monitoring of therapeutic delivery and methods for quantitation are reviewed. Therapeutic loading and release strategies for non-stimuli and stimuli responsive SPIONs is introduced.

Chapter 4 demonstrates application of the design parameters introduced in Chapters 2 and 3 for improved targeting and delivery of a therapeutic payload to increase *in vivo* survival in a brain tumor animal model.

Chapter 5 extends on the work presented in Chapter 4 by improving drug loading through polymerization of drug on the SPION surface and providing means for pH dependent controlled release to allow for less invasive administration of therapeutics.

Chapter 6 presents a new approach for streamlined production and functionalization of theranostic SPIONs that produces a highly effective transfection agent that demonstrates excellent magnetic properties.

Chapter 7 summarizes the work and provides conclusions.

2 Magnetic Nanoparticles for Medical MR Imaging

Magnetic resonance imaging (MRI) has become one of the most widely used and powerful tools for non-invasive clinical diagnosis due to its high soft tissue contrast, spatial resolution, and penetration depth[4]. In addition, images are acquired without the use of ionizing radiation or radiotracers which cause unwanted harmful side-effects. Considerable research in medical MR imaging is focused on the development of contrast agents that can provide better delineation between healthy and diseased tissue. Magnetic nanoparticles (MNPs) are a major class of nanoscale materials currently under extensive development for improved diagnosis of a wide range of diseases, including cancer,[5] cardiovascular disease[6] and neurological disease.[7] The nanoscale dimensions of MNPs give rise to unique magnetic properties and the ability to function on a cellular and molecular level.[8] It is the combination of these characteristics that make MNPs such promising contrast agents in MRI applications.

Among the various MNPs under investigation, superparamagnetic iron oxide nanoparticles (SPIONs) have attracted considerable interest due to their excellent magnetic properties, biocompatibility[9], and biodegradability.[10] While the *in vivo* applications of many nanoparticle-based contrast agents are hampered by toxicity concerns, SPIONs of several formulations have been approved by the Food and Drug Administration (FDA) as MRI contrast agents. These include Lumiren® for bowel imaging,[11] Feridex IV® for liver and spleen imaging,[12] and Combidex® for lymph node metastases imaging.[13] Recent advances in this field have further improved the magnetic and physiochemical properties of SPIONs,[14] broadening their potential clinical applications.

2.1 MRI and relaxation properties of SPIONs

2.1.1 Principles of MRI contrast

MRI employs a strong magnetic field that aligns the magnetic moments of protons in a sample producing an equilibrium magnetization along the z-axis (M_z) with a magnitude of M_0. A radio frequency (RF) pulse, at a resonance frequency capable of transferring energy to protons, rotates their magnetic moments off the z-axis in phase at an angle called the flip angle. The choice of flip angle depends on the imaging sequence applied but is generally to the transverse plane (xy-plane) causing a net magnetization of M_{xy}. Upon removal of the RF, the magnetic moments of protons relax to equilibrium.[4, 15] The time required for the magnetic moments to relax to the equilibrium state, which is broadly termed the relaxation time, is tissue-dependent.

MRI contrast in soft tissue is due to differences in proton density, spin-lattice relaxation time (T_1) and spin-spin relaxation time (T_2) of protons. T_1 is the time constant of the exponential recovery process of M_0 along the z-axis after an RF pulse. Protons that relax rapidly (short T_1) recover full magnetization along the z-axis and produce high signal intensities. For protons that relax more slowly (long T_1), full magnetization is not recovered before subsequent RF pulses and inherently produce less signal and the so called saturation effect. T_1 weighted images demonstrate anatomy well and are preferred when a clear image of structure is required.[15]

T_2 is the time constant of the exponential decay of transverse magnetization (M_{xy}) after an RF pulse. T_2 is related to the amount of time for precessing magnetic moments of protons to become randomly aligned in the xy-plane after an RF pulse, eventually resulting in a net magnetic moment of zero in the xy-plane. This dephasing process can be caused by a combination of local inhomogeneities in the magnetic field due to magnetic interactions of neighboring molecules and by macroscopic effects related to subtle variations in the external

magnetic field. When the dephasing time accounts for both intrinsic molecular interactions and extrinsic magnetic field inhomogeneities it is termed T_2*, and the produced images are considered to be T_2* weighted. Elimination of dephasing effects caused by extrinsic magnetic field inhomogeneities produces T_2 weighted images that account for molecular interactions alone. T_2 weighted images produce good pathological information as collection of abnormal fluid appear bright against the normal tissue background.[4]

Spin-echo (SE) pulse sequences are used to eliminate external magnetic field effects and can generate T_1 or T_2 weighted images based purely on molecular interactions.[4] This signal eliminates extrinsic effects and provides quantitative T_2 data for T_2 weighted images. In its most basic form, the spin-echo scans employ two RF pulses with flip angles of 90° and 180° that produce a spin echo. The 180° pulse serves to refocus the transverse magnetization, cancelling dephasing effects caused by inhomogeneities in the local magnetic field. The time between the application of the 90° pulse and the peak of the echo signal is termed echo time (TE). Both TE and the time gap between RF pulse repetitions (TR) are responsible for the type of image produced. T_1 weighted images are produced by selecting short TR (250–700 ms) and short TE (10–25 ms), while T_2 weighted images are produced by long TR (>2,000 ms) and long TE (>60 ms).[16]

In most tissue, intrinsic variation of T_1 and T_2 are small and often exogenous materials are employed clinically to enhance the contrast between the tissue of interest and the surrounding tissue. While nearly all MRI contrast agents affect both T_1 and T_2, usually the effects of contrast agents are more pronounced for either T_1 or T_2, leading to the categorization of these probes as T_1 or T_2 contrast agents. T_1 contrast agents are used to increase signal intensity providing positive contrast enhancement in T_1 weighted images, whereas, T_2 contrast agents decrease

signal intensity resulting in negative contrast enhancement in T_2 weighted images. Currently the most widely used clinical contrast agents are based on paramagnetic chelates of lanthanide metals such as gadolinium.[17] The presence of paramagnetic ions near water protons shortens their T_1 relaxation time through coordination with water molecules providing increased contrast. While gadolinium chelates are widely used, their short blood circulation times, poor detection sensitivity and toxicity concerns have led to the continued development of SPIONs for T_2 contrast enhancement.[18]

2.1.2 Magnetic properties of SPIONs

The unique magnetic properties of SPIONs arise from a combination of atomic composition, crystal structure, and size effects. Bulk iron oxide consists of both Fe^{2+} and Fe^{3+} atoms and exhibits ferromagnetic behavior. Large ferrimagnetic crystals of Fe_3O_4 are comprised of multiple magnetic domains that exhibit magnetic moments that are aligned within a domain, but between domains, magnetic moments are oriented in random directions.[19] Ferrimagnetic particles below a critical diameter consist of a single magnetic domain. The critical diameter defined as the size at which domain boundaries are no longer energetically favorable, is highly dependent on the anisotropy of the particles, and varies for differing materials.[20] For spherical magnetite iron oxide (Fe_3O_4) the critical diameter is approximately 70–150 nm.[20a, 20c, 21] When the diameter of spherical magnetite particles is reduced below approximately 20 nm,[20c] the thermal energy available at room temperature is greater than the magnetostatic energy well barrier. The magnetic dipole is free to fluctuate and as a consequence the particle acts like a paramagnetic $Fe^{(2+,3+)}$ atom. Since a nanoparticle comprises thousands of atoms, it is described as superparamagnetic; it combines the high magnetization of bulk magnetite with the paramagnetic nature of iron ions (**Figure 2-1**).

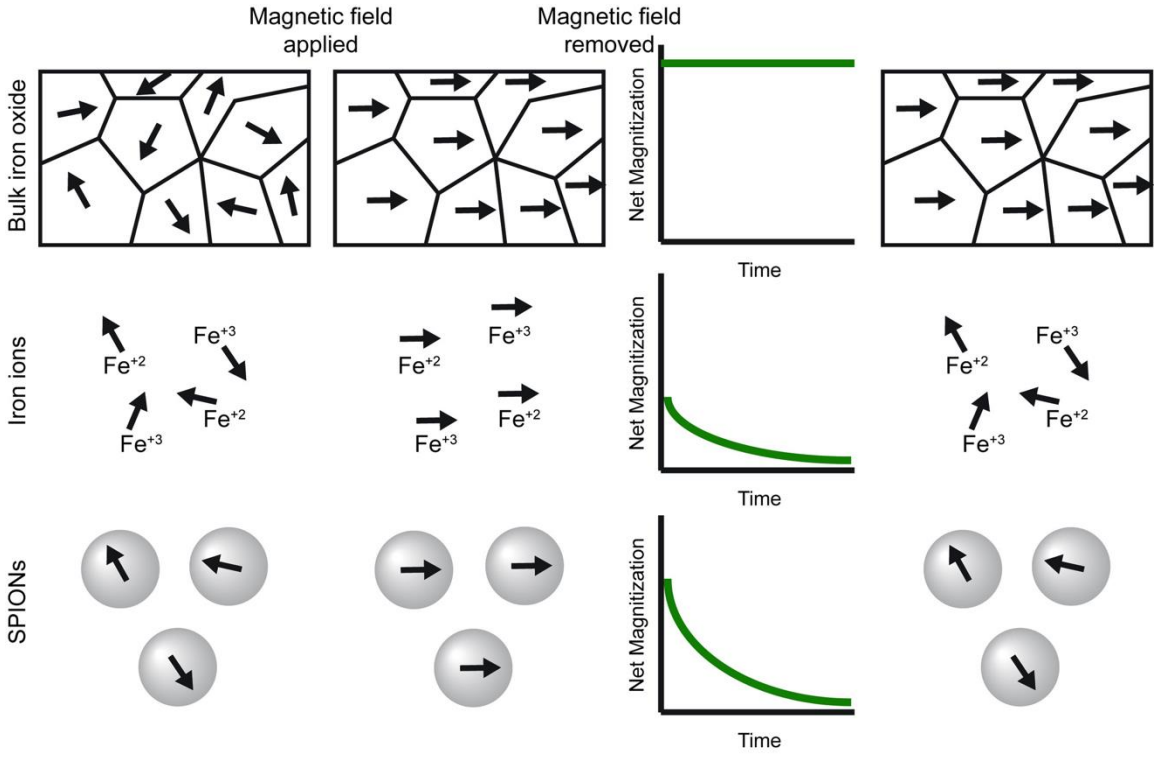

Figure 2-1. The effects of an external magnetic field on bulk magnetite (top), Fe ions (middle) and SPIONs (bottom). Before application of the magnetic field all magnetic moments are randomly aligned. Application of an external magnetic field aligns the moments along the z-axis of the magnetic field. The initial net magnetization of SPIONs is greater than Fe ions, but less than bulk magnetite. Upon removal of the magnetic field, the moments of bulk magnetite remain fixed along z-axis while both Fe ions and SPIONs magnetic moments relax over time to equilibrium.

2.1.3 Effects of SPIONs on MRI contrast

SPIONs act primarily to alter T_2 values of water protons surrounding the particle. When SPIONs present in tissue are subject to an external magnetic field the large magnetic moments of the particles align to create large heterogeneous field gradients through which water protons diffuse. The dipolar coupling between the magnetic moments of water protons and the magnetic moments of particles cause efficient spin dephasing and T_2 relaxation leading to a decrease in signal intensity.[22] The contrast provided by SPIONs in a T_2 weighted image is termed negative

contrast enhancement since areas with high concentrations of SPIONs appear dark on MR images.

Although SPIONs provide efficient shortening of T_2 and generate excellent contrast enhancement in tissue with longer T_2 characteristics, signal loss due to the presence of SPIONs can make it difficult to distinguish contrast enhancement in low signal body regions.[23] Senpan et al have recently reported a T_1 weighted colloidal cross-linked iron oxide nanoparticle comprised of oleate-coated magnetite particles within a cross-linked phospholipid nanoemulsion.[24] This formulation decreased T_2 effects and allowed positive T_1 weighted contrast detection at nanomolar concentrations. Additionally, ultrasmall superparamagnetic iron oxide (USPIO), i.e., SPIONs with core diameters less than 10 nm, are capable of producing positive contrast in T_1 weighted images[25] While positive T_1 contrast is possible with USPIO, this benefit is at the expense of their T_2 effects.[20a, 26]

Another approach that has recently been investigated is the addition of a gadolinium chelate on the polymer coating of SPIONs.[27] This dual contrast agent efficiently reduces both T_1 and T_2 relaxation times and achieves good contrast in mice for both T_1 and T_2 weighted images. This unique combination allows for the acquisition of both highly detailed T_1 weighted anatomical images and pathologically relevant T_2 weighted images with a single imaging nanoprobe. In addition, such a contrast probe could provide enhanced T_1 weighted imaging of brain tumors. Common clinical gadolinium chelates such as gadolinium diethylenetriamine penta-acetic acid (Gd-DTPA) cannot traverse the blood-brain barrier (BBB) without the use of invasive techniques,[28] limiting their application in brain tumor imaging. A significant advantage of SPIONs is their relatively large surface area which allows for efficient addition of biologically active moieties such as BBB-penetrating peptides for non-invasive brain tumor imaging. For

example, Veiseh et al have shown that SPIONs labeled with chlorotoxin (CTX) peptide, a targeting agent with high affinity for tumors of neuroectodermal origin through binding of the membrane-bound matrix metalloproteinase 2 complex, can pass the BBB and successfully target brain tumors in a transgenic mouse model.[29,30,31] Confirmation by MRI of the exclusion of Gd-DTPA from the parenchymal region signified that the BBB was not compromised before or after the administration of CTX labeled SPIONs, and highlights one advantage of SPIONs over commonly used Gd-chelates.

2.1.4 MRI acquisition methods for improved SPION detection

The detectability of SPIONs *in vivo* can be improved through synthesis techniques that enrich their magnetic properties and through enhanced MRI acquisition methods that improve SPION detection. Acquisition methods that achieve low detection limits will be essential as the next generation of SPIONs moves toward clinical application. Lower detection limits will allow for administration of lower SPION dosages while improving contrast. In addition to methods that improve the negative contrast enhancement inherent to traditional T_2 weighted methods, new techniques that generate positive contrast enhancement are currently being developed.

Historically, MRI acquisition methods for detection of SPIONs have been based on T_2 weighted SE pulse sequences and T_2* weighted gradient echo (GRE) pulse sequences that give quantitative and qualitative information about the location of SPIONs *in vivo*, respectively.[32] Recently, an effort to improve detection limits has led to the modification of traditional SPION pulse sequences,[32b] as well as the application of nontraditional SPION pulse sequences such as fluid attenuated inversion-recovery (FLAIR).[33]

The sensitivity of MRI in the detection of single SPION loaded cells increases linearly with increasing resolution and increases hyperbolically with increasing signal-to-noise ratios

(SNR).[32b] Based on this observation, imaging with both high resolution and high SNR would give the greatest SPION detection capabilities; however, increasing resolution and SNR, both of which increase image acquisition time, would result in unreasonably long acquisition times. Since there are diminishing returns in increasing SNR, reduction in voxel size should be of primary concern to maintain acceptable imaging times. With this in mind, Hyen et al used a fast imaging employing steady-state acquisition (FIESTA) sequence based on a GRE pulse sequence that was able to detect femtomole quantities of SPIONs in labeled single cells *in vitro*.[32b] With this pulse sequence images are weighted by a ratio of T_2 and T_1, and detection limits are comparable to those of positron emission tomography (PET).[34]

The fluid-attenuated inversion recovery (FLAIR) sequence was developed to nullify signals from fluid and have shown to be useful in the diagnosis of central nervous system diseases.[35] This sequence first inverts the magnetic moments of protons in the z-axis before an additional 90° RF pulse at time TI (time between 180° and 90° RF pulse) tilts the magnetic moments into the xy-axis. This process can attenuate both tissue and/or fluid based on the chosen TI, but suffers from long imaging times. Fukukura et al recently demonstrated the effectiveness of a more rapid FLAIR echo-planar imaging (FLAIR EPI) sequence[33] for the detection of malignant liver lesions with SPION contrast enhancement.[35] By suppressing signal from cysts, vascular structures and periportal tissue, the FLAIR EPI sequence was more sensitive for detecting malignant liver tumors than either the T_2 weighted SE pulse sequences or the T_2* weighted GRE pulse sequences in human patients.

Limitations of T_2 contrast in low signal tissues have led to the development of specific pulse sequences that produce positive contrast in the presence of SPIONs. These methods attenuate background signal so that only fluid and tissue immediately adjacent to SPIONs are

visible in MR images. The current positive contrast sequences are classified as selective RF pulse methods,[36] dephased methods,[37] and off-resonance methods.[38] Selective RF pulse methods, such as inversion-recovery with on-resonant water suppression (IRON), employ inversion of magnetization in conjunction with a spectrally-selective on-resonant saturation prepulse that only generates signal from off-resonant protons in close proximity to SPIONs. Dephased methods employ a slice gradient in the region near the SPION that dephase background signal protons, but conserve signal from protons surrounding the SPION due to their induced magnetic field. Off-resonance methods utilize spectrally selective RF pulses that excite and refocus the off-resonance water surrounding SPIONs, while suppressing on-resonance signal from surrounding tissue. In addition to positive contrast sequences, post-processing methods that do not require special sequences for acquisition of positive contrast images have been developed.[39] Liu et al compared a post-processing susceptibility-gradient mapping (SGM) technique to IRON and the White Marker (dephased method) positive contrast sequences.[40] SGM more clearly delineates glioma tumors labeled with SPIONs than either the IRON or White Marker sequences in rats. Nevertheless, further studies are needed to compare the detection limit of the various positive contrast methods with those of the traditional spin echo methods.

2.2 Important SPION design parameters

The magnetic properties of the SPION are affected by the crystallinity and size of the magnetite core. In addition, surface modifications including polymer coatings and tissue targeting agents can have a profound effect on the efficiency of SPIONs as MRI contrast agents by increasing local concentrations of SPIONs in the tissue of interest while decreasing the concentration in background tissue. The efficiency of these contrast agents to increase the rate of relaxation of surrounding protons can be expressed by relaxivity (r_1, r_2), which is defined as the

slope of the plot $1/T_1$ or $1/T_2$ as a function of SPION concentration. By carefully considering parameters of core synthesis and post synthesis modifications, materials with superior relaxivity properties and *in vivo* kinetics can be produced.

2.2.1 Core considerations

Synthesis methods of SPIONs have a dramatic effect on their crystallinity. The two most common methods are co-precipitation[41] and thermal decomposition.[42] Synthesis of SPIONs by co-precipitation of Fe^{2+} and Fe^{3+} in aqueous solutions has traditionally been the most utilized synthesis method.[43] This method typically results in a lack of well-defined nanocrystalline size, stoichiometry, and magnetism.[26, 44] Furthermore, the production often yields both maghemite (Fe_2O_3) and magnetite. Magnetite is preferred of the two materials because of its superior magnetic properties.[45] Synthesis parameters of the co-precipitation method must be rigorously controlled so that nanocrystalline magnetite is the major product to maintain acceptable MR signal-enhancing effect. Thermal decomposition of iron organometallic compounds is a more recent approach that produces monocrystalline particles of stoichiometric magnetite.[46] The high temperatures of the thermal decomposition method allows for a higher rate of diffusion during the growth phase of the SPIONs resulting in improved magnetic properties that demonstrate high relaxivity.

The core size of SPIONs has significant effects on relaxivity properties. The thermal decomposition synthesis method produces SPIONs with highly controllable, monodisperse size distributions. Through minor modifications to synthesis parameters, SPIONs with mean diameters ranging from 4 nm to 20 nm can be produced with a narrow size distribution.[47] There is a correlation between particle size and T_2 relaxation due to changes in magnetic properties. As particle size is reduced there is a corresponding reduction in saturation magnetization which in

turn reduces the T_2 relaxation capabilities of SPIONs. This phenomenon is a result of increased surface-to-volume ratios due to decreased particle diameter. As particle size is reduced, the percentage of atoms found on the particle surface increases and the curvature of the particle surface considerably increases, resulting in significant surface effects. The atoms on the surface have a reduction in nearest neighbors resulting in unsatisfied bonds, as well as noncollinear spins, spin canting and spin-glass-like behavior. These effects can severely diminish the saturation magnetization of small SPIONs by reducing the number of atoms that contribute efficiently to the particle's magnetic moment.[48]

2.2.2 Surface modifications

2.2.2.1 Surface coating

Passivation of the iron oxide core is necessary for successful application of SPIONs *in vivo*. The high surface-to-volume ratio of nanoparticles yields high surface energies and are prone to surface oxidation which can have a significant effect on the magnetic properties of SPIONs.[45, 48-49] In addition to surface oxidation, high surface energies can lead to particle aggregation or clustering in physiological environments.[50] Modification approaches for surface passivation of SPION cores generally provide a reduction in surface energy as well as either steric and/or electrostatic repulsion. Upon intravenous injection, SPIONs are subjected to protein adsorption, or opsonization, in the first step toward clearance from the blood stream by the mononuclear phagocyte system (MPS). Evading MPS uptake increases the blood half-life of SPIONs which is crucial for many MRI applications, as increased blood-circulation time maximizes the odds of SPIONs reaching their target tissue. A common technique to avoid

opsonization and eventual clearance by the RES is to utilize hydrophilic coatings[51] such as polyethylene glycol (PEG)[52] and zwitterionic[53] polymers that resist protein fouling.

Many materials and coating approaches have been utilized for modifying the surface of SPIONs. Polymers are the most widely used coating materials and can be classified as hydrophilic or amphiphilic, neutral or charged, and homopolymers or copolymers.[54] These polymers can be anchored on the iron oxide surface by hydrogen bonds, electrostatic forces or through pseudo-covalent bonding.[18b] In general, the coating should provide the SPION with a hydrophilic exterior to increase water solubility and stability.

The choice of coating material can have a significant effect on the relaxivity of SPIONs. The coordination chemistry of the inner capping ligand(s) and the hydrophilicity of the coating layer are important factors on particle relaxivity.[49, 55] Daou et al have shown that coupling of surface coatings with the core of the SPION by carboxylates led to spin canting and decreased net magnetization, yet this effect was not observed when coupling was performed with phosphonates.[49] Additionally, the use of hydrophilic molecules such as polyethylenimine (PEI) as capping ligands allow for greater hydration around the magnetic core and yield higher proton relaxivity than SPIONs capped with hydrophobic ligands such as oleic acid.[55]

Polymer chain length, which corresponds to coating thickness, also has significant effects on relaxivity. Computer simulations have shown the effect of coating thickness on relaxivity is determined by two competing factors: the physical exclusion of protons from the SPION's magnetic field and the residence time for protons within the coating zone.[56] The structure of the coating layer determines which factor dominates. LeConte et al studied the effects of chain length on relaxivity for SPIONs with a bilayer coating.[56] In this system, the inner hydrophobic layer excludes water, while the outer hydrophilic PEG layer allows for water diffusion in the

coating zone. Increasing PEG chain length led to a reduction in r_2 values. Here it seems that the exclusion of water from the core by the inner hydrophobic layer more than offsets any effect by increasing the hydrophilic PEG layer thickness. Recent studies by Hu et al have shown that when water molecules are not excluded from regions close to the SPION core, r_2 relaxivity is increased with increased chain length.[57] SPIONs with diameters of 3, 4, 5 and 6 nm were coated with a single polymer layer of either short chain diethylene glycol or long chain PEG. Modification with PEG leads to an increase from 29 to 47, 42 to 69, 48 to 86, and 61 to 119 $mM^{-1}s^{-1}$ for the four SPION diameters respectively. These differences can be attributed to a larger water-slow diffusion layer of PEG modified SPIONs. Measurements of water diffusion coefficients in solutions of PEG of varying molecular weights indicate that water moves more slowly in more highly concentrated PEG environments.[58] Protons in the slow water diffusion layer spend a longer period of time in close proximity to the magnetic field of the SPION core allowing for more efficient dephasing of the magnetic moments of neighboring protons.

2.2.2.2 Targeting agents

Contrast agents that specifically target tissue can increases SNR by increasing local SPION concentration, potentially allowing for earlier detection of disease tissue such as small solid tumors and metastatic cells. Early SPIONs relied on passive targeting through the enhanced permeation and retention (EPR) effect which is the primary route for passive targeting in solid tumors. The EPR effect aids in nanoparticle uptake by way of leaky vasculature which allows particles with a hydrodynamic size generally less than 100 nm in diameter to cross from the vasculature into the interstitium.[59] Poor lymphatic drainage then aids in the entrapment of the particle in the solid tumor.

Alternatively, active targeting strategies provide mechanisms for specific accumulation of contrast agents within diseased tissue or cells. These strategies are based on the targeting of unique molecular signatures of afflicted cells, such as over-expressed growth factors and nutrient receptors.[60] Many types of ligands have been investigated in the targeting of these markers including antibodies, peptides, small molecules and aptamers.[61] A recent study by Sun et al illustrates the ability of targeting ligands to improve MR signal in diseased tissue.[62] In this study, PEG coated SPIONs were modified with CTX demonstrated tumor-specific SPION accumulation in tumors of a 9L xenograft mouse model. In a similar approach, Fang et al modified SPIONs with either cyclic arginine-glycine-aspartic acid (RGD) which targets tumor endothelial cells, or CTX.[63] SPIONs modified with RGD (NP-RGD) or CTX (NP-CTX) show significant increases in r_2 values in tumors post injection in a xenograft U87-MG tumor mouse model, while non-targeted control SPIONs do not.

Active targeting is not only important for improving tissue targeting specificity, but has also shown to improve the distribution of SPIONs within the targeted tissue. Improved distribution of SPIONs *in vivo* can be an important factor in maximizing relaxivity in tissue and cells. SPIONs tend to accumulate and even cluster in some specific tissue and/or cells, affecting their relaxation properties.[64] Transverse relaxivity first increases with increased cluster size followed by a marked decrease as cluster size continues to grow. Improved nanoparticle distribution in tissue due to active targeting has been demonstrated by several research groups.[65] In studies by Kievit et al, SPIONs were modified with both DNA for gene therapy and CTX (NP:DNA-CTX), with SPION/DNA as a non-targeted control (NP:DNA). The author's showed a reduction of SPION clustering in C6 tumors of a xenograft mouse model when SPIONs were functionalized with the CTX targeting agent. The improved SPION distribution can act to

minimize any reduction in relaxivity due to large cluster formation, leading to higher SNR and in turn, better delineation of tumor margins.

2.3 Multimodal imaging

SPIONs were developed specifically as an MR imaging contrast agent, yet advances in coating technologies have allowed for the addition of other functional imaging moieties including those for optical[29a, 66] (e.g. fluorophores) and nuclear imaging (e.g. radionuclides).[65b, 67] These multifunctional SPIONs can be designed to incorporate complementary imaging modalities that synergistically provide more accurate information *in vivo*. Each imaging modality has its advantages and limitations and no one modality can give a comprehensive snap shot of a biological system.

Fluorescent labeled SPIONs may serve as a platform for the next generation of multifunctional probes for multimodality imaging. They have been developed with the goal of providing optical contrast that will enable surgeons to intraoperatively distinguish cancer tissue from healthy tissue.[29a, 66a] These nanoparticles provide fluorescence by addition of numerous chromophores on the polymeric coating. SPIONs labeled with the near-infrared dye, Cy5.5, and CTX have shown the ability to produce both MRI and fluorescent tumor contrast in the brain of medulloblastoma transgenic mice.[29a] Kumar et al recently developed a SPION conjugated to Cy5.5 and myristoylated polyarginine peptides for translocation across the BBB.[63b] This probe showed remarkable uptake by U87 human glioma cells *in vitro* and excellent delineation of stereotactically injected tumors *in vivo* by MRI. These advances in SPION design would allow for both preoperative MR imaging and intraoperative optical monitoring with a single imaging

probe that could improve survival rates of brain tumor patients through better delineation of tumor boundaries.

PET/MRI multimodal imaging may offer significant advantages over either imaging modality alone. Several research groups have recently developed dual PET/MRI contrast probes that combine a SPION core with the radionuclide, Cu-64 chelated on the functionalized polymeric surface of the nanoparticle.[65b, 67] A combined PET/MRI contrast probe in an integrated system could obtain near perfect spatial registration of molecular/functional PET and anatomic/functional MRI.[68] This combination allows highly detailed anatomical MR images to be coregistered with PET images that currently have greater sensitivity to the location of contrast probes than clinical MRI.[67a] While SPIONs with multimodal imaging capabilities have been developed, their full potential has yet to be realized due to a lack of integrated multimodal imaging instrumentation.

SPIONs have been extensively studied as MRI contrast agents and several formulations have been approved for clinical use. However, their widespread utility has yet to be realized due to limitations of current detection limits and a lack of tissue specificity. Recent developments in both MRI acquisition methods and SPION synthesis and post-synthesis modifications have led to significant improvements in SPION detection sensitivity and *in vivo* biodistribution. Beyond modifications to current MRI acquisition methods that demonstrate greater SPION sensitivity in T_2 weighted negative enhancement images, new acquisition methods are being developed that can provide positive contrast and potentially address current limitations of SPION contrast enhancement. These imaging techniques take advantage of the magnetic properties of SPIONs that are continually improving due to a better understanding of core synthesis parameters that affect both core crystallinity and size, as well as postsynthesis modifications that can have a

dramatic effect on their magnetic properties and *in vivo* behavior. In addition, modifications of SPION surfaces with optical and nuclear imaging probes for multimodal imaging could improve diagnosis methods by combining the beneficial characteristics of each imaging modality.

Improvement of current detection limits is necessary for the successful translation of newly designed SPIONs to broad clinical application. Because of their magnetic properties and ease of functionalization, SPIONs have gained interest as theranostic agents capable of providing both diagnostic information and delivering therapeutics. In addition, the use of SPIONs for cell tracking in stem cell therapies has shown great promise. The potential of such applications in clinical settings is dependent on the development of highly sensitive imaging methods, as well as efficient contrast probes, and will only be realized with improvements to current detection limits.

Despite recent improvements to imaging methods that exploit the magnetic properties of SPIONs, there is still a need to improve detection of these probes *in vivo*. Additional research is needed to both optimize methods for synthesis of highly reproducible monocrystalline SPIONs and to gain a better understanding of the effects of polymeric coatings on magnetic properties. By addressing these issues researchers can usher in the next generation of SPIONs for MR imaging.

3 Magnetic nanoparticles as theranostic agents

The development of theranostic agents is a natural extension of the development of targeted molecular imaging agents for cancer diagnostics. The unique properties that allow nanoparticles to successfully function *in vivo* at the cellular and molecular level as diagnostic tools, simultaneously provides the basis for therapeutic applications. The polymeric components of diagnostic nanoparticles can be engineered to provide binding sites or reservoirs for drug deposition and delivery. The targeting agents that facilitate targeted molecular diagnostics, can aid in the proper *in vivo* trafficking of therapeutics to tumors. Furthermore, the imaging component serves as a means to track therapeutic delivery and tumor response in real-time to provide customizable treatment and can also serve as a therapeutic tool *via* radiosensitization, photodynamic, or photothermal therapy.[69] For non-intrinsic therapy, theranostic agents often incorporate existing chemotherapeutic drugs as many potent anti-cancer agents have limited use in the clinic due to poor pharmacokinetics and biodistribution profiles that lead to severe side effects and complications. Theranostic nanoparticles have shown to improve biodistribution profiles of these drugs through increased circulation time of delivered therapeutics, protection of therapeutic from degradation, and specific targeting of cancer cells.[70]

Theranostic agents can take many forms but are typically delineated as polymer or metal based agents. For a polymer based theranostic agents the key structural architecture is defined by polymer assemblies such as polymer nanospheres, micelles, dendrimers, or polymer based liposomes.[71] These theranostic agents rely on additional functionalization with radionuclides, metal NPs, or fluorophores to provide an imaging component. By contrast, metal based theranostic agents typically are designed with metal cores that serve as the imaging components and are further modified with polymer matrices that facilitates addition of targeting agents and

therapeputics while providing stabilization. Metal nanoparticles can exhibit unique physical (e.g., plasmonic resonance, magnetic, and fluorescent enhancement) and chemical properties (e.g., catalytic activity enhancement) that make them highly suitable for theranostic applications.[72] Gold NPs (AuNPs) for example have been extensively studied as theranostic agents due to their optical and x-ray imaging capabilities and potential as a photothermal therapy agent.[73] AuNPs properties are conferred by interaction of light with surface plasmons to produce the surface plasmon resonance phenomena that enhance all radiative and non-radiative properties of Au. The non-radiative process of converting absorbed light to heat provides the means for photothermal therapy (PTT). Silver NPs exhibit similar phenomena, but with the advantage that the plasmon resonance can be tuned to any visible/NIR wavelength.[72] However, a drawback of noble metal NPs is the use of ionizing radiation for CT or x-ray imaging and the limited tissue penetration of light for optical imaging. The limitation on visible/NIR light penetration through tissue also minimizes the usefulness of photothermal therapy for deep tissue tumors. While noble metal NPs have shown promise as theranostic agents, they are expensive to produce and are reported to have long retention times in clearance organs. For successful *in vivo* application, these issues will need to be resolved.

By contrast, the application of magnetic nanoparticles in diagnostic and intrinsic cancer therapy (e.g., hyperthermia treatment) utilize radio waves and magnetic fields that have no limitation in regards to tissue penetration. This advantage allows magnetic NPs such as SPIONs to be broadly applicable to many tumor types including those deep within the body. Additionally, SPIONs are relatively biodegradable and non-toxic with several formulations already approved for clinical imaging. The combination of biodegradability, low toxicity, non-invasive imaging capabilities, and the potential to serve as a magnetic hyperthermia (MH) cancer

treatment agent and a drug delivery system make SPIONs one of the most promising theranostic platforms currently under investigation. The remainder of this chapter will focus on the importance of and methods for *in vivo* SPION quantitation, MH treatment applications and the use of SPIONS as chemo/biotherapeutic delivery systems.

3.1 In vivo SPION quantitation

Development of accurate in vivo quantitation methods for SPION based theranostic agents is a critical step in the translation of these NPs to mainstream clinical use. For intrinsic SPION hyperthermia therapy and SPION delivery of bio/chemotherapeutics, the ability to accurately quantify therapeutic delivery at the point of interest will improve efficacy of treatment and patient's quality of life. While researchers have developed a range of suitable approaches for quantitation of SPIONs *in vitro* and *ex vivo*, continued work is needed to improve non-invasive *in vivo* techniques such as PET, SPECT, MRI and magnetic particle imaging (MPI) to realize the full potential of SPION based theranostic agents.

Researchers have developed a wide array of techniques for *in vitro* and *ex vivo* quantitation of SPIONs based on iron quantitation assays. Inductively coupled plasma-optical emission spectroscopy (ICP-OES) or inductively coupled plasma-mass spectrometry (ICP-MS), UV-Vis based techniques such as Prussian blue and ferrozine assays, as well as fluorescence measurements are a few commonly used approaches for quantitation of SPIONs.[74] ICP-OES, ICP-MS, Prussian blue and the ferrozine assay are all capable of directly measuring iron, but are limited to *ex vivo* application when quantitation is performed in tissue. The use of fluorescence imaging provides a means for *in vivo* quantitation of NIR fluorophore labeled SPIONs and is readily utilized by researchers in small animal models.[75] However, attenuation of light through

tissue restricts this approach to areas near the surface of the skin, limiting this techniques application in the clinic as a means for real-time monitoring of therapeutic delivery.

Clinically relevant non-invasive techniques such as PET and SPECT show high sensitivity to radiolabeled SPIONs but have several limitations including the use of ionizing radiation, poor spatial resolution, poor anatomical information, and the need to label SPIONs with radionuclides prior to imaging. A more promising approach is to exploit the intrinsic magnetic properties of SPIONS. The ability of SPIONs to shorten transverse relaxation in MRI and the linear relationship between the decay of MRI signal and the quantity of iron at low concentrations provides means for quantitation of SPIONs.[76] This ability has been utilized to quantify and track SPIONs in the brain, heart, central nervous system and tumors.[76b, 77] MRI provides excellent anatomical detail and good spatial resolution which allows for better determination of the SPION location within tissue than either PET or SPECT. However, MRI quantitation still has limitation that need to be addressed. The sensitivity of MRI to SPIONs is poor in comparison to the sensitivity of PET or SPECT imaging to radiolabeled SPIONS. The air-tissue interface can cause overestimation of the R_2 relaxation rates of SPIONs[77a, 77b] and compartmentalization and aggregation of SPIONs within tissue and cellular components can have significant effects on relaxation and therefore SPION quantitation.[78] Furthermore, interference from endogenous iron is another major contributor to overestimates of SPION concentration. Many of these challenges can be addressed by continued improvements both to SPION design and production as well as development of new MRI acquisition and post processing techniques.

AC magnetic susceptibility measurements (MSM) is a common technique employed to avoid endogenous iron interference in R_2 quantitation. This approach utilizes differences in the

temperature dependent out of phase susceptibility of SPIONs and endogenous iron when an AC magnetic field is applied. By measuring AC susceptibility at various temperatures, differentiation of SPION and endogenous iron can be achieved and has been used for successful *in vivo* SPION quantitation.[79] MSM analysis is rapid and has detection limits of 1-2 ppm, but its application is limited in clinical settings due to the lack of clinical instrumentation.

MSM allows for *in vivo* SPION quantitation but lacks the ability to produce a 3D image which is an important factor for real-time monitoring of treatment, where the ability to track changes in the size and morphology of the tumor is ideal. Magnetic particle imaging (MPI) is a new imaging technique that utilizes an oscillating magnetic field (drive field) to generate signal through non-linear magnetization of SPIONs.[80] A superimposed magnetic gradient field (selection field) allows for localization of the SPIONs signal and image formation. MPIs offers several advantages over other medical imaging modalities. The signal generated by MPI is only from the SPION with zero background interference.[81] Theoretical calculations produce sensitivity estimated for MPI to be ~20 nM with sub-mm resolution.[82] Despite these advantages, MPI will still require coregistration of anatomical images from other imaging modalities and require further advances in MPI tailored SPIONs to reach its full potential.[80]

3.2 SPION therapeutic approaches

3.2.1 SPIONs for magnetic hyperthermia treatment

The unique magnetic properties of SPIONs that make them excellent MRI contrast agents also allow for MH cancer therapy. Hyperthermia treatment increases temperature in a tissue microenvironment to 40-45 ºC resulting in a cascade of subcellular events leading to apoptosis. SPIONs have been extensively studied and have shown considerable promise as a magnetic

hyperthermia agent.[83] The therapeutic properties of SPIONs arise from Neel relaxation that leads to remnant magnetization and coercivity values of zero. The lack of remnant magnetization and coercivity allows SPIONs to become magnetized when an external magnetic field is applied, but show zero magnetism in the absence of an external magnetic field, permitting the magnetic dipole moments to flip freely at room temperature. Oscillation of an external magnetic field will cause magnetic dipole moments of SPIONs to reorient quickly causing energy loss in the form of heat which is then transferred to surrounding tissue. The extent of heating is determined by the frequency of the magnetic field oscillation and strength of the magnetic field applied.[84] Careful selection of appropriate oscillation frequency, field strength and SPION constructs are needed to maximize localized heating the in the presence of SPIONs while minimizing heating of healthy tissue.[85] This process in non-invasive and can be targeted to desired tissue by magnetic targeting or the use of targeting ligands.

A recent breakthrough in the MH field is the introduction of MagForce AG (Berlin, Germany) that has attained clinical use in Europe.[86] MagForce in principle can treat tumors of about 5 cm with an injection of 3 mL of a simple core-shell aminosilane coated SPION ferrofluid. In Phase II clinical trials, MagForce was tested for MH in combination with stereotactic radiotherapy. European approval of MagForce was granted for brain tumor therapy after an increase in life expectancy of 6 to 13 months was reported in patients with glioblastoma multiforme (GBM) when compared to chemoradiotherapy alone.

While promising, the MH application of simple, non-targeted SPIONs is limited due to the importance of tissue specificity in MH based therapy. Fantechi et al. reported the synthesis of a Co-doped SPION core coated with a cage structure of PEGylated genetically modified ferritin and an α-melanocyte-stimulating hormone peptide that has shown good targeting of melanoma

cells.[87] These SPIONs were small with a core of 7 nm, yet the Co-doping facilitated high magnetic efficiency and *in vitro* studies demonstrated MH induced apoptosis in B16 melanoma cells.

SPIONs have also found use in non-magnetic hyperthermia therapy. Zhou et al. have recently developed a PEGylated SPION with an oxidized surface layer capable of targeting, MR imaging and NIR PTT.[88] These SPIONs showed high magnetization and transverse relaxation in addition to their PTT potential. Interestingly, these SPIONs demonstrated a photothermal conversion efficiency of ~20.3% which is comparable to gold nanorods (~24.4%). In addition, under NIR laser irradiation the SPIONs maintained considerably better photothermal stability than Au nanorods, which cross-link under these conditions.

3.2.2 SPIONs as drug delivery systems (DDS)

The use of SPIONs as drug delivery systems holds considerable potential in the fight against cancer. SPIONs engineered to navigate biological barriers such as the BBB and the blood-tumor barrier (BTB) and avoid rapid renal and MPS clearance, provide means to deliver potent anti-cancer drugs more effectively.[70] This approach has potential to drastically reduce side effects currently associated with clinical chemotherapy by maximizing the amount of drug the reaches the tumor and minimizing the delivery of drug to healthy cells. The formulation of anti-cancer drugs on SPIONs also provides the ability to control release of therapeutics either in a time- or stimuli-responsive manner. Simple diffusion of physically absorbed drug from the SPION and release of drug due to degradation of the SPION-drug construct are examples of time-responsive mechanism. More sophisticated approaches rely on encapsulation or SPION-drug linkages (covalent or ionic) that release or are cleavable in a stimulus induced manner that

can be dependent on pH, redox potential, temperature, or electrical and magnetic fields.[89] Theranostic application of SPIONs is not limited to small drug delivery but has also shown promise in a wide range of therapeutic approaches including delivery of biotherapeutic macromolecules such as antibodies, peptides, DNA and siRNA.

Early attempts to utilize SPIONs as drug delivery systems often depended on non-cleavable approaches that released drug due to particle degradation caused by hydrolysis and a host of cellular processes but with no specific trigger for release. Utilizing this approach, Kohler et al. immobilized the chemotherapeutic, methotrexate, on the surface of a PEG coated SPION (NP-PEG-MTX).[90] In this study, methotrexate, which is an analog of folic acid served as both a chemotherapeutic and a targeting agent against folate receptors. NP-PEG-MTX was shown to significantly increase cytotoxicity in 9L cells as compared to free MTX *in vitro*. The use of an MTX antidote confirmed that toxicity was due to the anticancer activity of MTX and not the NP-PEG component. A more recent approach for small hydrophobic drug delivery that relies on concentration gradient driven diffusion is the development of core shell SPIONs with a hydrophobic layer between the iron oxide core and the hydrophilic polymer surface layer. Hsiao et al. utilized this method to load paclitaxel (PTX) on an amphiphilic chitosan coated SPION (CTX-PTX-NP) through hydrophobic interactions.[91] Hydrophobic oleic acid coated SPIONs where modified with amphiphilic hexanoyl-chitosan-PEG polymer to infer water solubility while maintaining the hydrophobic region to facilitate PTX loading. The SPIONs were further modified with tumor targeting peptide, chlorotoxin, for GBM targeting. CTX-PTX-NP showed excellent drug loading efficiency (31.1%) and minimal release in saline solution. Importantly, CTX-PTX-NP demonstrated GBM specific targeting and great therapeutic efficacy in GBM cell line U-118 MG.

In an effort to provide improved control over temporal and spatial release of therapeutics from SPION based theranostic agents, many researchers have turned to either external or physiologically induced stimuli-responsive drug release mechanisms.[92] These approaches can further minimize off target accumulation of drug by minimizing release in the blood or extracellular matrix. Many theranostic agents designed for cancer therapy utilize the difference in environmental pH between tumor and healthy tissue to control release of drug. Zou et al. recently reported development of PEG coated SPIONs functionalized with tumor targeting antibody and amine containing drug encapsulated in the PEG layer.[93] pH dependent release of drug was observed and hypothesized to be due to protonation of the amines at low pH. Hydrazone linkages that are acid cleavable but stable at neutral pH, have been used for delivery of doxorubicin. Hydrazone bonds are formed by reaction of hydrazides with aldehydes or ketones. Pourjavadi et al. produced a doxorubicin (DOX) loaded SPION utilizing a poly(amidoamine) (PMAM) dendrimer directly on the iron oxide surface followed by addition of hydrazide functional PEG that formed the hydrazone linkage between DOX and polymer. This SPION construct displayed high drug loading and pH dependent release of DOX.[94] In a similar approach, Kievit et al. loaded DOX on SPIONs (NP-DOX) through a hydrazine bond formed between hydrazides on the terminus of the PEG surface layer.[95] NP-DOX were incubated with drug resistant rat glioma C6 cells that over express the ATP-binding cassette (ABC) which transports hydrophobic drugs out of cancer cells. NP-DOX released DOX in a pH dependent manner and overcame the multidrug resistance (MDR) inferred by over expression of ABC to produce significant cytotoxicity in treated cells. Formation of hydrazone bonds are one example of a pH dependent release mechanism, but researchers have also utilized acid cleavable polymers such as poly (β-amino ester) to produce SPIONs with pH dependent drug release.[96] In addition,

disulfide linkages are responsive to both pH and redox potential of a microenvironment making them an attractive candidate for controlled release of therapeutics.[97]

Incorporation of SPIONs in to liposome structures allow for the use of an external magnetic field to assist controlled release. In this approach, SPIONs encapsulated in a drug loaded thermally sensitive liposome are subjected to high-frequency alternating magnetic field (AMF). The disruption of the lipid bilayer due to heating and mechanical perturbation caused by the AMF effects on SPIONs allows for temporally and spatially controlled rapid drug release.[98] Amstad et al. have prepared SPION loaded PEGylated liposomes with a membrane melting temperature far higher than body temperature.[99] These SPION-liposome constructs demonstrated colloidal stability and impermeability at body temperature but demonstrated repeated ability to release cargo in a controlled manner when pulsed with an AMF.

The ability of SPIONs to facilitate delivery of macromolecules such as DNA and siRNA provides a means to improve current gene therapy approaches for treating cancer.[100] Gene therapy has vast potential as a powerful tool capable of treating the root cause of cancer: DNA damage that leads to uncontrolled cell growth and eventually tumor formation. Viral vectors have high transfection capabilities but clinical trials have been limited due to narrow distribution of transfected cell near the injection site and concerns over safety and potential side effects. Synthetic vectors such as SPIONs have shown promise in vitro and in small animal models continue to make strides in vivo.

One advantage of SPION transfection agents over viral vectors is the ease at which targeting ligands can be incorporated to improve tumor targeting and distribution within the tumor. Kievit el al. developed a SPION transfection agent coated with a chitosan-PEG copolymer that was further modified with the cationic polymer polyethylenimine (PEI) and

targeting agent chlorotoxin (CTX).[101] PEI facilitated ionic interaction and binding with the negatively charge backbone of green fluorescent protein (GFP) encoding DNA. GFP was used as a reporter gene to easily test transfection efficiency by fluorescence imaging. It was found that the addition of CTX did not increase the amount of SPION present at the tumor site over non CTX labeled SPIONs, but did improve tumor distribution and cellular uptake, increasing transfection efficiency. This work highlights the importance of targeted delivery in the development of new transfection agents. More recent work by Wang et al. utilized the human tumor necrosis factor α-related apoptosis-inducing ligand (TRAIL) gene (*TRAIL*) incorporated on a cationic and CTX functionalized SPION for GBM gene therapy.[102] TRAIL is a protein that induces apoptosis in cancer cells, but its clinical use has been hindered by a lack of efficient methods for *in vivo* delivery. The successful delivery of the *TRAIL* would provide a means to produce the protein within the tumor, circumventing this limitation. SPION mediated delivery of *TRAIL* to T98G cells successfully produced TRAIL protein *in vitro*. Furthermore, the *TRAIL* modified SPION produced TRAIL protein when delivered to mice bearing T98G flank xenografts halting tumor growth and induced apoptosis in tumor tissue.

4 Redox-Responsive Responsive SPIONs for Drug Delivery to Brain Tumors

Resistance to temozolomide (TMZ) based chemotherapy in glioblastoma multiforme (GBM) has been attributed to the upregulation of the DNA repair protein O^6-methylguanine-DNA methyltransferase (MGMT). Inhibition of MGMT using O^6-benzylguanine (BG) has shown promise in these patients, but its clinical use is hindered by poor pharmacokinetics that leads to unacceptable toxicity. To improve BG biodistribution and efficacy, we developed SPIONs for targeted convection-enhanced delivery (CED) of BG to GBM. The nanoparticles (NPCP-BG-CTX) consist of a magnetic core coated with a redox-responsive, cross-linked, biocompatible chitosan-PEG copolymer surface coating (NPCP). NPCP was modified through covalent attachment of BG and tumor targeting peptide chlorotoxin (CTX). Controlled, localized BG release was achieved under reductive intracellular conditions and NPCP-BG-CTX demonstrated proper trafficking of BG in human GBM cells *in vitro.* NPCP-BG-CTX treated cells showed a significant reduction in MGMT activity and the potentiation of TMZ toxicity. *In vivo,* CED of NPCP-BG-CTX produced an excellent volume of distribution (Vd) within the brain of mice bearing orthotopic human primary GBM xenografts. Significantly, concurrent treatment with NPCP-BG-CTX and TMZ showed a 3-fold increase in median overall survival in comparison to NPCP-CTX/TMZ treated and untreated animals. Furthermore, NPCP-BG-CTX mitigated the myelosuppression observed with free BG in wild type mice when administered concurrently with TMZ. The combination of favorable physicochemical properties, tumor cell specific BG delivery, controlled BG release, and improved *in vivo* efficacy demonstrates the great potential of these SPIONs as a treatment option that could lead to improved clinical outcomes.

4.1 Introduction

Multifunctional nanoparticles (NPs) that enable diagnostic imaging and therapeutic drug delivery are rapidly emerging as a powerful modality in cancer therapy.[103] The ability to monitor drug delivery non-invasively *in situ* will provide clinicians with an unprecedented tool that may facilitate personalized therapeutic regimens for each patient's tumor.[104] Additionally, NPs are attractive as drug delivery vehicles because they can deliver potent doses of therapeutic agents to cancer cells with significantly improved specificity and reduced toxicities.[105] These advantages are achieved through targeted delivery and release of chemotherapeutics specifically in tumor cells.[103b] Proper integration of these favorable attributes in a single nanoparticle formulation is expected to offer a solution for highly intractable cancers such as glioblastoma multiforme (GBM).

Glioblastoma multiformes (GBMs) are malignant brain tumors that are among the most lethal cancers, striking 14,000 individuals in the U.S. each year.[106] Therapy has long included surgery followed by conformal radiotherapy (RT). Clinical trials have documented that the inclusion of the DNA methylating agent TMZ in the post-operative therapy of newly diagnosed GBMs has produced the first significant improvement in survival in the last 30 years.[107] The clinical efficacy of TMZ reflects, in part, its ability to cross the blood-brain barrier (BBB). Clinical outcome, however, is not improved by TMZ in the majority of GBMs because of resistance mediated in large part by MGMT, a DNA repair protein that removes the cytotoxic O6-methylguanine lesions produced by TMZ.[108]

In vitro studies suggest that GBM resistance to TMZ can be overcome by ablating MGMT activity with DNA repair inhibitors such as BG.[109] BG serves as a pseudo-substrate for MGMT and irreversibly inactivates the DNA repair protein. However, clinical trials have shown

that the inclusion of BG in TMZ treatment regimens reduces the maximum tolerated dose (MTD) of TMZ by 50%.[110] The significant reduction in MTD is primarily caused by the poor pharmacokinetics of BG, which poorly permeates across the BBB, is limited by a short blood half-life, and rapidly accumulates in clearance organs and bone marrow producing significant myelosuppression in combination with TMZ.[110-111] Hence, prognosis remains dismal with only 2% of patients surviving 5 years. This necessitates the development of novel therapeutic agents and utilization of delivery methods that can circumvent resistance mediated by tumor biology (e.g., drug resistance due to DNA repair) and by normal physiological barriers (e.g., the BBB).

The inability of many systemically delivered therapeutic drugs to cross the BBB or to accumulate in the brain at therapeutic levels have led researchers to develop more direct delivery methods.[112] Diffusion controlled delivery methods such as general intraneoplastic injection or the placement of drug loaded wafers in the resection cavity during brain surgery present some advantages, but are limited by poor Vd due to the diffusion limited delivery.[113] In contrast, CED utilizes fluid convection by maintaining a pressure gradient during interstitial infusion to enhance simple diffusion, leading to better Vd.[114] However, not all drugs are effectively delivered by CED. Small hydrophobic molecules in particular are subject to high rates of elimination by transport into cerebrospinal fluid or blood[115] and do not distribute well.[116] These limitations require the development of therapeutic agents engineered to take full advantage of CED.

We hypothesized that a multifunctional SPION formulation carrying a targeting ligand specific to GBMs, loaded with a BG chemotherapeutic payload, and administered *via* CED represents a more effective and less toxic treatment strategy. Our aim was to reformulate BG in combination with a theranostic nanoparticle platform to improve its intracellular delivery to GBM cells while minimizing its localization to healthy tissue. Here we report the development

of an SPION formulation for BG delivery, that contains a superparamagnetic iron oxide core coated with a redox responsive biopolymer shell of PEG and chitosan conjugated to a tumor-targeting peptide CTX.[9],[29b] SPION stability, *in vitro* BG intracellular trafficking, reduction of MGMT activity, potentiation of TMZ cytotoxicity in GBM cells, *in vivo* biodistribution, and toxicity were evaluated and compared against free BG. Furthermore, the efficacy of CED administered NPCP-BG-CTX was evaluated in orthotopic human primary GBM6 xenograft tumors. Importantly, this new BG loaded SPION formulation could be integrated into the existing therapeutic protocol for GBM management and offers the potential to significantly improve the prognosis of GBM patients.

4.2 Experimental

4.2.1 Materials

All reagents were purchased from Sigma Aldrich (St. Louis, MO) unless otherwise specified. The heterobifunctional linker 2-iminothiolane (Traut's reagent) was purchased from Molecular Biosciences (Boulder, CO). NHS-PEG_{12}-maleimide was purchased from Thermo Fisher Scientific (Rockford, IL). Tissue culture reagents including Dulbecco's modified Eagle medium (DMEM) and antibiotic–antimycotic were purchased from Invitrogen (Carlsbad, CA). Fetal bovine serum (FBS) was purchased from Atlanta Biologicals (Lawrenceville, GA).

4.2.2 NPCP synthesis

Iron oxide nanoparticles coated with a copolymer of chitosan-grafted-PEG were synthesized *via* a co-precipitation method as previously reported.[54b] Briefly, chitosan

oligosaccharide (5,000 kDa) was PEGylated with aldehyde-activated methoxy PEG to produce chitosan-grafted-PEG (CP). Pure CP (150 mg) was mixed with iron chlorides (9 mg Fe^{2+}, 15 mg Fe^{3+}) in 2.18 mL of degassed DI water. A solution (14.5 M) of ammonium hydroxide was titrated in slowly at 40 ºC until a final pH of 10.5 was reached to ensure complete nucleation of SPIONs. At this point, the synthesized NPCP were purified using size exclusion chromatography in S-200 resin (GE Healthcare, Piscataway, NJ) into 100 mM sodium bicarbonate buffer, pH 8.0 containing 5 mM EDTA. NPCP was then thiolated using Traut's reagent (10 mg) in 100 µL of 100 mM sodium bicarbonate, pH 8.0, 5 mM EDTA. The reaction was maintained in the dark at room temperature for 1 h. The thiolated NPCP was purified using size exclusion chromatography in S-200 resin (GE Healthcare, Piscataway, NJ) into 100 mM sodium bicarbonate buffer, pH 8.5 without EDTA and subsequently aged overnight at 4 ºC to promote disulfide bond formation.

4.2.3 Characterization of NPCP crosslinking

Hydrodynamic sizes of NPCP and NPCPs cross-linked at 10:1, 5:1 or 2.5:1 weight ratio of 2-Iminothiolane to iron was analyzed at 100 µg/mL in PBS (pH 7.4) using a DTS Zetasizer Nano (Malvern Instruments, Worcestershire, UK).

Quantification of the number of amine groups immobilized on the surface of NPCP and cross-linked NPCP was performed by reaction of N-succinimidyl 3-(2-pyridyldithio)propionate (SPDP) (4.3 mg) to NPCP (2 mg) for 2 h at room temperature to produce pyridyldithiol-activated NPCP. Pyridyldithiol-activated NPCP was purified using size exclusion chromatography with S-200 resin into 100mM boric acid buffer, pH 7.4. Purified pyridyldithiol-activated NPCP was then mixed with tris-(carboxyethyl)phosphine hydrochloride (TCEP) at a final TCEP concentration of 50 mM. The NPCP/TCEP solution was reacted on a rocker for 30 minutes at

room temperature. Cleaved pyridine-2-thiol (P2T) was separated from the reaction mixture (0.5 mL) using a 30 kDa MW cut off Amicon Ultra centrifugal filter (Millipore, Billerica, MA) centrifuged at 12,000 rcf for 10 minutes. The UV-vis absorbance spectra of the P2T rich supernatant was measured at 343 nm and quantified using an extinction coefficient of 8080 cm^{-1}. The concentration of P2T is equivalent to the concentration of reactive amines. The number of amines/NPCP was determined by measuring Fe concentration of the reaction mixture and calculating the molar concentration of NPCP assuming the nanoparticle has a core diameter of 7.5 nm and the density of bulk magnetite.

4.2.4 Synthesis of brominated BG

BG (2.4 mg) was dissolved in 500 µL methanol (MeOH) and mixed with N-bromosuccinimide (2 mg) dissolved in 500 µL MeOH. The reaction was maintained in the dark at room temperature for 24 h yielding brominated BG (BG-Br). MeOH was removed under vacuum. Bromination of BG was confirmed by LC-MS as described below.

4.2.5 Characterization of brominated BG

To quantitate BG-Br yield from the reaction mixture a Hewlett Packard 1100 Liquid Chromatography (LC) system (Palo Alto, CA, USA), with autosampler, coupled to a Bruker Esquire ion trap mass spectrometer (Billerica, MA, USA) with electrospray ionization (ESI) source was utilized. The BG/N-bromosuccinimide reaction mixture was separated with an Agilent Zorbax narrow bore C18 column that was 100 mm × 2.1 mm i.d. with 3.5 µm particle size (Agilent, Santa Clara, CA, USA). A binary mobile phase system of solvent A (water with

5% acetonitrile and 1% acetic acid) and solvent B (acetonitrile with 1% acetic acid) provided the best separation at 30 ºC and a flow rate of 200 µL/min with the following gradient: B increased from 0% to 50% over 15 min followed by an increase to 100% B for 16.5 min. A sample volume of 1 µL was injected into the column.

Analytes were ionized for mass spectrometric detection by positive ion ESI with the following conditions: spray voltage, 3 kV; drying gas temperature, 350 ºC; drying gas flow rate, 10 L/min; nebulizer, 30 psi; capillary voltage, 4 kV. MS data were collected in full scan mode over the mass range 50–2200 m/z with a scan resolution of 13,000 m/z/sec. Ion optic voltages were as follows: skimmer 1, 30 V; skimmer 2, 6 V; octopole, 3 V; octopole RF, 100 V; octopole Δ, 2 V; lens 1, –5 V; lens 2, –60 V. Bruker Daltonics DataAnlysis software, version 3.0, was used for data acquisition and analysis.

4.2.6 NPCP-CTX and NPCP-BG-CTX synthesis

NPCP in 100 mM sodium bicarbonate buffer, pH 8.5 was mixed with BG-Br and dissolved in dimethyl formamide (DMF) at a 5:1 weight ratio of iron to BG-Br. DMF volume was limited to 10% of the total reaction volume. The reaction was maintained in the dark at room temperature for 24 h to produce NPCP-BG. 300 µL of the NPCP-BG reaction mixture was set aside for evaluation of BG loading. The remaining NPCP-BG was purified using size exclusion chromatography in S-200 resin (GE Healthcare, Piscataway, NJ) into 100 mM sodium bicarbonate buffer, pH 8.0 containing 5 mM EDTA for further conjugations of fluorophores and chlorotoxin (CTX).

NPCP-BG (3.5 mg) or NPCP (3.5mg) was reacted with 1 mg of Cy5.5 (GE healthcare) in 100 mM sodium bicarbonate buffer, pH 8.0 containing 5 mM EDTA for 1 h at room temperature

protected from light and with gentle rocking. Excess Cy5.5 was removed using size exclusion chromatography in S-200 resin (GE Healthcare, Piscataway, NJ). A 1 mg/mL solution of CTX was prepared in thiolation buffer and reacted with 2IT at a 1.2:1 molar ratio of 2IT:CTX for 1 h in the dark. Concurrently, NPCP-BG-Cy5.5 was reacted with $SM(PEG)_{12}$ at a ratio of 216 μg of $SM(PEG)_{12}$/mg Fe in the dark with gentle rocking for 30 min. The $SM(PEG)_{12}$ modified NPCP-BG-Cy5.5 was then reacted with CTX-2IT at 1 μg CTX per 4.5 μg Fe for one hour in the dark to produce NPCP-BG-Cy5.5-CTX. The resultant SPION was purified using size exclusion chromatography in S-200 resin equilibrated with PBS, and stored at 4 ºC. For CED, SPIONs were brought to 2 mg/mL and supplemented with 2.5% 400MW PEG (w/w) and 2.5% dextrose (w/w) before being flash frozen in liquid nitrogen and stored at –80 ºC.

4.2.7 Evaluation of BG loading

The NPCP-BG reaction mixture (300 μL) was placed in a 3000 MW cutoff Amicon Ultra centrifugal filter (Millipore, Billerica, MA) and centrifuged at 12,000 rcf for 10 min. The flow through containing unreacted BG was collected and free BG was quantified by absorbance measurements at 280 nm using a SpectraMax M2 microplate reader (Molecular Devices, Sunnyvale, CA) and standard curve of known BG concentrations. BG conjugated to SPIONs was calculated by subtracting the amount of free BG from the total amount of BG in the reaction. The mean and standard de*via*tion of BG per NPCP was calculated from 4 independent representative batches.

4.2.8 Evaluation of CTX labeling

To quantify the degree of CTX attachment to nanoparticles, NPCP-BG-CTX was prepared as described above except unbound CTX was not purified from the NPCP-BG-CTX reaction mixture. The unpurified reaction mixture was mixed with an equal volume of Laemmli Sample Buffer (Biorad, Hercules, CA) and 30 µL was then loaded in a precast 4-20% polyacrylamide gel (Biorad, Hercules, CA). Free CTX at 500, 250, 125 and 62.5 µg/mL were mixed with an equal volume Laemmli Sample Buffer and loaded (30 µL) in the precast gel as standards. The gel was run at 100 V for one hr. Free, unreacted CTX separated from the CTX conjugated to SPIONs along with the CTX standards were imaged on a Gel Doc XR (Biorad, Hercules, CA) and quantified using the Quantity One software package (Biorad, Hercules, CA). The amount of CTX conjugated to SPIONs was calculated by subtracting the amount of free CTX from the total amount of CTX in the reaction and assuming an SPION molecular weight of ~600,000 g/mol.

4.2.9 Nanoparticle size and zeta potential characterization

The hydrodynamic size and zeta potential of NPCP-BG-CTX were analyzed at 100 µg/mL in 20 mM HEPES buffer (pH 7.4) using a DTS Zetasizer Nano (Malvern Instruments, Worcestershire, UK). NPCP-BG-CTX stability in biological fluid was analyzed at 100 µg/mL in DMEM supplemented with 10% FBS and 1% antibiotic-antimycotic.

4.2.10 TEM analysis of SPION core diameter

TEM images were acquired with an FEI TECNAI F20 TEM (Hillsboro, OR) operating at 200 kV. SPION core diameters were analyzed with ImageJ software and the size distribution, mean diameter and standard de*via*tion was calculated from 200 SPION measurements.

4.2.11 Drug release

For this assay an Alexa Fluor 488 (AF488: Invitrogen, Carlsbad, CA) labeled version of BG was prepared. An amine modified version of BG (BG-NH2) was purchased from New England BioLabs Inc. (Ipswich, MA) and modified with AF488 according to the manufacture's instructions to produce AF488 modified BG (BG-AF488). BG-488 was conjugated to NPCP as described above to produce (NPCP-(BG-AF488)). NPCP-(BG-AF488) (1 mg of Fe/mL) was diluted into PBS at pH 7.4 and acetate buffer at pH 5.0 containing 100 mM glutathione and incubated at 37 ºC for 0, 1, 8, and 24 h. CP-(BG-AF488) was separated from NPCP-(BG-AF488) using Amicon centrifuge filters (30,000 MW cutoff, Millipore). Free CP-(BG-AF488) content in the filtrate was determined by fluorescence measurements. Percent CP-(BG-AF488) released from NPCP-(BG-AF488) was calculated using the fluorescence of total amount of drug released over 24 h.

4.2.12 Cell culture

SF767, a human GBM cell line obtained from the tissue bank of the Brain Tumor Research Center (University of California–San Francisco, San Francisco, CA), was maintained in DMEM supplemented with 10% FBS and 1% antibiotic-antimycotic at 37 ºC and 5% CO_2.

4.2.13 In vitro GBM targeting

SF767 cells were maintained at 37ºC in 95%/5% humidified air/CO2 in DMEM containing 10% FBS and 1% antibiotic-antimycotic. For targeting experiments, 50,000 cells were plated in 24-well plates the day before SPION or CTX-AF647 treatment. SPION and CTX-AF647 treatments were performed in fully supplemented culture medium at 50 µg/mL SPIONs and 4 µM CTX-AF647. After a 2-hr treatment, cells were washed thrice before preparation for detection of SPION or CTX-AF647 labeling. Cells were washed with PBS, and detached using TrypLE Express (Invitrogen, Carlsbad, CA), and suspended in PBS containing 2% FBS. At least 10,000 cells were then analyzed using a BD FACSCanto flow cytometer (Beckton Dickinson, Franklin Lakes, NJ) and data analyses were performed using the FlowJo software package (Tree Star, Ashland, OR).

4.2.14 MGMT activity assay

The MGMT activities of protein extracts of human GBM SF767 cells were measured in a standard biochemical assay that quantifies the transfer of radioactivity from a DNA substrate containing [methyl^{3}H]O^{6}-methylguanine (specific activity, 80 Ci/mmol) to protein, as detailed previously.[117] SF767 cells (2×10^{6}) were plated in 100 mm dishes and incubated with 10 µM free BG for 2 or 24 h with NPCP-BG-CTX equivalent to 10 µM BG in fully supplemented medium. After incubation, cells were washed with PBS, collected, and protein extracts were prepared. The protein extract supernatant was prepared by dissolution of washed SF767 pellets of known cell number with non-ionic detergents in the presence of 600 mM NaCl.[118] Aliquots of crude homogenate were saved for DNA determination by the diphenylamine method that measures deoxyribose following degradation of DNA with heat and acid.[119] Crude homogenate was cleared by centrifugation at 10,000 × g for 30 min. Activity, normalized to cell number

using a conversion factor of 6 pg DNA per cell, is fmol O^6-methylguanine transferred per 10^6 cells.

4.2.15 Clonogenic survival assay

Determination of proliferative survival of SF767 by clonogenic assay was performed as described previously.[118] Briefly, 6-well plates inoculated with 2 mL of supplemented medium containing 500 to 1000 cells were incubated overnight at 37 ºC in 95%/5% air/CO_2 to allow reattachment and resumption of proliferation. Cells were then incubated for 24 h with NPCP-BG-CTX equivalent to 20 µM free BG prior to exposure to TMZ. Incubation was continued for 24 h before changing cells to fresh, drug-free medium to allow formation of colonies ≥ 50 cells. Controls included cells treated with NPCP-CTX (Fe equivalent to NPCP-BG-CTX) or with 20 µM free BG; untreated controls received an equivalent volume of DMSO solvent. Survival (mean ± SD) is the ratio of colony-forming ability of treated cells to that of untreated cells. Cytotoxicity was quantitated by linear regression analysis of plots of log surviving fraction *vs* TMZ dose to obtain the dose required to reduce survival to 10%, LD_{10}. Survival was determined in two separate experiments in which every dose was assayed in duplicate (i.e., four determinations per TMZ dose).

4.2.16 Animal model

GBM6 cells were obtained from the Mayo Clinic and maintained as flank tumors in nude mice.[120] Luciferase expressing GBM6 (GBM6-luc) cells were generated through lentiviral transduction and then maintained as flank tumors. For intracranial implant of GBM6-luc tumors,

flank tumors were harvested, minced with a scalpel, then suspended into an equal volume of ice cold PBS (1 mL PBS per 1 g of tumor). Tumor cells were disaggregated by gentle pipetting then filtered through a 40 µm filter and kept on ice at 10^7 cells/mL. Mice (nude athymic) were anesthetized with isoflurane and affixed to the base of a stereotaxic frame with ear bars. The skull was exposed through a 1 cm midline incision, then a burr hole made 2 mm to the right of bregma and 1 mm posterior to the coronal suture using a dremel equipped with a 1 mm tip. Using a Hamilton syringe attached to the stereotaxic frame, 2 µL of cells (20,000 cells) were injected over 1 min at a depth of 3 mm. After injection, the syringe was kept in place for 1 min prior to withdraw and the incision closed with Vetbond skin glue. Animals were monitored for tumor growth through Xenogen IVIS luminescent imaging.

4.2.17 In vivo survival studies

Treatments were started once tumors were visible with IVIS imaging. Treatment conditions were as follows: NPCP-BG-CTX (5 µL, 15 µg BG/kg) (n = 8) and NPCP-CTX (5 µL, Fe concentration equivalent to NPCP-BG-CTX dosage) (n = 10) were administered *via* CED 24 h prior to TMZ treatment (66 mg TMZ/kg suspended in Ora-Plus *via* oral gavage). A group of 12 animals were left untreated. CED was performed with a stereotaxic frame in the same manner as described for the tumor implant. A new burr hole was produced at the same location as for the tumor implantation and the tip of the Hamilton syringe was placed at a depth of 3 mm prior to infusion of 5 µL of SPION at 1 µL/min. The treatment schedule is indicated in **Figure 3-12a**. All mice were euthanized when they became moribund. Survival was monitored and analyzed using a Kaplan-Meier plot. Statistical analysis was performed using the log rank test.

4.2.18 Magnetic resonance imaging

Ex vivo whole mouse brain samples were fixed in formaldehyde and placed in fomblin (Sigma) immediately prior to imaging. Fixed brain samples were obtained from mice with no SPION injection, immediately after CED of SPION, and at $t = 24$ h, and at $t = 48$ h after CED of SPION. Imaging was performed on Bruker 14 Tesla magnet (Ultrashield 600 WB Plus), using a 25 mm single-channel ^{1}H radiofrequency coil (PB Micro 2.5). Imaging sequences included (i) T2-weighted rapid acquisition with refocused echoes (RARE) sequence, performed separately in the transverse and sagittal planes (TR/TE = 4000/27 ms, in-plane resolution = 52 × 78 μm^2, matrix = 384 × 256), (ii) T2*-weighted 2-D fast low-angled shot (FLASH) sequence (TR/TE = 1000/6 ms, in-plane resolution = 98 × 98 μm^2, matrix = 256 × 256), (iii) quantitative T2 multi-spin multi echo (MSME) sequence (TR = 4000 ms, TE = 6.7 + 6n ms, n = 0–16). 2-D slices of 0.5 mm thickness were used in all sequences. Analysis was performed using the Bruker integrated software package (ParaVision 5.1) for T2 calculation, and OsiriX for image display. Quantitative T2 values were displayed as mean ± standard deviation.

4.2.19 Serum half-life

All animal studies were conducted in accordance with University of Washington's Institute of Animal Care and Use Committee (IACUC) approved protocols as well as with federal guidelines. C57BL6 wild type mice (Charles River Laboratories, Inc.) were injected through the tail vein with 200 μl of 1 mg/ml nanoparticle (n = 3). At 1, 8, and 24 h after injection, blood was collected by retro-orbital eye bleed or terminal heart puncture. Because of limitations on the amount of blood that can be drawn from each animal, no animal was used for

more than one time points. Blood samples were drawn from three independent mice for each time point and frozen at −80º C until analysis. Samples were thawed at room temperature for 30 minutes prior to analysis. Whole blood was spun using a bench top centrifuge for 5 minutes at 10,000 rpm to separate the plasma. 50 ml of plasma was then added to a 96 well clear bottom plate. The plate was scanned on the Odyssey NIR fluorescence imaging instrument (LI-COR, Lincoln, NE) using the 700 nm-channel (lexc = 685 nm with lem = 705 nm) to measure Cy5.5 fluorescence signals.

4.2.20 Biodistribution of nanoparticles

The biodistribution of nanoparticles was performed as previously described.[66b] Briefly, animals were injected via tail vein with 200 µl of 1 mg/ml of nanoparticles. Three additional non-injected animals were included as controls. 48 h after injection (n = 3) the animals were euthanized and tissues were dissected from 6 different organs: liver, spleen, kidney, lung, heart, and brain. Tissues were then embedded in OCT and kept frozen at −80°C until needed. The frozen tissues were sliced in 12 µm thick sections and mounted onto glass slides. The tissue sections were thawed at room temperature for 30 minutes and the fluorescence intensity was measured using the Odyssey fluorescence scanner at a resolution of 21 µm. The images were analyzed with the public-domain ImageJ software (US National Institutes of Health, Bethesda, MD). The average fluorescence intensity was determined for each tissue type using the same threshold settings (low threshold: 400, high threshold: 20,000). Data were reported as the average channel fluorescence of the tissue, given as relative units after background subtraction. For visual illustrations of fluorescence signals, color maps are generated using Matlab (Mathworks, Natick, MA).

4.2.21 Histopathological evaluation and hematology assay

Whole organs (brain, liver, kidney, and spleen) of C57BL/6 mice were removed through necropsy 120 h after intravenous injection of nanoparticles or PBS and preserved in 10% formalin for 48 h. Tissues were then embedded in paraffin wax, sliced into 5 µm thick sections, and stained with hematoxylin and eosin (H&E) or Prussian blue/Nuclear Fast Red using standard clinical laboratory protocols. Microscopic images of tissues were acquired using an E600 upright microscope (Nikon) equipped with a CCD color camera. Blood cell panels and serum aspartate aminotransferase (AST) and alanine aminotransferase (ALT) levels were quantified 120 h after intravenous administration of nanoparticles or free drug (n = 3 per treatment condition), and compared to mice receiving PBS injection (n = 5). Blood (300 µL) was drawn from each mouse through cardiac heart puncture. Samples were then submitted to a veterinary pathology laboratory (Phoenix Laboratories, Everett, WA) for third party analysis.

4.3 Results and discussion

4.3.1 Formulation and characterization of nanoparticles

Figure 3-1 shows the synthesis of chitosan-PEG (CP) copolymer coated nanoparticles (NPCP), cross-linked and functionalized with BG (NPCP-BG) and CTX (NPCP-BG-CTX). NPCP consists of a 7.5 nm iron oxide core coated with CP (**Figure 3-1a**).[54b] It should be noted that the carrier's core material, iron oxide, is biocompatible and biodegradable, and enables the monitoring of drug trafficking and delivery by magnetic resonance imaging (MRI) when administrated both *in vitro* and *in vivo*. Reactive sulfhydryl groups were then introduced to the CP shell by reaction of 2-iminothiolane to amine groups of chitosan (**Figure 3-1b**). The sulfhydryl groups then oxidized and formed disulfide bridges producing a redox sensitive cross-

linked polymer shell. BG was then activated with N-bromosuccinimide (BG-Br) rendering it amine reactive (**Figure 3-1c**). NPCP was then reacted with the brominated BG, followed by addition of CTX and Cy5.5 to produce NPCP-BG-CTX (Figure 1d). The BG loaded nanoparticles were readily soluble in PBS and cell culture media without the need of excipients.

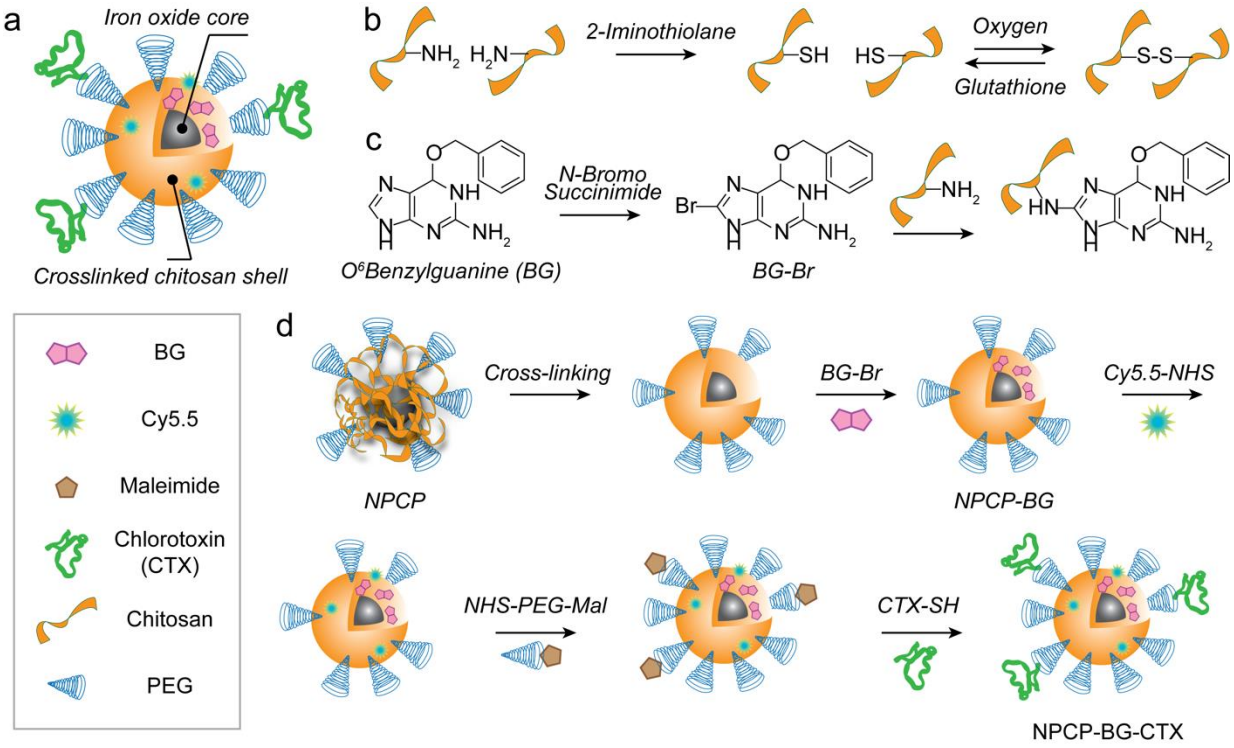

Figure 4-1. Synthesis of NPCP-BG-CTX. a) Illustration of fully functionalized NPCP-BG-CTX. b) Cross-linking of NPCP coating through intracellular reducible disulfide linkages. c) Activation of BG by bromination and subsequent reaction with amines on the chitosan backbone. d) Modification of NPCP with BG and CTX to produce NPCP-BG-CTX.

Cross-linking of the NPCP polymer coating via disulfide bond formation was utilized to further stabilize the NPCP for subsequent conjugation of BG, fluorescent probes and CTX, as well as provide a mechanism for release of drug within target cells. To optimize cross-linking, amine reactive Traut's reagent was reacted with NPCPs at 10:1, 5:1 and 2.5:1 weight ratios of

Traut's reagent to iron. The stability of the cross-linked NPCPs was compared to non-cross-linked NPCPs in PBS (**Figure 3-2a**) with respect to changes in hydrodynamic size over time. We found that cross-linking dramatically stabilized the nanoparticle at all three Traut's reagent ratios. Since the reaction with Traut's reagent consumes amines that are necessary for subsequent conjugations, we quantitated the number of reactive amines of NPCP and cross-linked NPCPs produced at the three cross-linking ratios (**Figure 3-2b**). These results show that at the 2.5:1 ratio, only a small fraction of available amines were consumed by Traut's reagent, indicating that few disulfide bonds could be formed at this ratio. Both the 5:1 and 10:1 ratios show a significant drop in the number of amines indicating a greater number of thiols for disulfide bond formation, yet maintain an adequate number of amines for further conjugation. Since there was not a significant gain in free thiols by increasing the Traut's reagent ratio from 5:1 to 10:1 and further experiments showed that the 2.5:1 ratio was not consistent in stabilizing NPCPs, the 5:1 ratio was determined to be optimal.

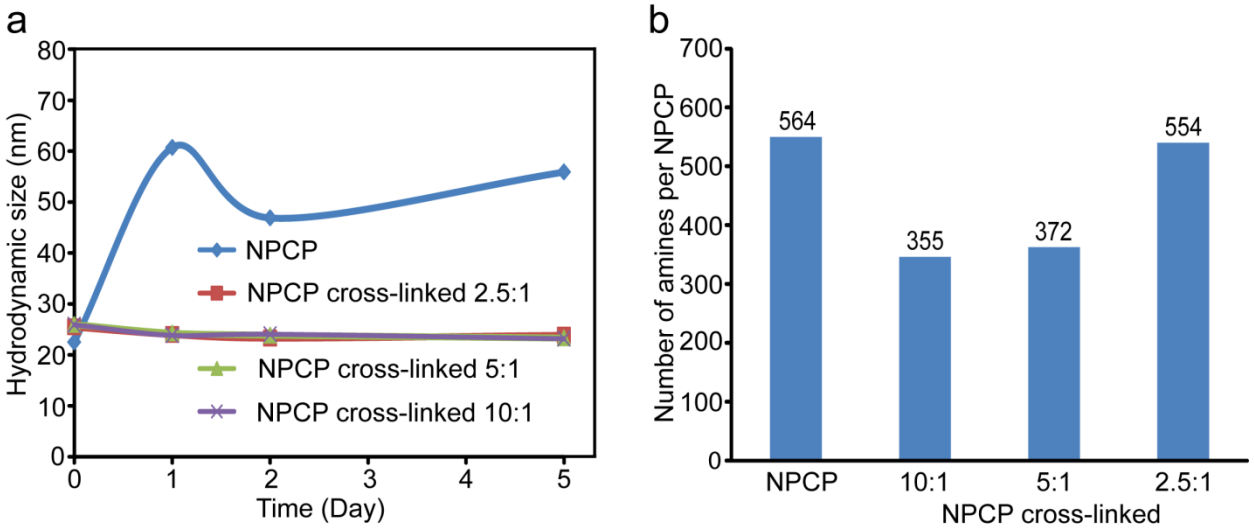

Figure 4-2. Cross-linking optimization of NPCP polymer coating. a) Stability over 5 days of NPCP and NPCP cross-linked at 10:1, 5:1 and 2.5:1 weight ratio of Traut's reagent to iron in PBS. b) Number of reactive amines on the polymer coating of NPCP and NPCP cross-linked at 10:1, 5:1 and 2.5:1 weight ratio of Traut's reagent to iron.

Unmodified BG contains no reactive handle for conjugation to SPIONs, therefore, bromination of BG at the C8 position was necessary for conjugation of BG to NPCP. Bromination of BG was confirmed by tandem liquid chromatography-mass spectrometry (LC-MS) (**Figure 3-3a).** Extracted ion chromatography (EIC) was used to analyze data for ions with specific mass to charge ratios (m/z) allowing for easy identification of analytes. The chromatographic peak at 13.1 min (242 m/z) in the blue trace corresponds to unmodified BG, whereas the peak at 16.2 min (321-323 m/z) in the yellow trace corresponds to BG-Br. Integration of these peaks showed ~60% yield of BG-Br from the reaction mixture.

The hydrodynamic size and zeta potential of nanoparticles can drastically influence their *in vivo* functionality, clearance, and overall safety.[103c] The intensity based hydrodynamic sizes of NPCP-BG-CTX in 20mM HEPES, pH 7.4 was measured by dynamic light scattering (DLS)

(**Figure 3-3b**). The Z-average size of NPCP-BG-CTX was 76 nm in HEPES and remained stable in biological fluid (DMEM with 10% FBS) for over 10 days (**Figure 3-3c**). Notably, the hydrodynamic size distribution for the SPION remained appropriate for *in vivo* navigation and evasion of rapid clearance by the reticuloendothelial system (5 nm < d < 200 nm)[59a] and for CED (<100 nm).[115] Additionally, the average zeta potential of NPCP-BG-CTX was measured to be near neutral at 4 ± 7.4 mV (**Figure 3-3d**). A near neutral zeta potential is ideal since a strong positive surface charge can lead to non-specific interactions with negatively charged cell membranes and reduced Vd,[121] whereas a strong negative surface charge can lead to non-specific interactions with the positively charged extracellular matrix.[122]

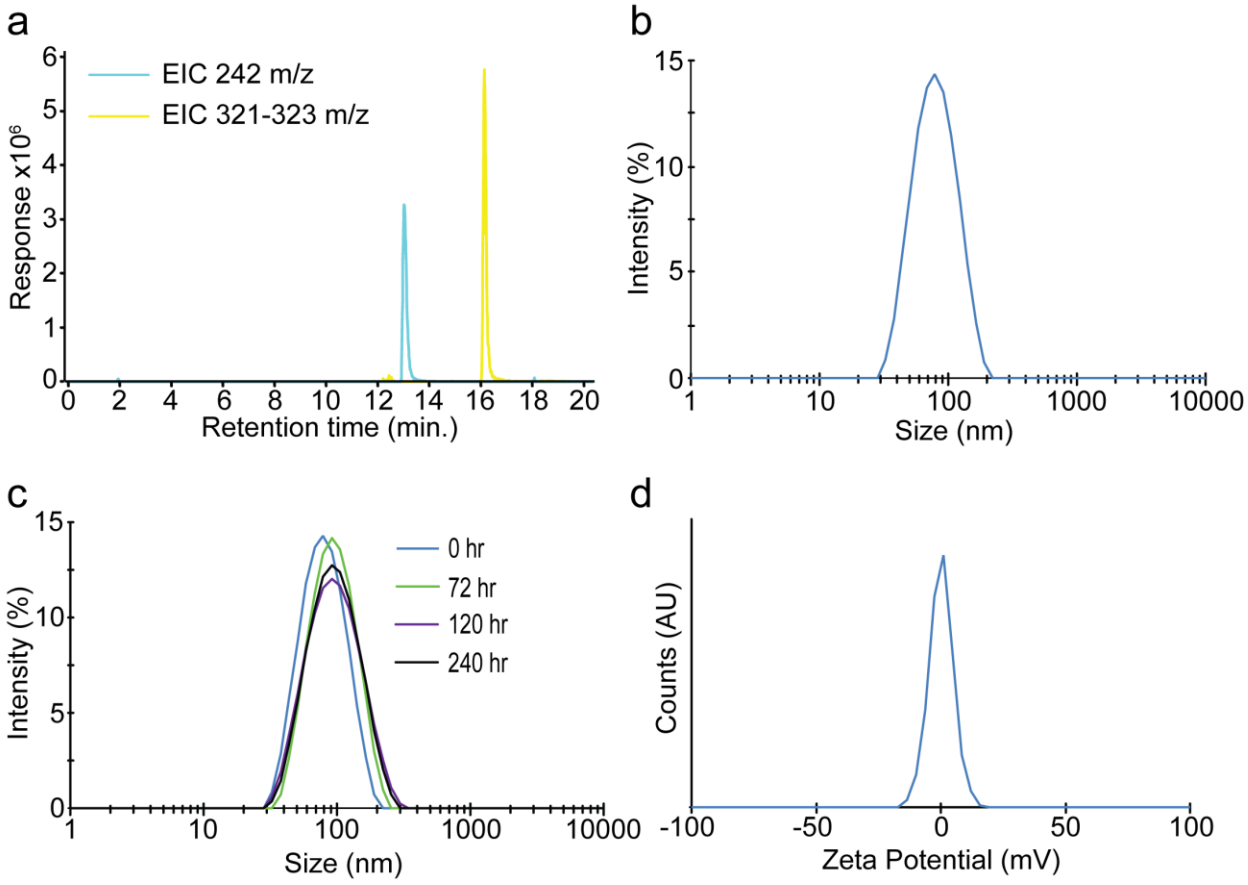

Figure 4-3. LC-MS analysis of BG-Br and physicochemical characterization of NPCP-BG-CTX. a) Extracted ion chromatogram of reaction mixture of BG and N-bromosuccinimide in methanol, analyzed by LC ESI TOF MS. The blue trace corresponds to unmodified BG (242 m/z) and the

yellow trace corresponds to BG-Br (321-323 m/z). b) Intensity based hydrodynamic size distribution of NPCP-BG-CTX in 20mM HEPES, pH 7.4 as determined by DLS. c) NPCP-BG-CTX stability in biological fluid (DMEM containing 10% FBS). d) Zeta potential distribution of NPCP-BG-CTX in 20mM HEPES, pH 7.4

To accurately determine the number of BG and CTX molecules per SPION, the SPION molecular weight was determined by measuring the mean core diameter of SPIONs from transmission electron microscopy (TEM) images (**Figure 3-4a-b**). The mean core diameter of NPCP-BG-CTX was 7.5 ± 1.3 nm which corresponds to an iron based molecular weight of ~600,000 g/mol. Using UV/Vis spectroscopy the number of BG molecules per SPION was estimated to be 150. Furthermore, using a gel electrophoresis assay the number of CTX peptide per SPION was found to be approximately three. **Table 4-1** summarizes the key physicochemical properties of NPCP-BG-CTX.

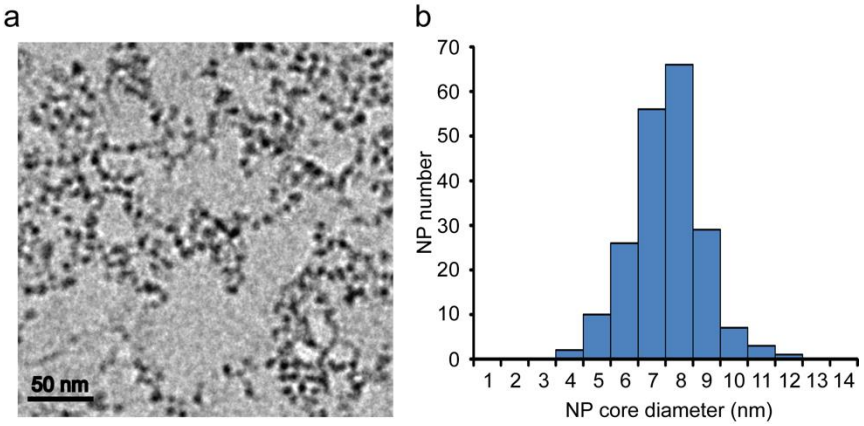

Figure 4-4. Determination of SPION core size. a) Representative TEM image of NPCP-BG-CTX. Scale bar corresponds to 50 nm. b) Distribution of SPION core diameters yielding a mean of 7.5 ± 1.3 nm determined from 200 independent core measurements using ImageJ software.

Table 4-1. Primary physicochemical properties of NPCP-BG-CTX.

Core Size (nm)	Hydrodynamic Size (nm)	Poly Dispersion Index	Zeta Potential (mV)	BG Molecules/ SPION	CTX Molecules/ SPION

7.5 ± 1.3	76 ± 3.8	0.16	4 ± 7.4	150 ± 14	3 ± 1

A challenge in developing drug carrier SPION formulations is ensuring rapid and effective intracellular release of drugs in target cells while minimizing release in the blood or extracellular matrix. Several strategies have been investigated to create SPION formulations that selectively respond to environmental stimuli such as temperature, pH, ionic strength, redox potential, and electrical or magnetic fields.[89, 123] Among them, redox responsive SPIONs are most attractive as cells regulate the reducing potential in their environment both intracellularly and extracellularly through the expression and secretion of reducing enzymes such as glutathione.[124] These enzymes are known to be present in the cytoplasm at 1000-fold higher levels than those found in the blood.

To determine the redox responsive properties of our SPIONs, NPCP-BG-CTX was incubated in solutions similar to blood conditions (BC environment: PBS pH 7.4) and intracellular conditions (IC environment: Acetate buffer pH 5 and 100 mM glutathione) to examine drug release under reducing conditions likely encountered following SPION tumor uptake and intracellular sequestration.[123b] Gel electrophoresis was used to monitor biodegradation of the polymer/BG/CTX conjugate (CP-BG-CTX) coating from the iron oxide core in response to BC and IC environments (**Figure 3-5a**). SPIONs and any bound polymer coating remained in the gel loading wells while unbound polymer freely moved down the gel lanes. Based on the intensity of the bands remaining in the loading wells, the IC environment resulted in more degradation of the CP-BG-CTX coating than the BC environment. CP-BG-CTX release was quantitatively monitored using a fluorescence assay where BG was fluorescently

labeled with Alexa Fluor 488 (BG-AF488) and biodegradation of CP-(BG-AF488)-CTX from the iron oxide core was determined in BC and IC environments by collecting the filtrate at 0, 1, 8 and 24 h using centrifugal filters (**Figure 3-5b**). CP-(BG-AF488)-CTX was released rapidly under conditions mimicking intracellular environments reaching maximum CP-(BG-AF488)-CTX release at 1 h. However, under conditions mimicking blood, maximum CP-(BG-AF488)-CTX release was not achieved until 24 h. The significantly elevated CP-(BG-AF488)-CTX release under IC conditions demonstrates that controlled intracellular BG drug release can be achieved using this SPION formulation.

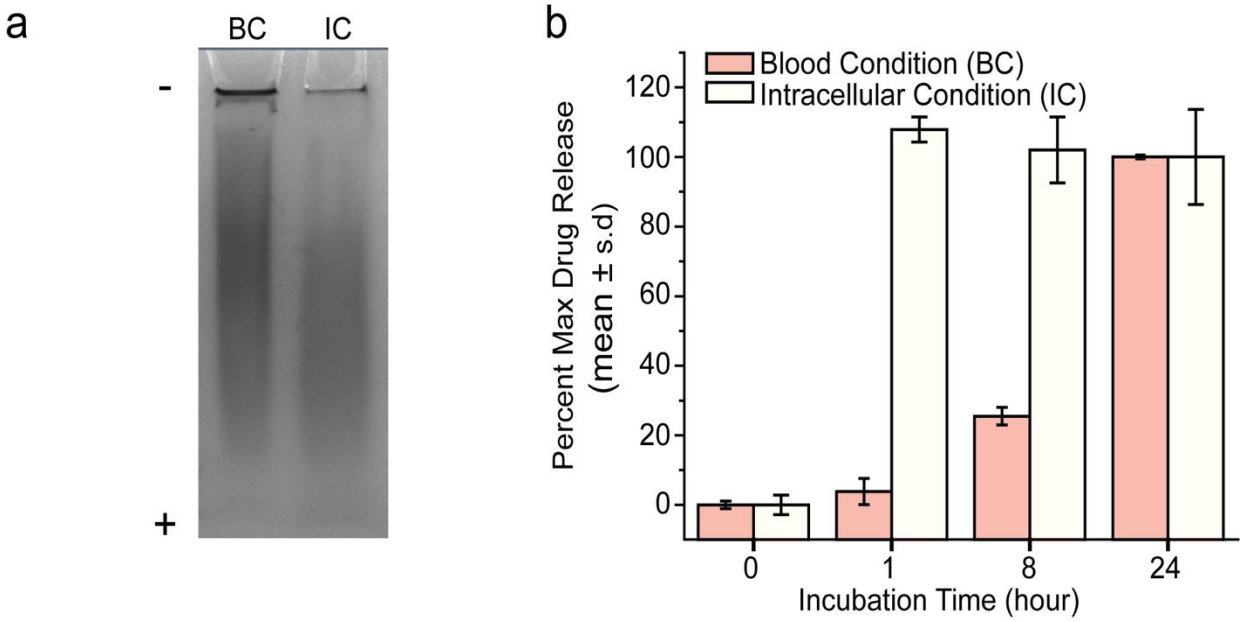

Figure 4-5. NPCP-BG-CTX drug release. a) Coomassie blue stained polyacrylamide gel electrophoresis image of NPCP-BG-CTX incubated for 1 hour under blood conditions (BC) and intracellular conditions (IC) showing pH and glutathione sensitive degradation of the CP-BG-CTX coating from SPION. b) Drug release profiles showing the pH and glutathione sensitive release of CP-(BG-AF488)-CTX from NPCP-(BG-AF488)-CTX. BC = pH 7.4 and no glutathione, and IC = pH 5.0 and 100 mM glutathione.

4.3.2 Internalization of NPCP-BG-CTX by human GBM cells in vitro

To efficiently deliver BG *in vivo*, SPIONs must be equipped with ligands that bind to tumor cells with high specificity and avidity. CTX, a small peptide of scorpion venom that has been shown to bind to MMP2[125] and Annexin A2[126] on cell surfaces, has high specificity and avidity for GBM but not normal brain tissue.[127] We have previously shown that CTX-conjugated SPIONs are efficiently taken up through endocytosis in rodent glioma cells.[103c, 128] Unlike other ligands, which target only certain types of brain tumors, CTX targets the majority of brain tumors examined (74 out of 79).[127b, 129]

CTX targeting of the human GBM cell line SF767 was confirmed by flow cytometry. **Figure 3-6** shows uptake of targeted (NPCP-BG-CTX) and control SPION (NPCP-BG) by target cells (SF767) and evaluated against a control cell line, HFF, which are not upregulated in MMP-2 or Annexin A2 expression. Here, SF767 cells treated with the CTX-enabled SPION showed significantly increased internalization levels when compared with cells exposed to the non-functionalized SPION. Conversely, the HFF cells showed little interaction with both SPION types, indicating selective binding of the SPION presenting the CTX peptide. All cell lines were incubated with SPION formulations at a 50 μg of Fe/ml dose. At this dose there was nearly a 2-fold increase in uptake of CTX-modified SPION by SF767 cells compared with control SPION. Furthermore, there was a four-fold improvement in uptake of the targeted NPCP-BG-CTX SPIONs by SF767 cells compared to HFF cells.

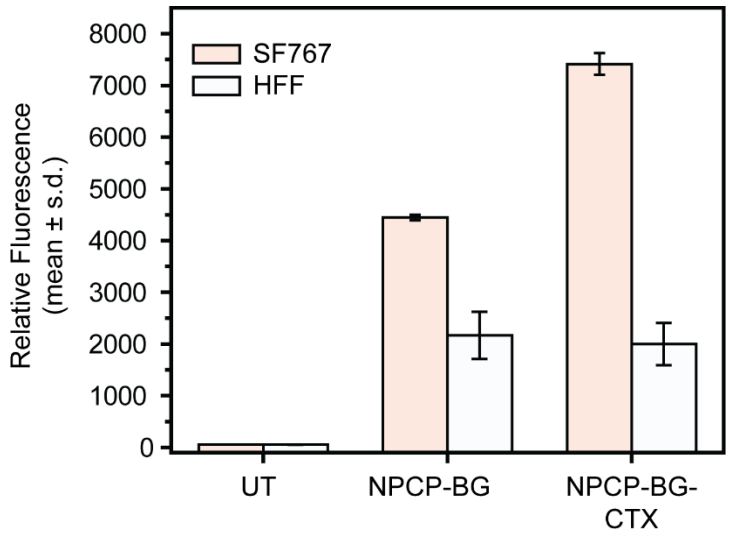

Figure 4-6. Flow cytometry analysis of NPCP internalization by SF767 (GBM cell line), and control HFF cells 2 h post treatment with either NPCP-BG or NPCP-BG-CTX; also shown is the result for cells receiving no nanoparticle treatment (UT) as a reference.

Visual confirmation of SPION internalization and BG delivery was established by confocal microscopy. Images were obtained from SF767 cells treated with NPCP-AF647-CTX (SPIONs labeled with fluorophore), BG-AF647 (fluorophore labeled BG), and NPCP-(BG-AF647)-CTX (SPIONs carrying fluorophore labeled BG). In all images (**Figure 3-7**), cells were fixed after SPION/BG treatments, nuclei were stained with DAPI (blue) and membranes with WGA-555 (green). Treatments with these formulations were administered at a concentration of 50 µM of BG or its SPION equivalence. In the top panel, NPCP-AF647-CTX (red, third column) can be visualized in the treated cells. The overlay images (fourth column) reveal that the NPCP-AF647-CTX formulation is bound to the SF767 cells. The middle panel shows CP-(BG-AF647)-CTX localized in the nucleus with NPCP-(BG-AF647)-CTX delivery. Similarly, the lower panels show free BG-AF647 localized in the nucleus. This observation suggests the proper release and trafficking of BG within cells.

Figure 4-7

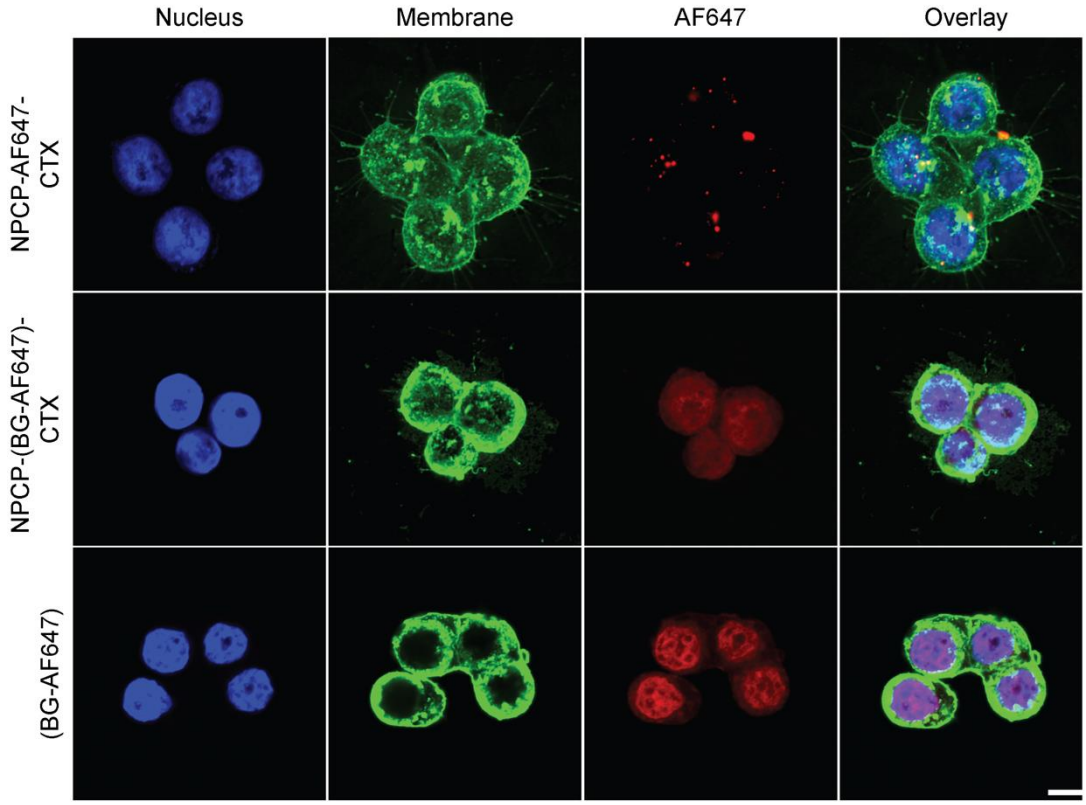

Figure 4-8. Confocal fluorescence images of SF767 cells treated with one of three treatment formulations: NPCP-AF647-CTX (fluorophore labeled NPs), NPCP-(BG-AF647)-CTX (NPs loaded with fluorophore labeled BG), and BG-AF647 (fluorophore labeled BG). Cells were imaged 24 h post treatment. Cell nuclei are shown in blue, cell membranes in green, and NPCP-AF647-CTX or BG-AF647 in red. The scale bar corresponds to 10 μm.

4.3.3 NPCP-BG-CTX inhibition of MGMT and potentiation of TMZ cytotoxicity in human GBM cells

MGMT is the sole repair activity that removes O6-methylguanine (O6-meG) adducts from DNA in human cells and plays an important role in GBM resistance to TMZ.[130] Suppressing DNA repair activity is a promising strategy for improving TMZ-based therapies.[131] **Figure 3-8a** shows the effect of free BG and NPCP-BG-CTX treatments on MGMT activity in SF767 cells. In this experiment, MGMT activity was assayed in untreated cells, cells incubated

with 10 μM free BG and NPCP-BG-CTX equivalent to 10 μM BG for 2 or 24 h. Untreated cells had an activity of 39 fmol/106 cells or roughly 23,500 MGMT molecules/cell. All treatment conditions were normalized as a percent MGMT activity of untreated SF767 cells. Exposure to free BG for 2 h reduced the activity by ~4.8-fold (~21% of untreated activity) and exposure for 24 h reduced activity by ~10.3-fold (~9.7% of untreated activity). Importantly, incubation with NPCP-BG-CTX for 2 h also reduced MGMT activity ~1.5-fold (~67% of untreated activity), and achieved a greater than 5.4-fold (~18.7% of untreated activity) reduction in activity 24 h after the initial exposure to NPCP-BG-CTX. Control SPIONs with no BG conjugated (NPCP-CTX) showed no reduction in MGMT activity at 2 and 24 h. These results demonstrate that SPION-conjugated BG produces similar reduction of MGMT activity in a human GBM cell line as free BG after 24 h exposure.

SF767 cells are noted for their pronounced resistance to TMZ (LD10 at roughly 640 μM) mediated in large part by MGMT.[118] The effect of suppression of MGMT activity by NPCP-BG-CTX on TMZ-mediated reduction in clonogenic survival of SF767 is illustrated in **Figure 3-8b**. Cells were exposed to NPCP-BG-CTX equivalent to 20 μM free drug for 24 h followed by incubation with TMZ for 24 h in the presence of inhibitor. Controls were treated either with 20 μM free BG, NPCP-CTX or with an equivalent volume of DMSO. A linear regression analysis was performed on the linear portions of the survival curves to determine LD10. NPCP-BG-CTX reduced the resistance by about 40-fold (LD10 15.7 ± 1.1 μM), a potentiation of cytotoxicity comparable to that produced by free BG (LD10 12.8 ± 1.6 μM). These results demonstrate that NPCP-BG mediated suppression of MGMT is accompanied by greater sensitivity to TMZ in human GBM cells.

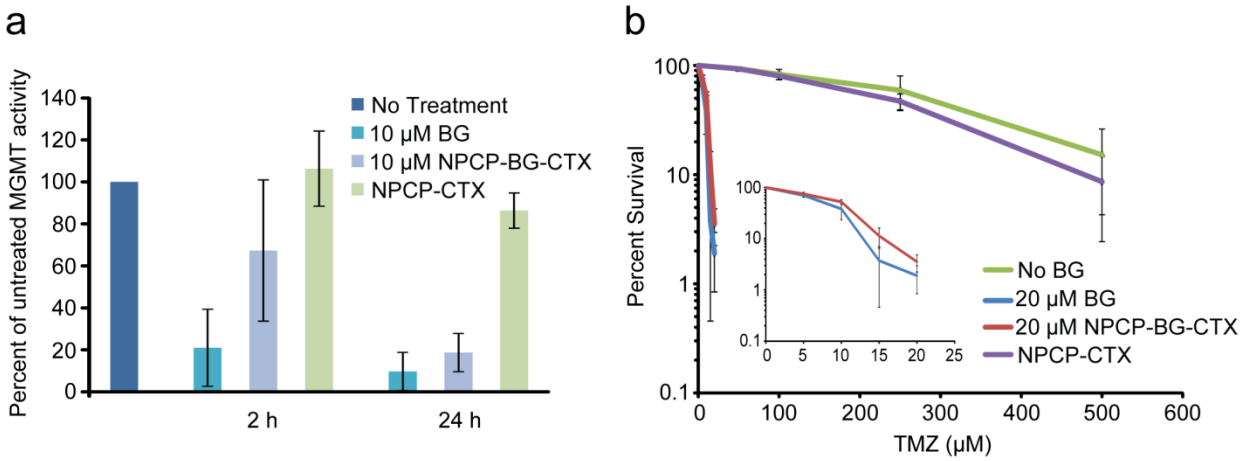

Figure 4-9. NPCP-BG-CTX inhibits MGMT and sensitizes GBM cells to TMZ. a) Suppression of MGMT activity in SF767 cells treated with BG, NPCP-BG-CTX or NPCP-CTX. Cells were harvested 2 h and 24 h after inhibitor exposure and MGMT activity determined in cleared supernatants of whole cell homogenates by quantitating transfer of radioactivity from DNA containing O6-[3H]methylguanine to protein.[117] Data represent the results of cells treated with a single preparation of NPCP-BG-CTX and are representative of results observed using independent preparations of NPCP-BG-CTX. b) Suppression of MGMT activity with NPCP-BG increases TMZ cell killing of the GBM line SF767. Survival of SF767 cells treated with TMZ alone (no BG), or exposed to 20 μM BG or NPCP-BG-CTX containing 20 μM BG for 24 h prior to 24 h exposure to TMZ was determined by a clonogenic colony-forming assay. The inset displayed at a finer scale reveals the comparable effect of BG and NPCP-BG-CTX on cell killing.

4.3.4 CED and in vivo efficacy of NPCP-BG-CTX

To evaluate CED and combination therapy of NPCP-BG-CTX with TMZ *in vivo*, we used a clinically relevant primary GBM xenograft using GBM6 cells, which express high levels of MGMT and have shown resistance to TMZ.[132] The use of primary cells is advantageous for drug screening since prolonged tissue culture can lead to phenotypic changes including loss of amplified epidermal growth factor receptor[133] and hypermethylation of DNA MGMT promoter[134] in GBM cell lines, which can significantly affect tumor response to treatment. Primary GBM xenografts avoid these issues by serial transplantation in mouse flanks to preserve important genetic features of the primary cell.[120] Thus, we established orthotopic human primary

GBM xenografts using luciferase expressing GBM6 cells maintained as flank tumors in mice. Orthotopic brain tumor growth could then be monitored through Xenogen IVIS luminescent imaging.

Prior to animal studies, CTX targeting of GBM6 cells was confirmed *in vitro* by flow cytometry. **Figure 3-9** shows GBM6 uptake of targeted CTX-AF647 and free AF647 control. Cells were incubated with CTX-AF647 or free AF647 at a 4 μM fluorophore concentration. At this concentration there was a nearly 3-fold increase of CTX-AF647 uptake as compared to free AF647, demonstrating ligand specific targeting of GBM6 cells by CTX.

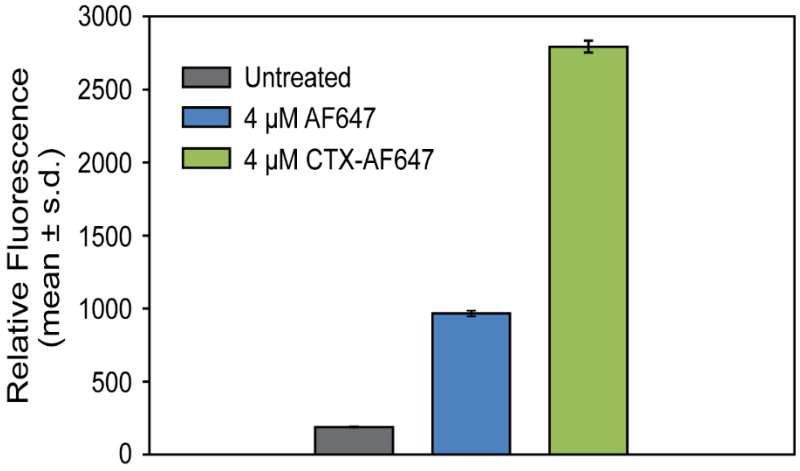

Figure 4-10. Flow cytometry analysis of AF647 internalization by primary GBM6 cells, 2 h post treatment with either free AF647 or CTX-AF647; also shown is the result for cells receiving no treatment (Untreated) as a reference.

Prior to treatment, SPIONs were suspended in 2.5% 400 MW PEG (w/w) and 2.5% dextrose (w/w), aliquoted at the predetermined treatment dose, and flash frozen in liquid nitrogen. The addition of PEG and dextrose was to both stabilize the SPION during freeze for storage and to increase viscosity, which has been shown to increase Vd of therapeutics when administered by CED.[135] Before each SPION treatment, SPIONs were quickly thawed and placed on ice until administered. NPCP-BG-CTX (5μL, 15 μg BG/kg) and NPCP-CTX (5μL, Fe

concentration equivalent to NPCP-BG-CTX dosage) were administered via CED 24 h prior to TMZ treatment (66 mg TMZ/kg, via oral gavage). The 24 h SPION pre-treatment time point was selected based on *in vitro* MGMT inhibition results that showed maximum MGMT inhibition at 24 h. CED was performed using a stereotaxic frame to securely hold the mouse and Hamilton syringe. A new burr hole was produced at the same location as for the tumor implantation and the tip of the Hamilton syringe was placed at a depth of 3 mm (tumor implant location) prior to infusion of 5 µL of SPIONs at 1 µL/min.

MR imaging was utilized to evaluate the extent of SPION delivery via CED. **Figure 3-10** shows T2-weighted transverse and sagittal images of (a) mice brain bearing GBM6 tumor without SPION treatment, as well as CED SPION injected tumors at (b) t = 0 h, (c) t = 24 h, and (d) t = 48 h after SPION treatment. Excellent SPION distribution was observed at all three time points. The outer edge of the injected margin at t = 0 was somewhat blurred (**Figure 3-10b**), but became significantly well-defined at t = 24 h (**Figure 3-10c**). To further examine the brain parenchyma outside the tumor capsule, T2*-weighted images, which are highly sensitive to small quantities of SPION, were acquired (**Figure 3-10e**). The red arrows in **Figure 4-11e** represent (at t = 0) the blurry outer SPION margin, (at t = 24 h) the highly defined SPION edge, and (at t = 48 h) the appearance of SPIONs in the process of elimination from the outer margin of the tumor. To best capture the behavior between 24 and 48 h, separate images were acquired with a short echo time (TE = 6 ms, **Figure 3-10f**). The short TE reduces the effects of SPION contrast and better displays the removal of SPION from the outer margin at 48 h post CED. We used a multi-spin multi-echo sequence to calculate the T2 value within this outer margin, in comparison to untreated tumor (**Figure 3-10g**). The quantitative results suggested that a significant quantity of SPION remained within the outer tumor margin at 48 h (red ROI). Conceptually, the early

extraction at 48 h of SPION from the outer tumor margin corresponds well to the known presence of extensive tumor perfusion within this area. The persistence of SPION within the small central region may thus correspond to the dysfunctional vascular and cytologic architecture of the necrotic core.

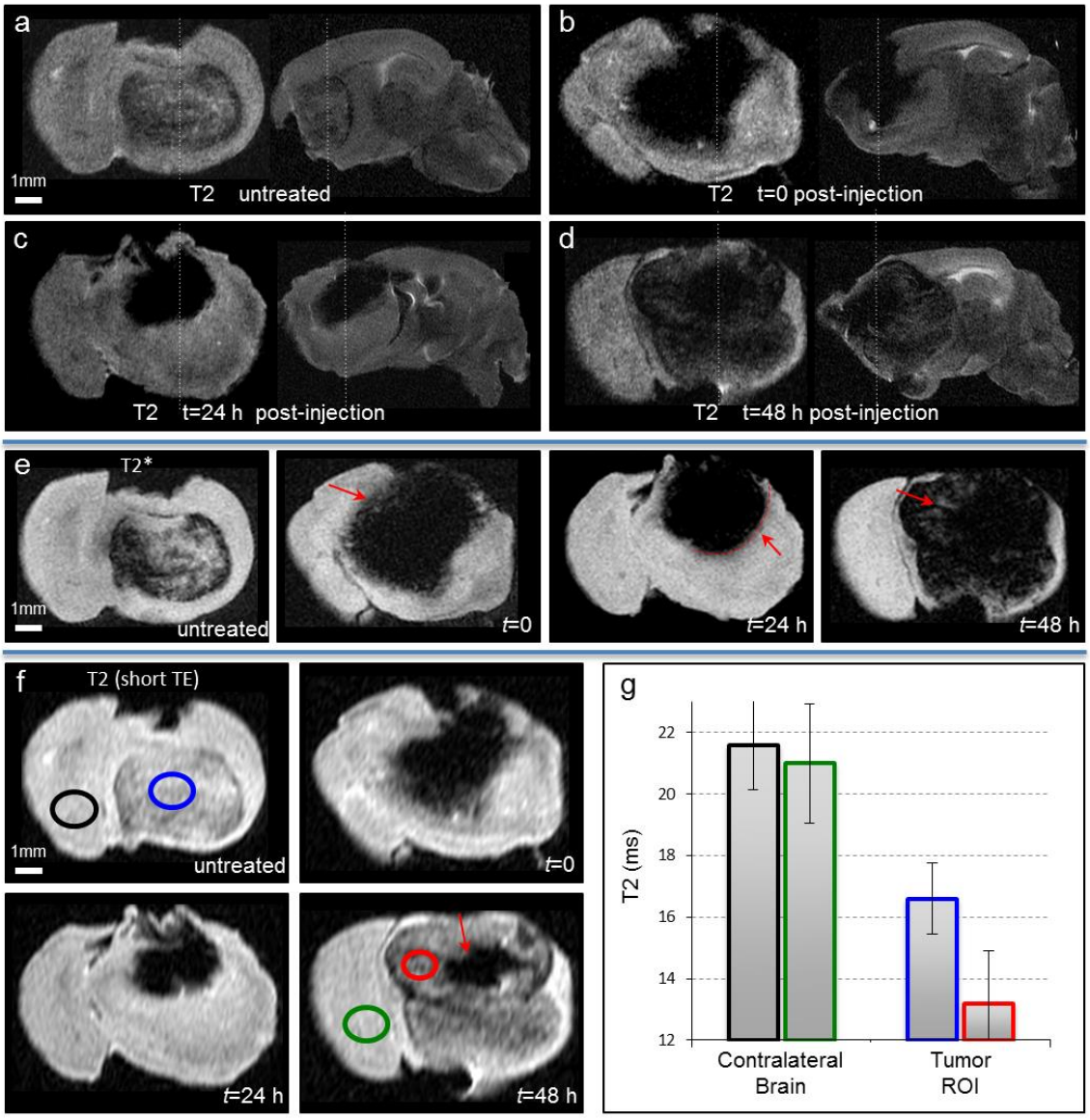

Figure 4-11. MR evaluation of CED delivery of NPCP-BG-CTX. Transverse and sagittal T2-weighted images of a mouse brain a) untreated, b) immediately after CED, c) 24 h after CED, and d) 48 h after CED. e) T2*-weighted images illustrating changes in SPION contrast margins at 0 h (red arrow indicates diffuse SPION contrast margin), 24 h (well-defined SPION contrast

margin) and 48 h (loss of SPION from outer margin inward) post CED. f) Quantitative T2-weighted images with short TE of an untreated animal, and 0, 24 and 48 h post CED of NPCP-BG-CTX. g) T2 relaxation time differences between untreated and 48 h post CED of NPCP-BG-CTX for contralateral brain and tumor ROI indicated a significant quantity of NPCP-BG-CTX remained in the outer tumor margin 48 h after treatment. Bar color outlines correspond to ROI outlines in (f).

NPCP-BG-CTX localization was further examined through histological analysis on brain sections near the tumor margin. After MR imaging, fixed brains (10% formalin) were embedded in paraffin, sectioned, and stained with Prussian blue and hematoxylin and eosin (H&E) (**Figure 3-11a and b**). The Prussian blue staining revealed the presence of NPCP-BG-CTX well beyond the tumor boundary immediately after CED, but confined within the tumor at 48 h post CED. **Figure 3-11c** displays a model for the behavior that we visualize here; upon completion of CED, NPCP-BG-CTX diffused outward beyond the tumor boundary. By 24 and 48 h, NPCP-BG-CTX cleared from the healthy brain and remained only within the tumor boundary. Both MRI and histology results confirm the successful delivery and distribution of NPCP-BG-CTX throughout the tumor, validating CED as a promising mode of delivery for these SPIONs.

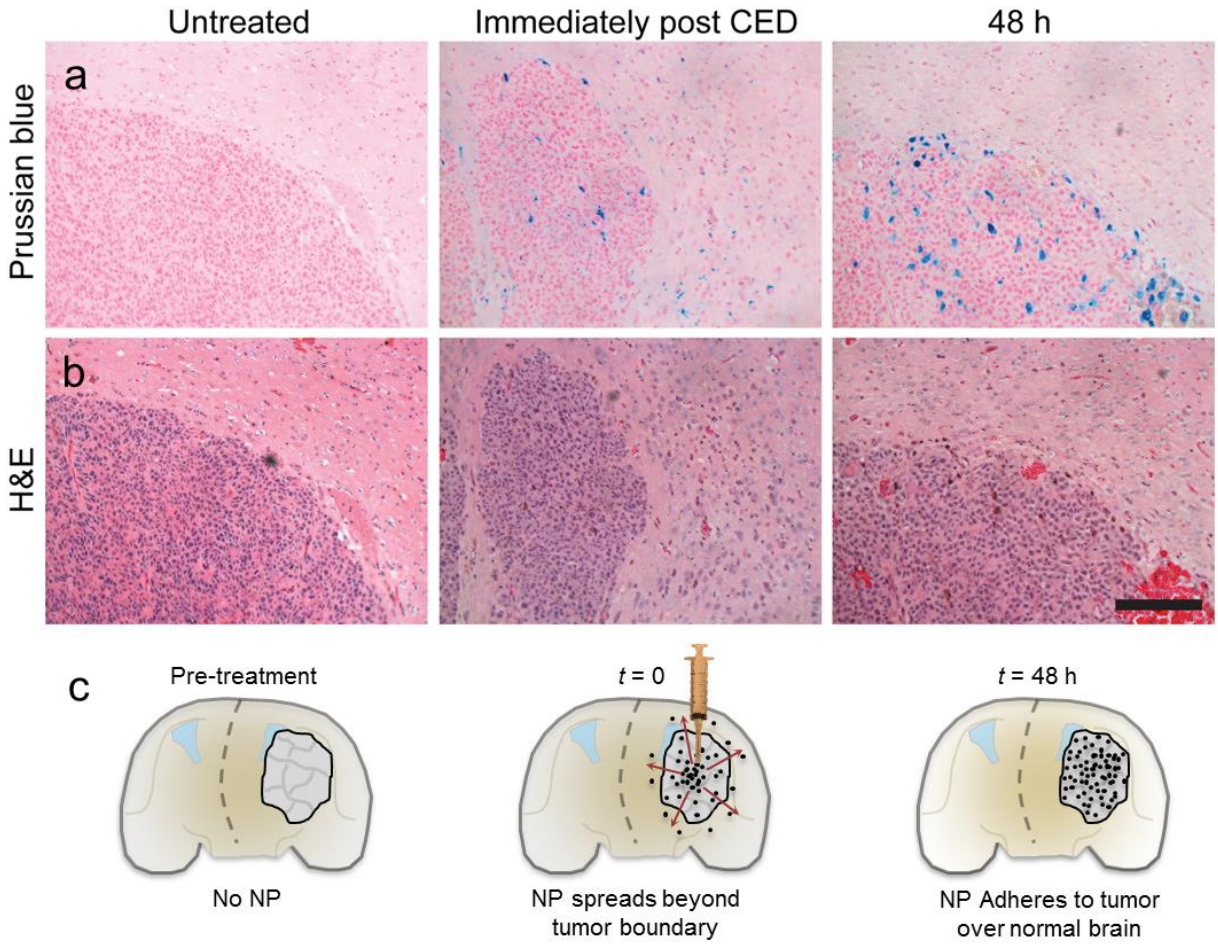

Figure 4-12. NPCP-BG-CTX is preferentially retained in the tumor region. a) Representative Prussian blue and b) H&E stained subsequent tissue sections of brain at the tumor margin obtained from untreated or NPCP-BG-CTX treated animals immediately post CED or 48h post CED. The scale bar corresponds to 100 μm. c) Schematic illustration of time dependent changes of SPION localization before and after CED.

In vivo efficacy of NPCP-BG-CTX in combination with TMZ was compared to control NPCP-CTX in combination with TMZ and animals that received no treatment. Treatments were administered twice weekly for two weeks **(Figure 3-12a**). Overall median survival was determined with the first treatment day as day 0 and a log rank statistical analysis of the Kaplan-Meier plot was performed (**Figure 3-12b and c**). Animals treated with NPCP-BG-CTX/TMZ showed a three-fold increase in survival as compared to untreated animals and had a median

survival time of 9 days in comparison to 4 days for NPCP-CTX/TMZ, and 3 days for untreated animals. The log rank statistic for comparison between NPCP-BG-CTX/TMZ and untreated animals showed a statistical increase in survival probability for mice receiving NPCP-BG-CTX/TMZ ($P = 0.0003$). Importantly, the log rank statistic for survival probability comparison between NPCP-BG-CTX/TMZ and NPCP-CTX/TMZ showed a statistically significant difference ($P = 0.009$) between the groups. There was no statistical difference in survival probability between NPCP-CTX/TMZ treated and untreated animals ($P = 0.7$). These results indicate that the prolonged time of survival for NPCP-BG-CTX/TMZ treated animals was caused by the therapeutic effect of BG on the SPION polymer surface and was not induced by local SPION toxicity.

In the above experiments we demonstrated that a BG loaded SPION formulation engineered with proper size and surface chemistry can be administered by CED to achieve excellent tumor coverage and increase median survival in an orthotopic primary GBM xenograft model. In addition to holding a potential role in the up-front treatment of malignant glioma, the clinical promise for CED agents extends to the adjunct treatment of recurrent tumors, and of those deemed inoperable due to deep location in the brain. Especially in the setting where re-operation or re-irradiation ceases to provide clinical benefit, novel therapeutic technologies such as ours may play an important role in improving survival or providing symptomatic relief.[136] We envision a single needle-based injection, or a stereotactically implanted microcatheter-based infusion, to provide a localized high concentration of our compound to the active site of such tumors. As we have shown with MRI and histology, NPCP-BG-CTX permeates outside the tumor margin immediately after delivery, but becomes rapidly confined to the tumor region, with the SPION persisting within tumor for at least 48 h.

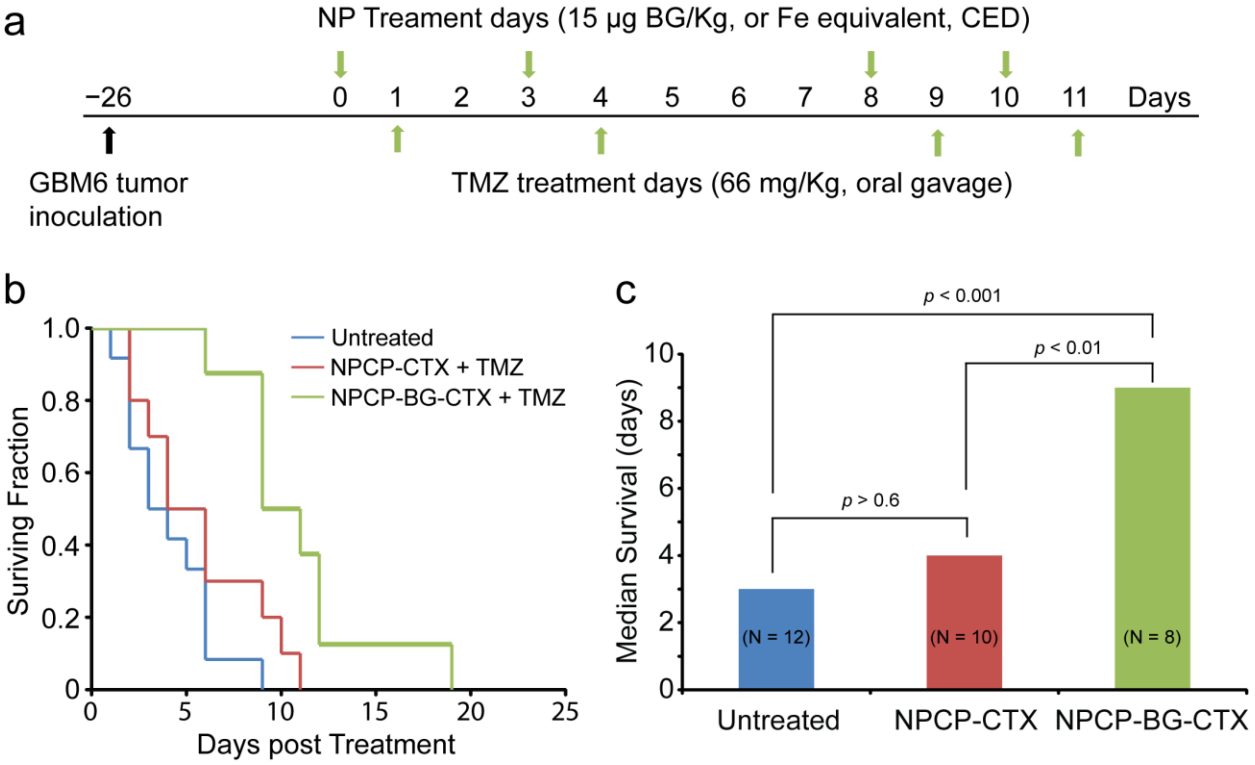

Figure 4-13. Increased survival by CED of NPCP-BG-CTX in combination with TMZ in an orthotopic GBM6 xenograft model. a) Tumor inoculation and treatment time-line. SPIONs were administered 24 h prior to TMZ treatment. Treatments were performed twice weekly for two weeks. b) Kaplan-Meier survival curve. c) Median survival and log rank statistical comparison of the three treatment groups.

4.3.5 NPCP-BG-Cy5.5-CTX in vivo serum half-life, biodistribution and BBB permeability

For assessment of serum half-life, we used a reproducible, quantitative assay that utilized the NIRF dye, Cy5.5, which was incorporated into the nanoparticle as we previously reported.[75] Mice were injected through tail vein with 200µL of 1 mg/ ml NPCP-BG-Cy5.5-CTX (n = 3 for each time point) and blood was collected from mice at 1, 8, and 24 h. Blood was centrifuged and the plasma was collected for analysis. The blood plasma was added to a 96 well clear bottom

plate and scanned using an Odyssey scanner. Exponential decay analysis of the fluorescent signal from NPCP-BG-Cy5.5-CTX over time revealed an elimination half-life of 5 h (**Figure 3-13a and b**). This is significantly longer than the 1.2 h reported in literature for BG evaluated in rodent models. [111b]

The biodistribution of the mice receiving NPCP-BG-Cy5.5-CTX was determined by *ex vivo* NIRF signal quantification of excised tissues (brain, liver, spleen, kidney, heart and lung) (**Figure 3-13c and d**). Wild type mice were chosen for their intact immune system. Mice were injected (n = 3) through the tail vein with 200 µl of 1 mg/ml of NPCP-BG-Cy5.5-CTX. Whole organs were removed at 120 h after injection, frozen in OCT, and then sliced in 12 µm sections and mounted on glass slides. The slides were scanned on the Odyssey NIR scanner and images were obtained using the 700 nm channel (**Figure 3-13c**). The measured fluorescence intensities were then plotted to determine a biodistribution profile (**Figure 3-13d**). No marked nanoprobe accumulation was observed in brain, heart, and lung tissue. Conversely, significant accumulation of the NPCP-BG-Cy5.5-CTX was observed in clearance organs including liver, spleen, and kidney. These results are comparable in distribution profile to those reported for other iron oxide nanoparticle systems.[137]

To evaluate BBB permeability of NPCP-BG-CTX, analysis was performed on mouse brain sections three hours after SPION administration. Gross examination was first performed on 12 µm thick brain sections using odyssey scanner assays described above to monitor biodistribution (**Figure 3-13e**). Images obtained from three mice show distribution of nanoparticles throughout the entire brain with markedly higher intensities noticeable in blood vessels. As a control, brain tissue from mice receiving no injection is also displayed to verify that the signal is not from tissue auto fluorescence. The extravasation of nanoparticles from blood

vessels was further confirmed through immunohistological analysis of mouse brain sections (**Figure 3-13f**). The presence of fluorescent signal in the brain's extracellular matrix of wild-type mice further supports the ability of these particles to escape the neural vasculature.

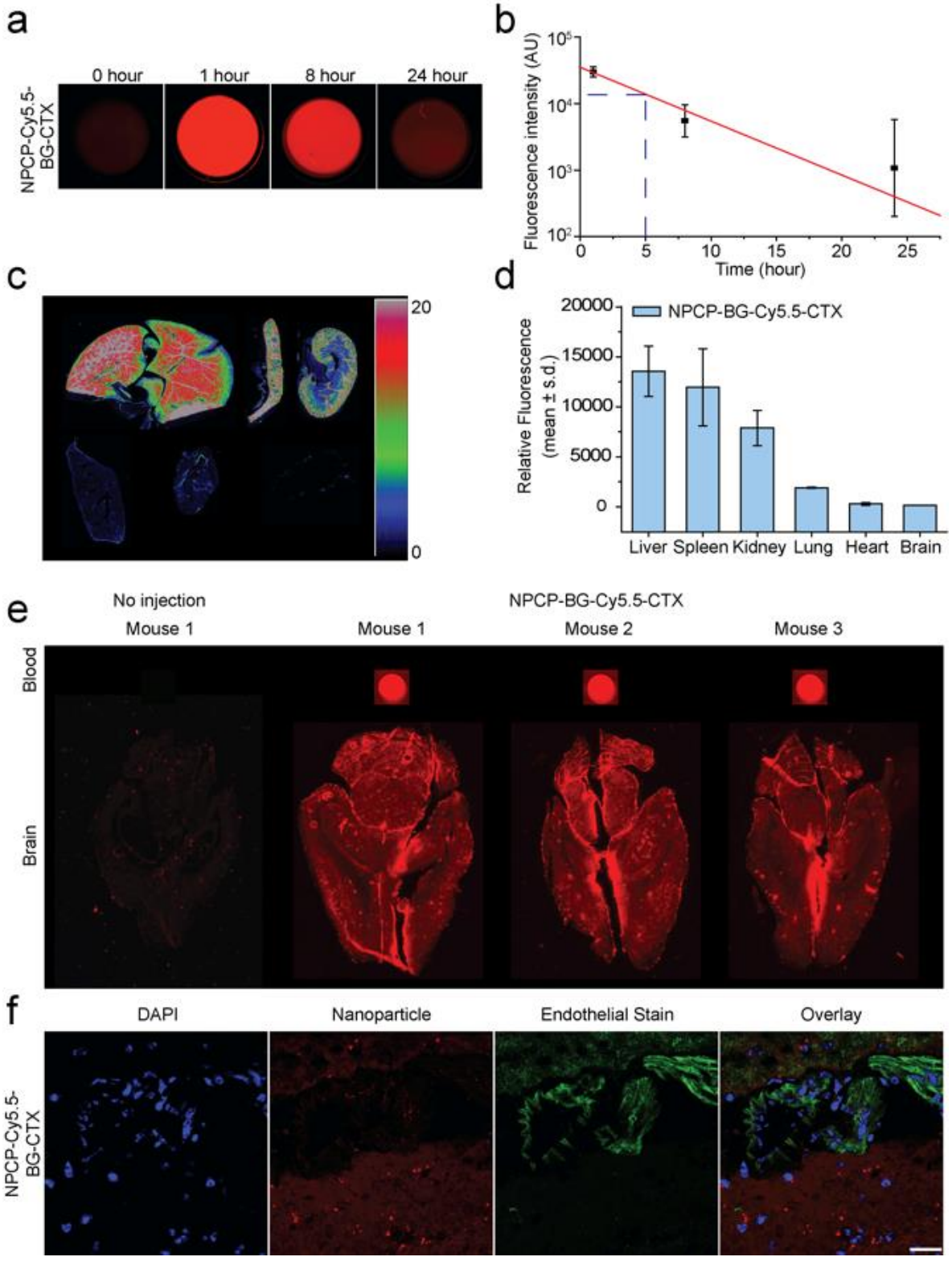

Figure 4-14. Serum and organ biodistribution profile of NPCP-BG-CTX in wild type mice. a) Measured fluorescence intensity of nanoparticles in serum. b) Serum half-life of NPCP-BG-CTX

determined using fluorescence measurements. Each data point represents the mean fluorescence intensity integrated above the baseline. The curve indicates an exponential decay curve fit to the data (n = 3 mice per time point). c) Fluorescence image of 12-micron sections of various organs five days post injection, obtained using the Odyssey imaging system. The spectrum gradient bar corresponds to relative fluorescent level. (Top row, from left to right: Liver, Spleen, and Kidney. Bottom row from left to right: Lung, Heart, and brain). The spectrum gradient bar corresponds to the relative fluorescence intensity unit p/sec/cm2/sr × 10^3. (d) Quantitative representation of the biodistribution of NPCP-BG-CTX. (e and f) Fluorescence-based BBB permeability assay. Shown are representative images of brains of wild-type mice receiving no-injection or tail vein injections of NPCP-BG-CTX. The mice were sacrificed at 3 h after treatment. e) Fluorescence image of 12-micron sections of mice brain and 100× dilution of blood in 96 well plate scanned using the Odyssey imaging system. f) Histological examination of nanoparticle permeability across the BBB. Cell nuclei (blue; DAPI) and endothelial cells (green; FITC-PECAM-1) were stained to visualize the localization of nanoparticles (red) within the brain tissue. The scale bar in the confocal images corresponds to 20 μm.

4.3.6 NPCP-BG-CTX pharmacological evaluation

Tissue specific toxicity was examined through histological analysis on various tissues (kidney, spleen, liver, and brain) of mice injected with NPCP-BG-CTX to identify any signs of acute toxicity. Tissues were harvested from mice 120 h after receiving nanoparticle injection, fixed in 10% formalin, embedded in paraffin, sectioned, and stained with hematoxylin and eosin (H&E). Tissue sections showed no evidence of toxicity, appearing similar to those observed in the tissues from PBS injected control animals (**Figure 3-14a**).

Since the accumulation of nanoparticles in liver have been reported[66b] and shown with NPCP-BG-CTX, potential toxicity of the accumulated SPIONs to liver was assessed by a hepatotoxicity assay. Serum aspartate aminotransferase (AST) and alanine aminotransferase (ALT) levels were determined in mice injected with NPCP-BG or PBS (**Figure 3-14b**). No marked elevation of AST and ALT levels was found in mice receiving NPCP-BG-CTX compared to control mice receiving PBS injection, suggesting that SPIONs do not induce liver toxicity at the given dosage.

A major concern associated with combinational therapy of brain tumors through co-administration of BG and TMZ is dose limiting chemotherapy-induced bone marrow toxicity.[110, 138] In the clinic, chemotherapy induced myelosuppression is detected through blood work by the decrease in the number of white blood cells (neutropenia) and platelets (thrombocytopenia).[139] To monitor whether co-administration of TMZ with NPCP-BG-CTX is more tolerable in mice compared to BG, we evaluated the influence of each formulation on white blood cell (WBC) and platelets levels in peripheral blood (**Figure 3-14c and d**). Mice were injected with NPCP-BG at a BG dose of 6 mg/kg followed two hours later by an injection of 66 mg/kg TMZ and sacrificed 5 days later. Mice receiving PBS and free BG injections were also included in our study as controls. Peripheral blood was collected through cardiac heart puncture. BG/TMZ produced almost complete knockdown of WBC and platelet levels indicating substantial neutropenia and thrombocytopenia. Importantly, NPCP-BG-CTX/TMZ produced significantly lower degrees of WBC and platelet suppression compared to BG/TMZ treatments indicating they do not accumulate in the bone marrow, as we have shown with a similar CTX-targeted nanoparticle.[66b]

Combined, these findings suggest that NPCP-BG-CTX produced less myelosuppression and were more tolerable when combined with TMZ as compared to free BG. The decrease in myelosuppression is likely due to the favorable biodistribution of these SPIONs. We anticipate that NPCP-BG-CTX will be more tolerable than free BG when combined with TMZ and decrease the dose limiting chemotherapy-induced myelosuppression often observed in the clinic.

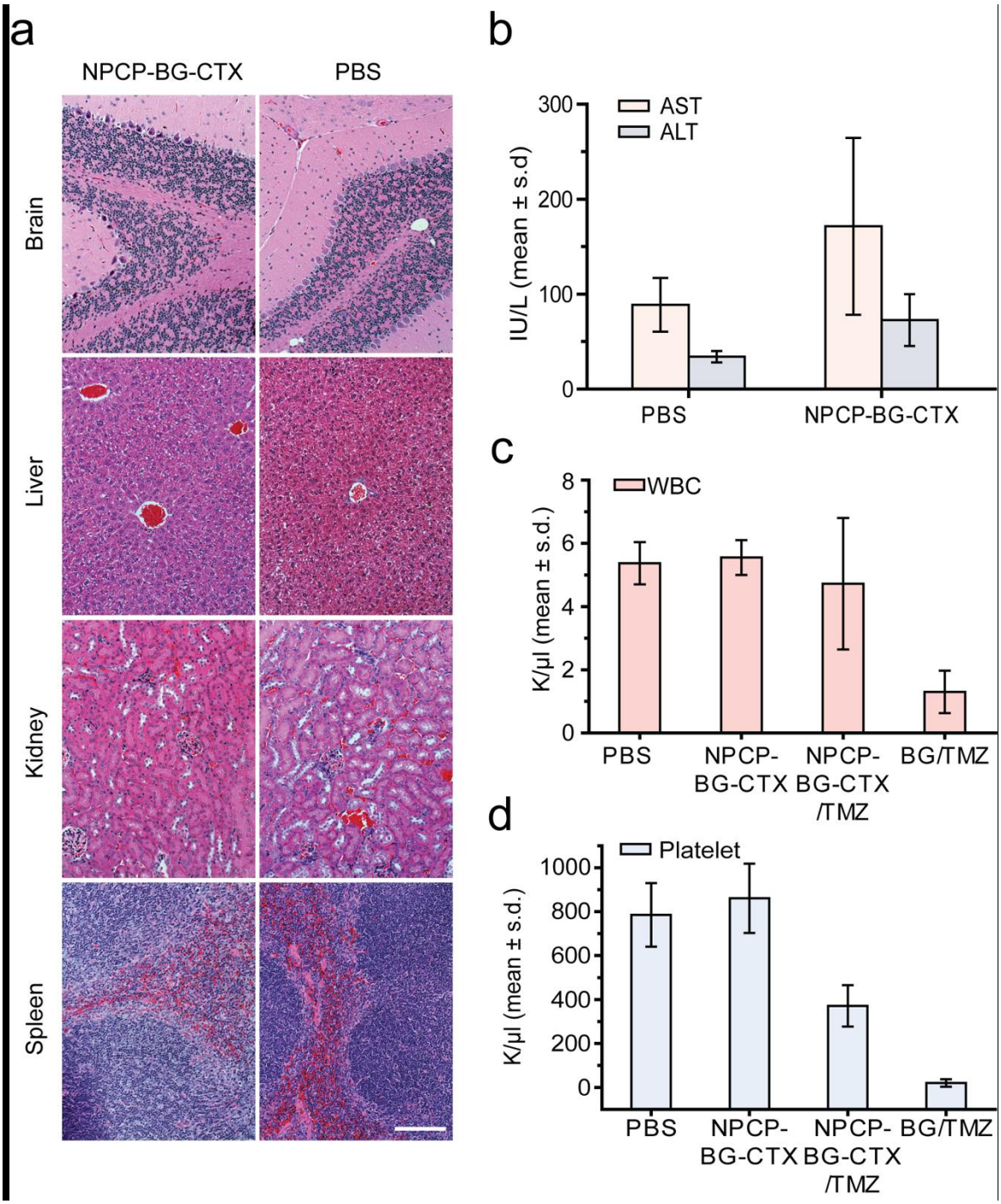

Figure 4-15. Pharmacological evaluation of NPCP-BG-CTX. a) Representative H&E stained tissue sections of mouse liver, kidney, spleen, and cerebellum obtained from PBS injected animals and from those injected with NPCP-BG-CTX. Scale bar corresponds to 150 µm. b) Assessment of toxic effects of NPCP-BG-CTX on liver. AST and ALT levels of mice receiving NPCP-BG-CTX or PBS injection were measured five days after administration (mean ± standard deviation of the mean, n =3 mice per treatment). (c and d) Evaluation of bone marrow toxicity in response to co-administration of BG and TMZ. c) White blood cell counts obtained from wild type mice 5 days post treatment with PBS, NPCP-BG-CTX/TMZ, or BG/TMZ. d) Platelet counts

obtained from wild-type mice 5 days post treatment with PBS, NPCP-BG-CTX/TMZ, or BG/TMZ.

4.4 Conclusions

GBM targeted SPIONs carrying a BG payload were successfully prepared. These SPIONs had excellent solubility and physicochemical properties, and demonstrated a redox-responsive drug release profile. *In vitro* evaluation of NPCP-BG-CTX demonstrated proper release and trafficking of BG within human GBM cells. NPCP-BG-CTX treated human GBM cells showed significant reduction of MGMT activity similar to free BG treated cells. In addition, NPCP-BG-CTX mediated suppression of MGMT was accompanied by significantly greater sensitivity to TMZ in human GBM cells. Pharmacological evaluations showed there was no difference in liver toxicity between saline injected and SPION injected mice indicating the innocuous toxicity profile of NPCP-BG-CTX. Co-treatment of wild type mice with NPCP-BG-CTX and TMZ was much better tolerated than treatment with free BG combined with TMZ, which produced significant myelosuppression. NPCP-BG-CTX was successfully administered by CED and produced excellent distributions within the brain tumor. The clearly delineated contrast provided by NPCP-BG-CTX in MR images displayed the potential for real-time monitoring of drug delivery. In combination with TMZ, NPCP-BG-CTX increased median overall survival 3-fold over untreated animals. Combined, these findings warrant further optimization and evaluation of NPCP-BG-CTX as a viable adjunct to the current clinical treatment of patients with MGMT expressing GBMs.

5 pH Sensitive Therapeutic Polymer Modified Magnetic Nanoparticles for Increased Drug Loading

Nanoparticle-mediated delivery of chemotherapeutics has demonstrated potential in improving anti-cancer efficacy. Yet, sub-optimal drug loading, particularly for solid core nanoparticles (NPs), remains a challenge that limits the application of these formulations in the clinic. The addition of the hydrophobic drug O^6-benzylguanine (BG) as an adjuvant treatment of Glioblastomas (GBMs) has shown potential to improve the dismal prognosis of this devastating disease, however, current clinical formulations suffer from poor pharmacokinetics. Nanoformulations that can improve water solubility and controlled release provide a solution to these clinical challenges. In this study we formulated ribose modified BG, O^6-benzylguanosine (BGS) to achieve high drug loading while maintaining SPION stability. The base nanovector consists of an iron oxide core (9 nm) coated with hydrazide functinalized PEG (IOPH). Di-aldehyde modified BGS and PEG-dihydrazide was polymerized on the SPION surface (IOPH-pBGS) through acid-labile hydrazone bonds. Successful BGS polymerization was confirmed by FTIR and quantitated by UV-vis spectrascopy. IOPH-pBGS demonstrated excellent drug loading of 38.3 ± 2.9% by weight while maintaining adequate size for *in vivo* navigation (36.5 ± 1.8 nm). Drug release was monitored under physiological and intracellular conditions (pH 7.4 and 5.5 respectively) and showed pH dependent release. Importantly, IOPH-pBGS significantly suppressed activity of DNA repair protein O^6-methylguanine-DNA methyltransferase (MGMT) *in vitro*. These results demonstrate the potential of IOPH-pBGS to address current limitations of clinical treatment of GBMs.

5.1 Introduction

GBMs are highly aggressive, infiltrative brain tumors affecting 14,000 individuals a year in the United States.[106] GBMs present many treatment challenges; the tumor is afforded variable protection within the blood-brain barrier (BBB) and can develop chemoresistance due to efflux and upregulation of DNA repair factors.[140] Even with aggressive treatment comprising surgery, chemotherapy and radiation, mean survival is 12-15 months,[141] with a 5-year survival of < 5%.[142] The DNA methylating agent temozolomide (TMZ) has become the standard-of-care but the majority of patients suffer from resistance inferred by MGMT, a DNA repair protein that eliminates the cytotoxic O^6-methylguanine DNA lesions produced by TMZ.[108] GBM resistance to TMZ may in theory be mitigated by inclusion of MGMT inhibitors such as BG,[109] however, incorporation of conventional BG formulations in TMZ drug regimens reduces the maximum tolerated dose of TMZ by 50%, leads to significant meyolosupression and has shown no significant increase in survival or quality of life.[110]

Recent advances in nanotechnology have provided tools to address the limitations of current chemotherapeutic treatments of GBM. Nanoparticle (NP) drug formulations can increase blood circulation time, protect therapeutic payloads, mitigate resistance to drug efflux, provide controlled drug release, and minimize off-target accumulation of drug.[95, 143] Previously, our group reformulated BG in combination with a redox-responsive theranostic SPION platform to improve its intracellular delivery to GBM cells while minimizing its localization to healthy tissue.[143] This improved BG formulation demonstrated significant reduction in MGMT activity and potentiated TMZ cytotoxicity *in vitro* while increasing survival 3-fold over untreated controls in an orthotopic primary human GBM xenograft mouse model. However, the relatively low drug loading of this nanoparticle BG formulation required site specific administration via

intratumoral convection enhanced delivery (CED) to achieve efficacious intratumoral drug concentrations. While CED is emerging as a promising drug administration technique, it is highly invasive and requires surgical expertise. Increased drug loading may allow for intravenous injection that would simplify administration and mitigate potential CED side effects.

A major constraint of drug loading with solid core NPs is the limited surface area and reactive sites for conjugation of chemotherapeutic drugs. The number of reactive sites on an NP surface is typically the limiting factor for covalent drug loading as only one chemotherapeutic molecule can be bound at each NP reactive site. Additionally, increased loading of drugs with poor water solubility may destabilize the NP formulation leading to greater hydrodynamic size and shorter serum half-life, hampering performance *in vivo*.[144] Chemical modification of existing chemotherapeutic drugs can increase water solubility and provide means to polymerize the drugs on the surface of solid core NPs, thereby increasing drug loading while maintaining NP stability.

In addition to ensuring high drug loading, a challenge in developing drug carrier NP formulations is providing rapid intracellular release of drugs in target cells while minimizing release in the blood. Many strategies have been explored to create NP formulations that respond to environmental stimuli such as temperature, pH, ionic strength, redox potential, and electrical or magnetic fields.[89, 123] Reversible hydrazone linkages formed by reaction of hydrazides with ketones or aldehyde functionalities have been extensively studied as a pH responsive mechanism for controlled intracellular release of doxorubicin.[145] These formulations have shown favorable release profiles, minimizing release at physiological pH, yet exhibiting controlled degradation of drug linkages at intracellular pH, demonstrating the potential of this chemistry in cancer treatment.

Here we report the development of a new SPION formulation for delivery of a ribose modified BG, O^6-benzyl guanosine (BGS), comprised of a superparamagnetic iron oxide core coated with a polymer shell of polyethylene glycol (PEG) functionalized with hydrazide end groups for polymerization of homobifunctional dialdehyde BGS (DA-BGS) via hydrazone linkages. DA-BGS was produced through oxidation of the ribose moiety to yield two aldehyde functional groups for reaction with hydrazide functionalized SPIONs and with homobifunctional PEG hydrazide to allow polymerization off the SPION surface. SPION size, zeta potential, drug loading and release kinetics, and *in vitro* ablation of MGMT activity were evaluated and compared against free BG and BGS. Importantly, this new polymerized BGS SPION formulation may provide a less invasive, yet more effective treatment strategy than current clinical treatment methods and lead to improved clinical outcomes.

5.2 Experimental

5.2.1 Materials

All chemicals were purchased from Sigma-Aldrich (St. Louis, MO, USA) unless otherwise specified. 3-(triethoxysilyl)propyl succinic anhydride (SATES) was purchased from Gelest (Arlington, VA, USA). 2000 MW mono-amine functionalized polyethylene glycol ($mPEG_{2K}$-NH_2) was purchased from Laysan Bio (Arab, AL, USA). 600 MW hydrazide-PEG-hydrazide ($PEG_{600}DH$) was purchased from Creative PEGWorks (Chapel Hill, NC, USA). O^6-Benzylguanosine (BGS) was purchased from Toronto Research Chemicals (Toronto, ON, Canada).

5.2.2 IOPH synthesis and coating

Oleic acid coated iron oxide particles were synthesized following previously reported procedure.[46] 50 mg of IOOA was suspended in 43 ml of anhydrous toluene followed by addition of 50 µl of triethylamine in a 3 neck round-bottom flask fitted with a Graham condenser and a vacuum adapter. The flask was sealed with rubber septa and purged with nitrogen before heating the solution to 100°C. SATES (100 µl) was added to the flask. $mPEG_{2K}$-NH_2 (187.5 mg) was dissolved in 7 mL of anhydrous toluene and was added to the flask 15 minutes after the addition of SATES. An additional 50 µl of SATES was injected 1 h after the $mPEG_{2K}$-NH_2 injection, and the solution was reacted for a further 6 h and 45 minutes. The solution was transferred to a single neck round-bottom flask and SPIONs were precipitated with hexane. The SPION precipitate was dispersed in tetrahydrofuran (THF), sonicated for 10 minutes, and precipitated with hexane. The resulting SPION pellet was suspended in 10 ml anhydrous THF and sonicated for 10 minutes. 102.5 mg of $mPEG_{2K}$-NH_2 and 160 mg of PEG_{600}-DH was dissolved in 12 ml anhydrous THF and added to the SPION solution. The flask was then sealed with a septum and purged with nitrogen. 12.5 mg of N,N^1-dicyclohexylcarbodiimide (DCC) was dissolved in 2 ml anhydrous THF and added to the flask, and the reaction solution was placed in a sonication bath at 25°C and allowed to react for 16 h. Fully PEGylated SPIONs were precipitated with hexane, redispersed in 20 ml ethanol, sonicated for 10 minutes, and precipitated again with hexane. The pellet was fully dried and dispersed in PBS with sonication for 10 minutes. The particles were purified through size exclusion gel chromatography.

5.2.3 Synthesis of DA-BGS

O^6-Benzylguanosine (BGS) was dissolved in DMSO (26.78 mM) before being mixed at an equal volume ratio with an aqueous $NaIO_4$ solution (3.17 M). The mixture was protected from light and reacted overnight on a rocker.

5.2.4 IOPH-pBGS synthesis

Aqueous IOPH (1 mg, 6.676 mg/mL) was diluted in aqueous MES buffer (123 mM, 594 μL). cBGS (5 mg/mL, 133 μL) was titrated in at a constant rate of 10 mL/min. Titration of PDH (6.45 μg/μL, 66.7 μL) started after half of the BGS had been added. After the completion of titration, the reaction mixture was protected from light and allowed to react at room temperature for an additional two h before purification through a size exclusion column. Purified particles were collected and analyzed for size, zeta potential, and drug loading using UV and NMR.

5.2.5 SPION size and zeta potential characterization

Hydrodynamic size and zeta potential of IOPH and IOPH-pBGS was analyzed at 100 μg/mL in 20 mM HEPES buffer (pH 7.4) using a DTS Zetasizer Nano (Malvern Instruments, Worcestershire, UK).

5.2.6 TEM characterization of SPION core size and morphology

TEM images were acquired with an FEI TECNAI F20 TEM (Hillsboro, OR) operating at 200 kV. SPION core diameters were analyzed with ImageJ software and the size distribution, mean diameter and standard deviation was calculated from 100 SPION measurements.

5.2.7 Evaluation of BGS loading

Absolute quantization of drug loading on each particle was determined though both UV absorbance and HPLC quantization. IOPH-BGS (50 μg) was freeze dried and resuspended in a solution of propanoic acid hydrazide in 50 mM MES buffer (125 μL, 10 mg/mL). The solution was sonicated for seven hours before filtration through a 10k MWCO spin filter (12 rcf for 15 minutes). The supernate (25 μL) was added to an equal volume of BGS standard and the volume brought up to 200 μL with deionized water. UV absorbance was measured at 280 nm and total concentration calculated.

5.2.8 Drug release

IOPH-BGS (2 mg) was dialyzed using a 10k MWCO slide-a-lyzer mini dialysis cassette against 15 mL of MES (50 mM) pH 5.0 and 6.0 as well as DPBS (pH 7.4) held at a constant 37.0 C. Aliquots (1 mL) were removed at specified time points and measured for UV absorbance (280 nm). The volume against which dialysis occurred was held constant by adding back the removed volume of media for each condition. Absorbance for each sample was converted to concentration using a standard curve.

5.2.9 Cell culture

SF767, a human GBM cell line obtained from the tissue bank of the Brain Tumor Research Center (University of California–San Francisco, San Francisco, CA), was maintained in DMEM supplemented with 10% FBS and 1% antibiotic-antimycotic at 37 ºC and 5% CO_2.

5.2.10 MGMT activity Assay

The MGMT activities of protein extracts of human GBM SF767 cells were measured in a standard biochemical assay that quantifies the transfer of radioactivity from a DNA substrate containing [methyl^{3}H]O^6-methylguanine (specific activity, 80 Ci/mmol) to protein, as detailed previously.[117] SF767 cells (2×10^6) were plated in 100 mm dishes and incubated with 10 µM free BG for 2 or 24 h with IOPH-pBGS equivalent to 10 µM BG in fully supplemented medium. After incubation, cells were washed with PBS, collected, and protein extracts were prepared. The protein extract supernatant was prepared by dissolution of washed SF767 pellets of known cell number with non-ionic detergents in the presence of 600 mM NaCl.[118] Aliquots of crude homogenate were saved for DNA determination by the diphenylamine method that measures deoxyribose following degradation of DNA with heat and acid.[119] Crude homogenate was cleared by centrifugation at 10,000 × g for 30 min. Activity, normalized to cell number using a conversion factor of 6 pg DNA per cell, is fmol O^6-methylguanine transferred per 10^6 cells.

5.3 Results and discussion

5.3.1 Formulation and characterization of SPIONs

An overview of the synthesis scheme for PEG coated, hydrazide functionalized nanoparticles (IOPH) surfaced polymerized with DA-BGS (IOPH-pBGS) is illustrated in **Figure 4-2a**. IOPH consists of a 9 nm iron oxide core coated with PEG/PEG-hydrazide and was synthesized from oleic acid coated SPIONs produced through thermal decomposition of iron-oleate complexes. The hydrophobic oleic acid coating was replaced with a hydrazide functionalized PEG monolayer to render the SPIONs water soluble via an established ligand exchange process[54b] modified by replacing di-amine functionalized 2000 MW PEG with 600

MW PEG di-hydrazide (PDH). It should be noted that the carrier's core material, iron oxide, is biocompatible and biodegradable, and enables the monitoring of drug trafficking and delivery by magnetic resonance imaging (MRI) when administrated both *in vitro* and *in vivo*. The lower MW hydrazide functionalized PEG was chosen to allow polymerization of BGS within the 2000 MW PEG layer, minimizing crosslinking and improving IOPH-pBGS water solubility. To facilitate polymerization of BGS on the SPION surface, di-aldehyde groups were introduced by cleaving the carbon-carbon bonds between vicinal diols of the ribose moiety with sodium periodate (**Figure 4-1**). DA-BGS and PDH were slowly added drop-wise with offset start times into IOPHs in MES buffer pH 5.5, reacted for 2 h before addition of propanoic acid hydrazide (PAH) as an end capping group (**Figure 4-1b**). The formation of pH sensitive hydrazone bonds that allow for degradation of pBGS under acidic conditions are highlighted in yellow.

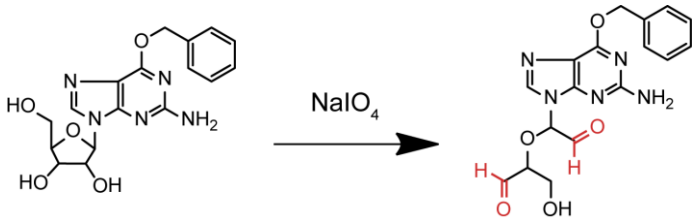

Figure 5-1. BGS is modified with dialdehyde functional groups by oxidation of the ribose moiety with sodium periodate. Sodium periodate specifically cleaves the carbon-carbon bond between vicinal diols and oxidizes the diols to aldehydes.

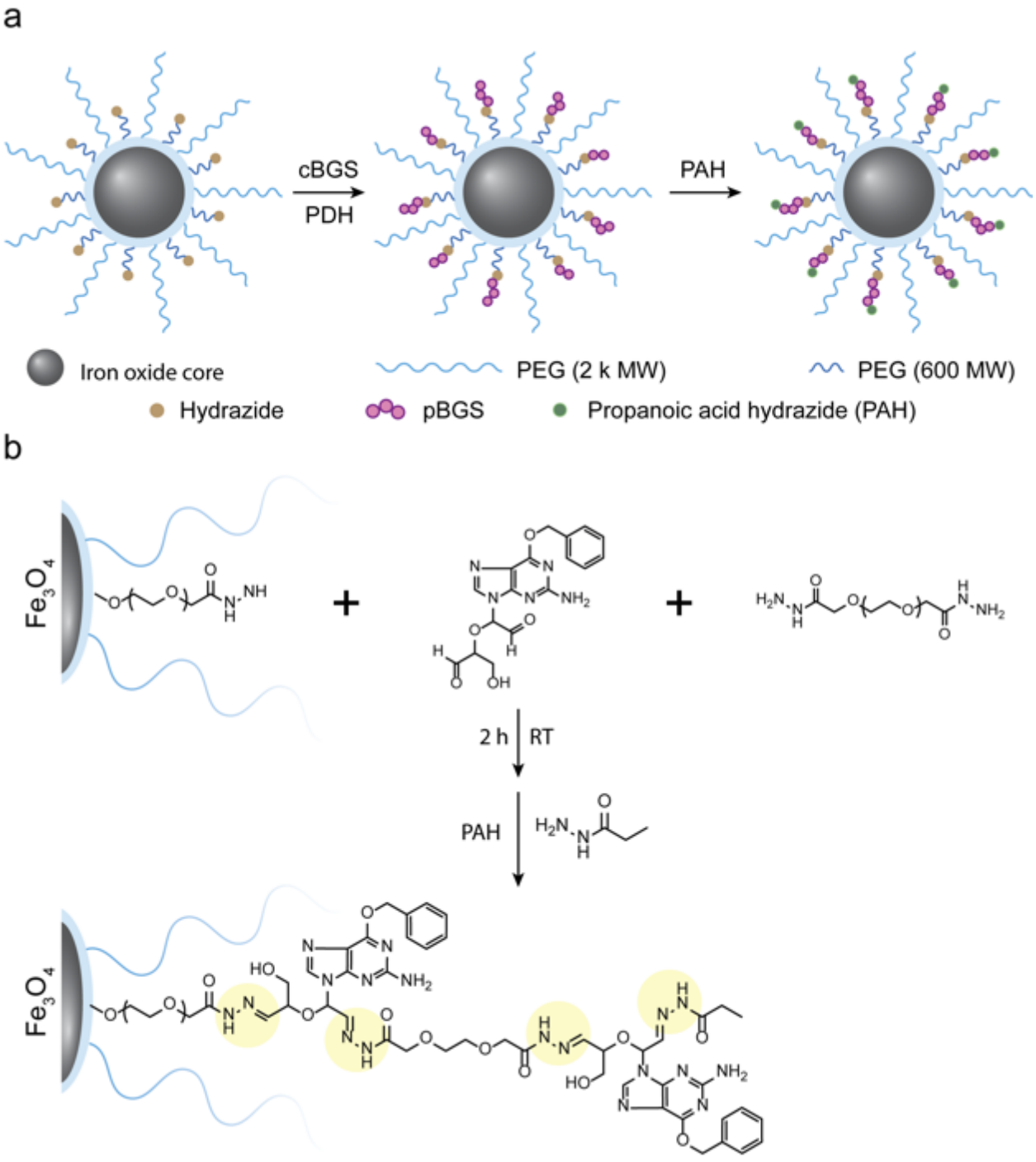

Figure 5-2. Synthesis of IOPH-pBGS. a) Illustrative overview of IOPN-pBGS synthesis. b) Chemical detail of BGS polymerization on IOPH surface. Acid-labile hydrazone linkages are highlighted in yellow.

Transmission electron microscopy (TEM) images showed that IOPH-pBGS maintained spherical morphology with core sizes of roughly 9 nm after ligand exchange to produce PEG coated water soluble SPIONs and with the addition of pBGS (**Figure 4-3a, c)**. Importantly, no aggregation was observed in IOPH and IOPH-pBGS indicating that no interparticle crosslinking was produced during PEG coating or BGS polymerization.

Hydrodynamic size and zeta potential are primary factors that determine the pharmacokinetic behavior of SPIONs *in vivo*.[59a, 146] IOPH and IOPH-pBGS had an average hydrodynamic size of 26 ± 2 nm and 36.5 ± 1.8 nm in HEPES buffer, pH 7.4, respectively, which falls within the appropriate range for evasion of the mononuclear phagocyte system (**Figure 4-4d**).[56a] Zeta potential plays a key role in non-specific SPION interactions with cell surfaces and extracellular matrices. Highly positively charged SPIONs preferentially interact with negatively charged cell surfaces whereas highly negatively charged SPIONs preferentially interact with positively charged extracellular matrices.[122] With this in mind, it is preferential for zeta potential to be near neutral. The mean zeta potentials of IOPH and IOPH-pBGS was determined in HEPES buffer pH 7.4 and was found to be slightly negative at −12.1 ± 14.2 mV and −11.8 ± 4.0 mV, respectively (**Figure 4-3e**).

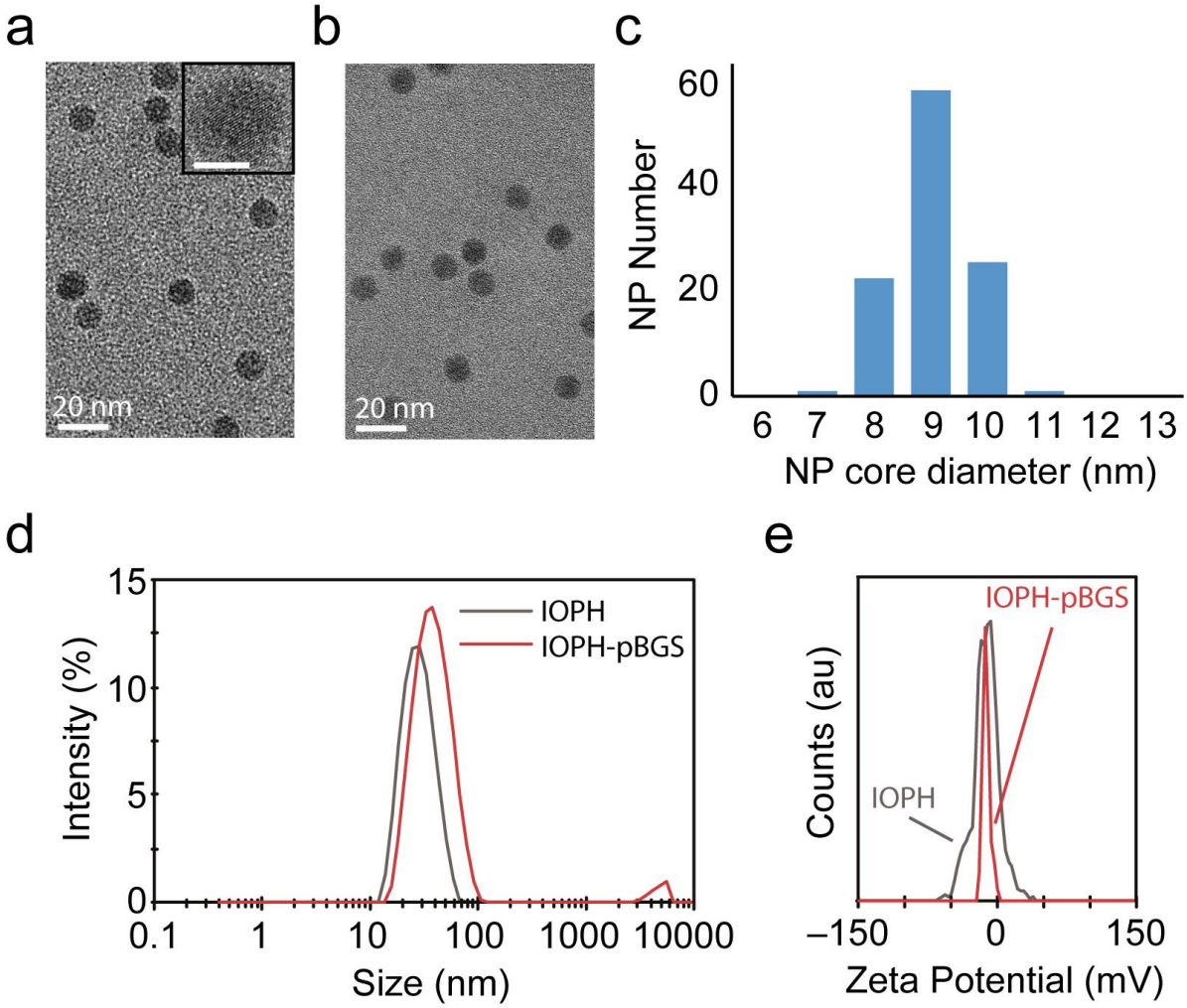

Figure 5-3. Primary physiochemical characterization of IOPH and IOPH-pBGS. TEM analysis of a) IOPH and b) IOPH-pBGS. The inset in a) shows the lattice fringe of the iron oxide SPION (Scale bar = 5 nm). c) Distribution of IOPH core diameter yielding a mean of 9 ± 0.7 nm determined from 100 independent core measurements using Image J software. d) Intensity based hydrodynamic size distribution of IOPH and IOPH-pBGS in PBS, pH 7.4. f) Zeta potential distribution of IOPH and IOPH-pBGS in HEPES buffer, pH 7.4.

SPION surface modification was qualitatively analyzed by Fourier transform infrared spectroscopy (FTIR) (**Figure 4-4**). IR spectra of IOPH and IOPH-pBGS show characteristic bands of different vibrational modes of PEG's C-O-C bonds at 1456, 1350, 1250, 1103, and 950 cm^{-1}.[147] In addition, The IR spectra for IOPH-pBGS has additional bands at 1579, 1558, 1543,

797 cm^{-1} indicative of aromatic structures confirming the presence of BGS. Band designation for additional functional groups of IOPH and IOPH-pBGS can be found in **Table 5-1**.

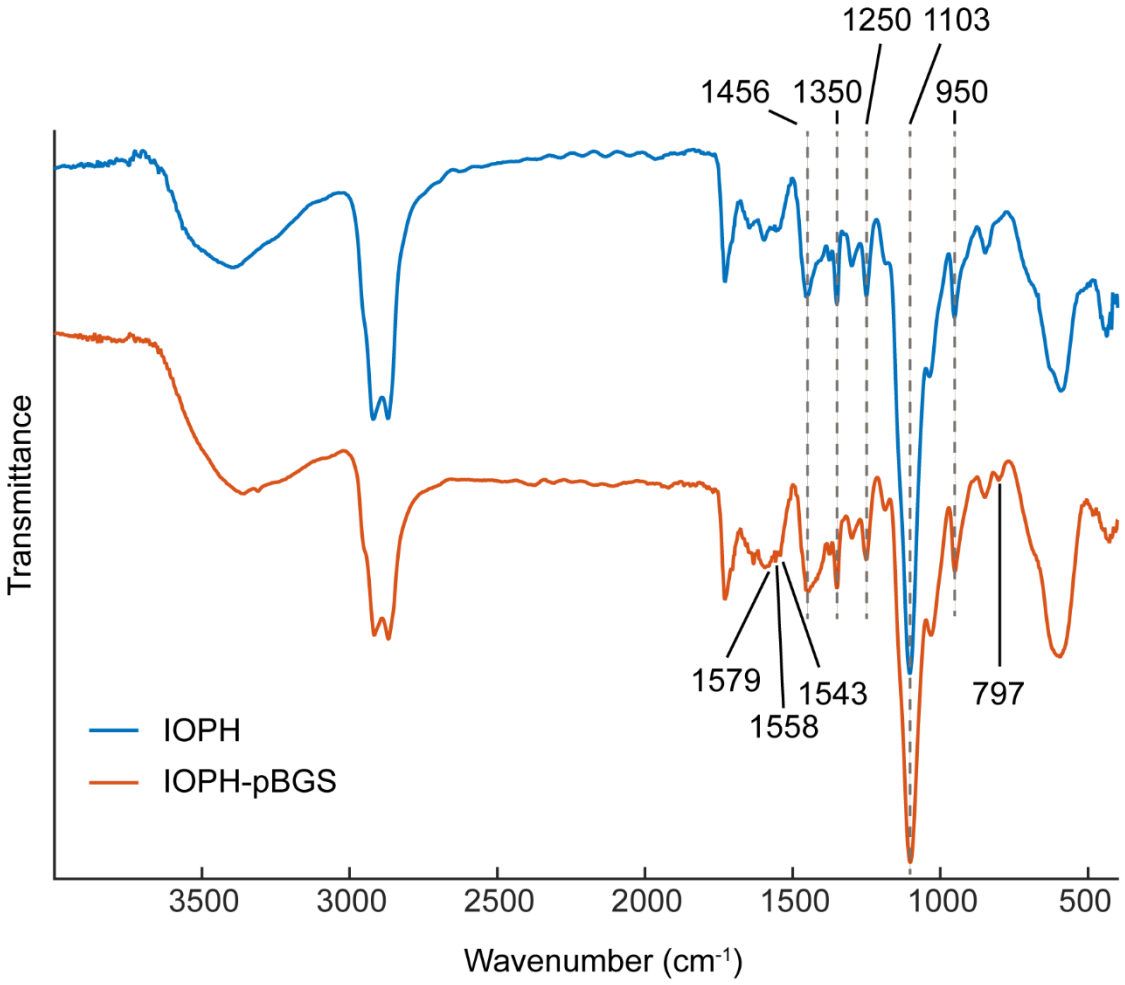

Figure 5-4. FTIR spectra of IOPH and IOPH-pBGS indicating the presence of aromatic structures associated with BGS.

Table 5-1. FTIR band designation of functional groups for IOPH and IOPH-pBGS.

Wavenumber (cm^{-1})	Functional Group (IOPH)	Functional Group (IOPH-BGS)
3365	Hydroxyl	Hydroxyl
2920	Alkane	Alkane
2870	Alkane	Alkane
1730	Ketone	Ketone
1647	Amide	-----
1633	-----	Amide
1597	Amine N-H bend	Amine N-H Bend
1579	-----	Aromatics
1558	-----	Aromatics
1541	-----	Aromatics
1456	Alkanes	Alkanes
1379	Alkane C-H rock	Alkane C-H rock
1350	Amine C-N Stretch	Amine C-N Stretch
1300	Ether	Ether
1250	Ether	Ether
1188	Amines	Amines
1103	Ether	Ether
1038	Si-OH stretch	Si-OH stretch
950	Ether	Ether
847	Amine wag	Amine Wag
797	-----	Aromatic out-of-plane bending

Direct quantitation of drug loading is difficult for iron oxide SPIONs because they absorb over a broad range of UV-vis wavelengths, while their magnetic properties cause NMR peak broadening and inconsistencies in peak ratios due to anisotropic effects.[148] We utilized the mono-hydrazide PAH in excess to drive the degradation of pBGS from the SPION surface for quantitation without interference from the iron oxide core. 50 μg of IOPH-pBGS were freeze dried and dissolved in 125 μL of a 10mg/mL PAH solution and sonicated for 2 h. SPIONs were removed from the supernatant using a centrifugal filter and quantitative drug loading was determined by UV-vis spectroscopy using a standard addition method. Percent drug loading by weight was determined to be 38.3 ± 2.9% which is high in comparison to typical solid core

nanoformulations that often only achieve 10% drug loading by weight.[149] **Table 5-2** summarizes the key physiochemical properties of IOPH-pBGS.

Table 5-2. Primary physiochemical properties of IOPH-pBGS.

Core Size (nm)	Hydrodynamic Size (nm)	PDI	Zeta Potential (mV)	% Drug loading by weight
9 ± 0.7	36.5 ± 1.8	0.196	-11.8 ± 4.02	38.3 ± 2.9

5.3.2 pH dependent drug release

Hydrazone linkages were chosen for polymerization of BGS due to their acid sensitive degradation profile that facilitate release of drug intracellularly while minimizing release in the blood.[150] The *in vitro* BGS release from IOPH-pBGS was evaluated under simulated physiological conditions (PBS, pH 7.4) and in conditions mimicking acidity of endosomes/lysosomes (MES buffer, pH 5.5) (**Figure 4-5**). It was found that BGS release from IOPH-pBGS was greatly affected by pH of the release media. BGS release at pH 5.5 shows a well controlled release profile approaching maximum release at 96 h with minimal signs of a burst effect. BGS release was suppressed with only ~20% of drug released after 96 h for SPIONs evaluated in PBS at pH 7.4. The differences in drug release at neutral and acidic conditions can be attributed to the effect of pH on the equilibrium of hydrazone bond formation.[151] The high drug loading and well controlled release of BGS from IOPH-pBGS under acidic conditions demonstrates the potential of IOPH-pBGS as an improved MGMT inhibitor delivery platform.

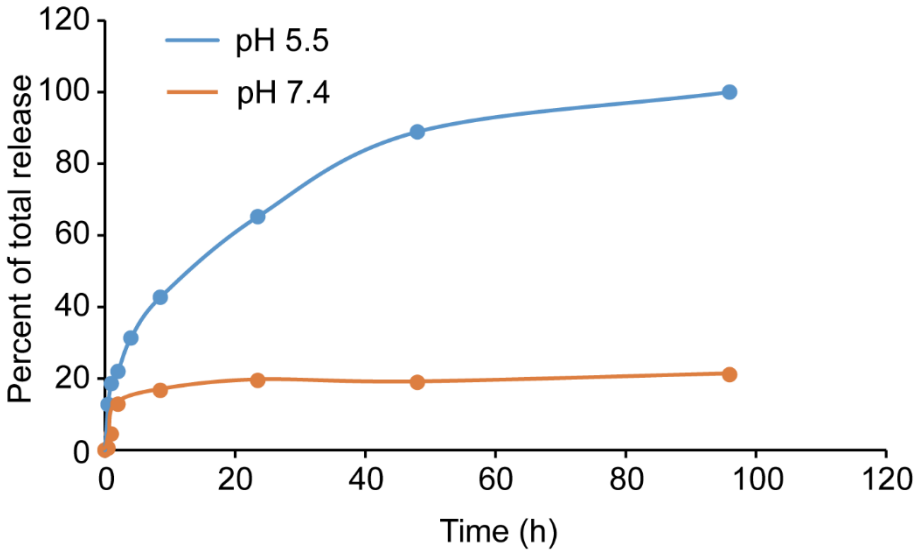

Figure 5-5. pH dependent release of BGS from IOPH-pBGS. Drug release was evaluated at physiological conditions (pH 7.4) and endosomal/lysosomal conditions (pH 5.5).

5.3.3 IOPH-pBGS inhibition of MGMT

Repair of cytotoxic DNA damage by repair protein MGMT has been shown to be a major component in the development of resistance of GBMs to chemotherapeutic alkylating agents such as TMZ.[142] It has also been shown that MGMT levels in healthy brain are relatively low and that high levels of the repair protein in tumors is associated with tumorgenisis.[117] Therefore, the ablation of MGMT activity in combination with TMZ is a promising treatment strategy for GBMs. Although BGS is simply ribose modified BG, there is no report of its use as an MGMT inhibitor in literature. Furthermore, upon degradation of pBGS, DA-BGS is the analog that presents itself intracellularly and must serve as a potent MGMT inhibitor. To confirm if BGS and DA-BGS function as MGMT inhibitors, a quantitative MGMT inhibition assay was performed using the MGMT+ human GBM cell line SF767. **Figure 4-6a** shows the effects of BG, BGS, and DA-BGS on MGMT activity of SF767 cells. Activity was determined at 2 and 24 h in

untreated cells and cells treated with 10 μM of inhibitor. Untreated cells had an activity of 25 fmol/10^6 cells or ~15,000 MGMT molecules/cell. All treatment conditions were normalized as the percent activity of untreated cells. At 2 h, cells exposed to BG showed a ~3.9-fold (~26% of untreated activity) reduction in MGMT, while those exposed to BGS and DA-BGS had a ~2.5-fold (~40 of untreated activity) and ~1.5-fold (~65% of untreated activity) reduction in MGMT levels. At 24 h, cells exposed to BG showed a ~10.6-fold (~9.4% of untreated activity) reduction in MGMT, while those exposed to BGS and DA-BGS had a ~17.1-fold (~5.9% of untreated activity) and ~11.2-fold (~13.4% of untreated activity) reduction in MGMT levels. The difference in MGMT suppression at 2 h between BG, BGS, and DA-BGS is likely explained by the increased hydrophilicity of BGS and DA-BGS. BG is capable of efficiently partitioning into lipid bilayers which facilitates rapid uptake *in vitro* but leads to poor pharmacokinetic profiles *in vivo*. Importantly, BGS and DA-BGS, in comparison to BG, demonstrated similar reduction in MGMT levels at 24 h indicating their utility as MGMT inhibitors.

Inhibition of MGMT by IOPH-pBGS was evaluated at 24 h utilizing the similar treatment conditions to those described above (**Figure 4-6b**). IOPH and BG were used as negative and positive controls respectively and 0.1and 10 μM BGS concentrations were evaluated for the SPION conditions. At 10 μM BGS concentration, IOPH-pBGS showed a reduction of ~6.7-fold (~14.4% activity of untreated) while the IOPH control particle at the same iron concentration had ~1.5-fold (~63.8% activity of untreated). Interestingly, at a 100-fold reduction in drug concentration (0.1 μM), IOPH-pBGS maintained a ~2.2-fold (~45.7% activity of untreated) reduction in MGMT activity. These results confirm that BGS and DA-BGS serve as inhibitors of MGMT and that DA-BGS maintains its inhibitor activity when formulated as IOPH-pBGS demonstrating the potential clinical relevance of the IOPH-pBGS formulation.

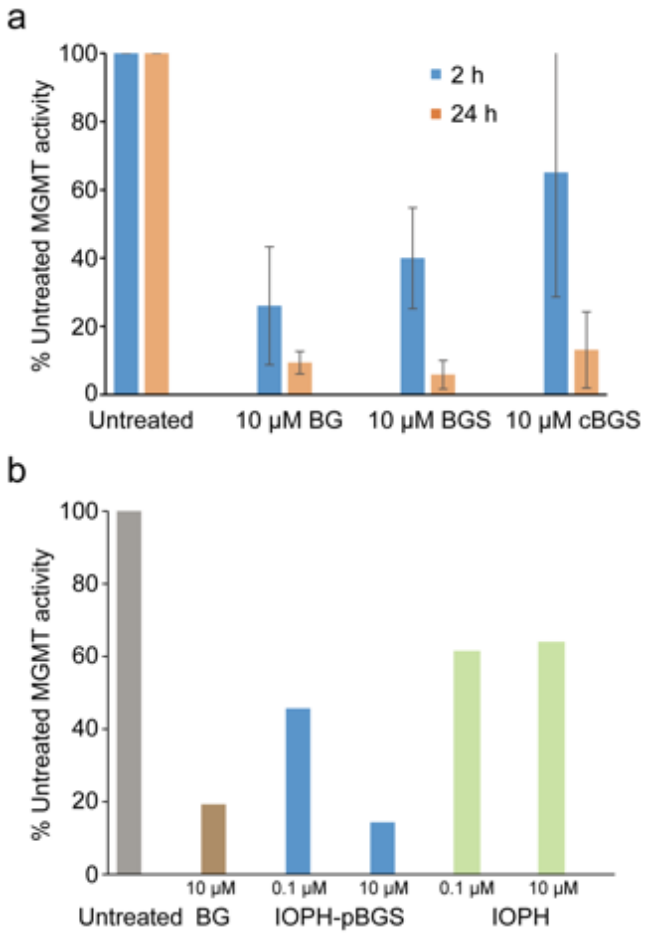

Figure 5-6. DA-BGS and IOPH-pBGS inhibit MGMT activity. a) Suppression of MGMT activity in SF767 cells treated with BG, BGS or DA-BGS. Cells were harvested 2 h and 24 h after inhibitor b) Supression of MGMT activity in SF767 cells treated with BG (10 μM) , IOPH and IOPH-pBGS (0.1μM and 10 μM) for 24 h.

5.4 Conclusions

Iron oxide SPIONs carrying a BGS payload for treatment of GBMs were successfully prepared. BGS and DA-BGS were evaluated *in vitro* as MGMT inhibitors and were shown to be as potent as BG after 24 h exposure. DA-BGS was successfully polymerized on the base SPION surface to produce IOPH-pBGS which exhibited proper size and surface charge for *in vivo*

application. FTIR analysis of IOPH-pBGS confirmed DA-BGS loading by appearances of bands associated with the aromatic structures of BGS. IOPH-pBGS achieved high drug loading and released drug through a pH dependent mechanism that favors release of drug intracellularly. Importantly, *in vitro* MGMT activity assays confirmed successful suppression of MGMT activity by IOPH-pBGS on par with free BG. The combination of high drug loading, controlled release and ability to efficiently suppress MGMT demonstrates the potential of IOPH-pBGS to serve as an improved MGMT inhibitor formulation that can provide minimally invasive i.v. administration and improved patient prognosis.

6 Streamlined Surface Functionalization of Theranostic SPIONs

Surface functionalization of theranostic nanoparticles (NPs) typically relies on lengthy, aqueous post-synthesis labeling chemistries that have limited ability to fine tune surface properties and can lead to NP heterogeneity. The need for a rapid, simple synthesis approach that can provide great control over the display of functional moieties on NP surfaces has lead to increased use of highly selective bioorthoganol chemistries including metal-affinity coordination. Here we report a simple approach for rapid production of a superparamagnetic iron oxide NPs (SPIONs) with tunable functionality and high reproducibility under aqueous conditions. We utilize the high affinity complex formed between catechol and $Fe^{(III)}$ as a means to dock well-defined catechol modified polymer modules on the surface of SPIONs during co-precipitation synthesis. Polymer modules consisted of chitosan and poly(ethylene glycol) (PEG) copolymer (CP) modified with catechol (CCP), and CCP functionalized with cationic polyethylenimine (CCP-PEI) to facilitate binding and delivery of DNA for gene therapy. This rapid synthesis/functionalization approach provided excellent control over the extent of PEI labeling, improved SPION magnetic properties and produced an efficient transfection agent.

6.1 Introduction

Theranostic NPs capable of diagnostic imaging and therapeutic drug delivery have potential to revolutionize current clinical approaches to cancer therapy.[103b, 103c, 152] Of the nanomaterials studied to this end, iron oxide nanoparticles have emerged as one of top candidates. Their intrinsic superparamagnetism enables non-invasive magnetic resonance imaging (MRI), and their biodegradability is advantageous for *in vivo* applications. [153 154] The

successful translation of theranostic NPs to clinic will require the development of simplified production processes that lead to reproducible NPs with control over surface functionality while maintaining excellent imaging sensitivity. However, theranostic NPs are inherently complex, typically containing endogenous and/or exogenous imaging components, therapeutic agent(s), and targeting ligands with each component typically added through time consuming multi-step processes (i.e., each step involving processes such as surface modification, purification, and characterization). Unlike polymer conjugates, theranostic SPION conjugates are generally difficult to characterize because their nanosized feature and magnetic properties cause fluorescence quenching and NMR peak broadening and inconsistencies in peak ratios.[148] More importantly, post synthesis surface modification of theranostic SPIONs (and other NPs as well) relies primarily on aqueous chemistries that are prone to hydrolysis and unwanted crosslinking, and often lacks reaction site specificity,[155] yielding limited ability to fine tune surface functionality and maintain batch-to-batch consistency. Furthermore, surface coatings produced by existing methods would more or less reduce the intrinsic magnetism of SPIONs.

The complex formed between catechol and $Fe^{(III)}$ is extremely stable due to the σ- and π-donor bond contributions[156] and researchers have previously exploited the $Fe^{(III)}$-catechol interaction to yield ultra-stable catechol-polymer capped SPIONs with improved magnetic properties.[157] However, to date, all catechol-polymer capped SPIONs have been produced through laborious ligand exchange processes subsequent to SPION synthesis, typically by the thermal decomposition method. The thermal decomposition synthesis of SPIONs requires one day to produce an Fe-oleate complex followed by a second day to thermally decompose the Fe-oleate complex and purify the product to produce water-insoluble oleic acid coated SPIONs that must then undergo ligand exchange process to infer water solubility. In addition, biomedical

application of SPIONs normally requires additional chemistry to enable appropriate surface functionality, which requires additional processing time (days). Our approach directly produces water-soluble, catechol capped SPIONs with appropriate surface functionality for gene delivery in less than 24 h including ~2 h of active time and an overnight aging step. Furthermore, our simplified approach significantly reduces the batch-to-batch variation, which is normally proportional to the chemical reaction steps involved.

Here we report a simple method for production of a SPION gene transfection agent utilizing polymer modules consisting of chitosan and poly(ethylene glycol) (PEG) copolymer (CP) modified with catechol (CCP), and polyethylenimine (PEI) modified CCP (CCP-PEI) that exhibit high affinity and specificity for iron oxide surfaces. Utilization of an aqueous co-precipitation synthesis method[158] modified by reducing polymer concentration during initial synthesis and addition of functionalized polymer post-synthesis, facilitated a rapid synthesis/coating/functionalization of theranostic SPIONs. The high affinity of the catechol functionalized polymer for the iron oxide core provided the ability to fine-tune important physiochemical properties by altering feed ratios of the polymer modules which improved reproducibility through strong site-specific interaction between the iron oxide core and catechol-functionalized polymer coating and enhanced the magnetic properties by increasing the spin ordering of SPIONs. As a model system, PEI was chosen as a CCP modifier to infer functionality through its cationic charge capable of efficiently binding DNA for gene therapy applications. However, we anticipate this approach to be widely applicable to other therapeutic platforms by simply replacing PEI modified CCP with a suite of chemo/biotherapeutic and targeting ligand modified CCP to allow a highly customizable approach to patient care.

6.2 Experimental

6.2.1 Materials

All reagents were purchased from Sigma-Aldrich (St. Louis, MO) unless otherwise specified. The low molecular weight chitosan was purchased from Acemey Industrial (Shanghai, China). The heterobifunctional linker 2-iminothiolane (Traut's reagent) and succinimidyl iodoacetate (SIA) was purchased from Molecular Biosciences (Boulder, CO). NHS-PEG_{12}-maleimide was purchased from Thermo Fisher Scientific (Rockford, IL). Tissue culture reagents including DMEM and antibiotic-antimycotic were purchased from Invitrogen (Carlsbad, CA). Fetal bovine serum (FBS) was purchased from Atlanta Biologicals (Lawrenceville, GA).

6.2.2 Polymer synthesis

2,300 MW chitosan oligosaccharide (1.3 mmol) was dissolved in 40 mL DI water and 8 mL methanol was added drop-wise and the solution was pH was adjusted to 6.5. Aldehyde-activated methoxy PEG (13 mmol) produced by the Pfitzner-Moffatt oxidation of 2000 MW methoxy-PEG-OH, and 3,4-dihydroxybenzaldehyde (5.2 mmol, DHBA) dissolved in 16 mL DI water were then added drop-wise and reacted for 1 h. 1.0 M sodium cyanoborohydride (185 µL, diluted to 12 mL in DI water) was added drop-wise and the solution was reacted for an additional 18 h. The resulting catechol functionalized chitosan-PEG (CCP) was precipitated with acetone, collected with a Buchner funnel, washed three times with acetone to remove unreacted PEG, dried by vacuum, re-dispersed in DI water and further purified by tangential flow filtration (TFF, Millipore, Billerica, MA) using a 5 k MW cutoff cassette. The purified polymers were freeze-dried and stored at −20 °C.

CCP was further modified with PEI (CCP-PEI) as follows: CCP (500mg) was dissolved at 100 mg·mL^{-1} in 0.1 M Na bicarbonate, 5 mM EDTA buffer at pH 8.0 and reacted with SIA (142 mg) dissolved in 1 mL dimethyl sulfoxide (DMSO) and reacted for 1 h at room temperature with gentle rocking. Simultaneously, 6.25 g of 25 k MW PEI was dissolved in 20 mL 0.1 M Na bicarbonate, 5 mM EDTA bufferr at pH 8.0, and Traut's reagent (40 mg at 10 mg·mL^{-1} in 0.1 M Na bicarbonate, 5 mM EDTA bufferr at pH 8.0) was added and reacted for 1 h at room temperature. SIA modified chitosan and Traut's reagent modified PEI were added together and reacted for 30 m. The CCP-PEI reaction mixture was purified by dialysis against DI water using 50 kDa MWCO Spectra/Por dialysis membrane (Spectrum Laboratories, Rancho Dominguez, CA). The purified polymers were freeze-dried and stored at −20 °C.

CCP-Cy5 was synthesized as follows: 2.5 mg of Cy5-NHS ester (Lumiprobe, Hallandale, FL) was dissolved in 100 µL of anhhdrous DMSO and added to 35mg of CPP dissolved in 2 mL of anhydrous DMSO. 0.1% N,N-diisopropylethylamine was added as a base catalyst. The mixture was reacted for 48 h at room temperature and purified by dialysis against DI water using 8 kDa MWCO Spectra/Por dialysis membrane (Spectrum Laboratories, Rancho Dominguez, CA). Purified CCP was freeze-dried and stored at −20 °C.

6.2.3 NMR analysis

Polymer samples were prepared by dissolving polymer and TSP in D_2O and NMR spectra were obtained using a Bruker Avance 300 spectrometer operating at 300 MHz (^{1}H) and 298 K (number of scans = 64, acquisition time = 3.9 s, delay (D1) = 2 s).

Peak identification:

CP (PEG): ^{1}H NMR (300.13 MHz, D_2O) δ 3.38 (3H, s)

CCP (catechol group): ^{1}H NMR (300.13 MHz, D_2O) δ 7.1-6.75 (3H, m), 3.38 (3H, s)

CCP-PEI (PEI): ^{1}H NMR (300.13 MHz, D_2O) δ 2.9-2.5

6.2.4 IOCCP and IOCCP-PEI synthesis

Iron oxide nanoparticles coated with CCP or CCP/CCP-PEI were synthesized via a co-precipitation of iron chlorides in aqueous solution. Briefly, pure CCP (25 mg) was mixed with iron chlorides (9 mg Fe^{2+}, 18 mg Fe^{3+}) in 2.18 mL of degassed DI water. A 14.5 M solution of ammonium hydroxide was titrated in slowly at 40 ºC with sonication until a final pH of 10.5 was reached to ensure nucleation of SPIONs. Upon completion of base titration, sonication was continued until a pH of 8.5-9.5 was reached due to evaporation of ammonia from the solution. 50mg of additional polymer (CCP, or CCP/CCP-PEI) was then added and the SPIONs were incubated overnight at 4 °C. The synthesized IOCCPs/IOCCP-PEI were purified first by centrifugation at 3500 rcf for 10 minutes and the supernatant was further purified using size exclusion chromatography in S-200 resin (GE Healthcare, Piscataway, NJ) into 20 mM HEPES buffer, pH 7.4. IOCCP-Cy5 was synthesized in the same manner with CCP-Cy5 replacing CCP-PEI.

6.2.5 Hydrodynamic size and ζ potential characterization

Hydrodynamic size and ζ potential of IOCCP, IOCCP-PEI, and IOCCP-PEI complexed with DNA as described below was analyzed at 100 μg mL−1 in 20 mM HEPES buffer (pH 7.4) using a DTS Zetasizer Nano (Malvern Instruments, Worcestershire, UK).

6.2.6 TGA analysis

SPIONs were purified in to DI H_2O, freeze-dried, and ground into powder using a mortar and pestle. 3.5 ± 0.2 mg of SPION powder was placed in a platinum crucible and analyzed with a TGA Q50 system (TA Instruments, New Castle, DE) by ramping temperature at 20 °C/minute with a starting temperature of 25 °C and a final Temperature of 500 °C.

6.2.7 TEM analysis of SPION core diameter

TEM images were acquired with an FEI TECNAI F20 TEM (Hillsboro, OR) operating at 200 kV. SPION core diameters were analyzed with ImageJ software, and the size distribution, mean diameter, and standard deviation was calculated from 200 SPION measurements.

6.2.8 AFM analysis

IOCCP and IOCCP-PEI AFM samples were prepared by dropping and air-drying ~5 μg/mL of SPION solution in water on freshly cleaved mica. SPIONs images were acquired with a Dimension-3100 (Veeco/DI/Bruker, Madison, WI) in tapping mode in air with an antimony-doped silicon cantilever (FESP, Bruker, Madison, WI). The cantilever had a nominal spring constant of 2.8 N/m, a resonant frequency of 75 kHz, a length of 225 μm, and a tip radius of 8 nm. Images were processed using Gwyddion software.

6.2.9 Magnetic characterization of IOCCP and IOCCP-PEI

R_2 relaxivity ($1/T_2$) of SPIONs at concentrations of 0, 5, 10, 15, 20, and 25 μg Fe mL^{-1} in phosphate buffered saline was evaluated by MRI using a Bruker (Billerica, MA) 14 Tesla

vertical-bore imaging system (Utlrashield 600 WB Plus) through multi-spin echo acquisitions. Glass vials (3.25 mm I.D., 5 mm O.D., 200 μL volume) were filled with 150 μL of SPION/PBS solution. The vials were secured and surrounded by water to serve as a homogeneous background signal to minimize magnetic susceptibility variations around the samples. The fixed samples were positioned in a 25 mm single-channel ^{1}H radiofrequency receive coil (PB Micro 2.5). The samples were scanned with a quantitative T2 multi-spin multi echo scan sequence (MSME) (TR = 2500 ms, TE = 6.7 + 6n ms, [n=0-16], in-plane resolution 78x156 μm^2, matrix 256x128) with 0.5 mm slice thickness for 14 slices. Analysis of MRI data was accomplished with the FMRIB software library (FSL), Paravision 5.1 analysis package (Bruker), Osirix (Pixmeo), and ImageJ (NIH). T2 values were determined within a circular, 100-voxel region of interest.

6.2.10 Plasmid DNA preparation

The plasmid pDsRed-Max-N1 (pRFP) vector was purchased from Addgene (Cambridge, MA) and contained RFP encoding DNA under control of the cytomegalovirus (CMV) promoter, and was propagated in DH5α *E. Coli* and purified using a Plasmid Giga Kit (Qiagen, Valencia, CA).

6.2.11 SPION/DNA complex formation

For DNA ratio optimization based on hydrodynamic size and zeta potential, DNA was prepared at appropriate concentrations in 20mM HEPES buffer pH 7.4 and incubated for 5 minutes at room temperature to produce SPION/DNA ratio of 2, 5, 10 and 20:1 SPION to pRFP

with SPIONs added at a final concentration of 100 μg Fe mL^{-1}. After addition of SPION, the solution was mixed by micropipette and incubated for 15 minutes at room temperature before measurements were taken. For *in vitro* cell transfections, SPION /DNA complexes at 1 μg DNA/50 μL were formed by first incubating pRFP in 20mM HEPES buffer pH 7.4 for 5 minutes at room temperature. SPIONs were then added at appropriate volume to yield a 10:1 w/w ratio with pRFP, mixed thoroughly by micropipette and incubated for 15 minutes at room temperature.

6.2.12 PEGylation of IOCCP-PEI complexed with DNA

IOCCP-PEI complexed with DNA at a 10:1 w/w ratio of SPION to DNA was reacted with $SM(PEG)_{12}$ at 216 μg of $SM(PEG)_{12}$ per mg Fe in the dark with gentle rocking for 30 min. The $SM(PEG)_{12}$ modified IOCCP-PEI (IOCCP-PEI-PEG) was then purified using size exclusion chromatography in S-200 resin equilibrated with 20mM HEPEs, pH 7.4, and stored at 4 ºC.

6.2.13 Cell Culture

SF767 human glioblastoma multiforme (GBM) cells (American Type Culture Collection, Manassas, VA) were cultured in DMEM supplemented with 10% FBS and 1% antibiotic-antimycotic (Invitrogen, Carlsbad, CA). Cultures were maintained at 37°C in a humidified incubator with 5% CO_2.

6.2.14 Cell viability assay

A cell viability assay using alamarBlue reagent (Invitrogen, Carlsbad, CA) was performed on Human GBM cell line SF767. Briefly, 96-well plates were inoculated with 5,000 cells per 100 μL of supplemented media and incubated overnight at 37ºC in 95%/5% air/CO_2. Before treatment each well was increased in volume to 200 μL. Cells received treatments of SPION/DNA complex (10:1 w/w), PEI/DNA (10:1 w/w) or Lipofectamine 2000/DNA (3:1, w/w) prepared according to the manufacturer's instructions, and diluted to achieve 0.1, 0.5, 1, 2, 3, or 4 μg mL^{-1} DNA final concentration. Cells were incubated for 48 h with the transfection agents. Alamar blue reagent was added and incubated for 2 h according to manufacturer's instructions. Viability was quantified by fluorescence spectrophotometery using a fluorescence excitation wavelength of 550ex/590em on a SpectraMax i3 microplate reader (Molecular Devices, Sunnyvale, CA).

6.2.15 Confocal imaging

For each transfection condition, 50,000 SF767 cells were seeded onto 24 mm glass cover slips 12–16 h prior to transfection. Cells were transfected as described above, then 48 h after transfection, were washed thrice with PBS and fixed with 4% formaldehyde (methanol free, Polysciences Inc., Warrington, PA) in PBS for 30 minutes at room temperature. Fixative was then removed and cells were washed thrice with PBS to remove the formaldehyde. Cells were membrane-stained with WGA-AF647 (Invitrogen, Carlsbad, CA) according to the manufacturer's instructions. The slides were mounted using ProLong Gold antifade solution containing DAPI (Invitrogen, Carlsbad, CA) and imaged using a Nikon Eclipse TE2000s confocal fluorescence microscope (Nikon, Tokyo, Japan).

6.2.16 Cell transfections and flow cytometry analysis

Human GBM cell line SF767 was used to compare the transfection efficiency of the SPION formulations against a Lipofectamine 2000 standard (Invitrogen, Carlsbad, CA) and 25 K PEI using pRFP. Briefly, cells were seeded at 100,000 cells/well in 24-well plates 16 h prior to transfection. SPION/DNA complexes prepared at different ratios (w/w) as described above were added to 1 ml of fully supplemented culture media to give a final DNA concentration of 1 or 2 μg DNA mL^{-1} in each well and gently rocked to mix. Cells were incubated with complexes for 48 h. Transfections using the commercial agent, Lipofectamine 2000, were performed following the manufacturer's protocol. Visual confirmation of RFP transfection was obtained by confocal microscopy using 561 nm excitation. Quantitative transfection efficiency was collected by flow cytometry.

Cells were washed three times with PBS, and detached using TrypLE Express (Invitrogen, Carlsbad, CA), and suspended in PBS containing 2% FBS. 5,000 cells were then analyzed using a BD FACSCanto flow cytometer (Beckton Dickinson, Franklin Lakes, NJ) and data analyses were performed using the FlowJo software package (Tree Star, Ashland, OR).

6.2.17 Statistical analysis

Experiments were performed in triplicate and the data was statistically analyzed to express the mean ± standard deviation (SD) unless otherwise stated.

6.3 Results and Discussion

6.3.1 Synthesis and characterization of CCP and CCP-PEI

The multi-dentate catechol polymers were synthesized by modification of low molecular weight chitosan (2300 MW) with aldehyde functionalized methoxy-PEG (mPEG-aldehyde, 2000 MW) and catechol analog 3,4-dihydroxybenzaldehyde (DHBA) through reductive amination (**Figure 5-1a**). PEI modified CCP (CCP-PEI, **Figure 5-1b**) was produced by coupling thiolated 25k MW PEI with iodoacetyl modified CCP. The presence of catechol, PEG, and PEI on the chitosan backbone of CP (control), CCP and CCP-PEI were verified by ^{1}H-NMR (**Figure 5-1c**). Analysis of CCP showed the characteristic ^{1}H-NMR peak for the methoxy group of PEG present at $\delta = 3.38$ and the peaks corresponding to the catechol aromatic hydrogens were present at $\delta =$ 6.91-7.55. The extent of grafting was determined to be ~3 PEG/chitosan and ~2 catechol/chitosan and CCP-PEI was 72% w/w PEI based on the characteristic ^{1}H-NMR peaks associated with ethylenimine ($-NH_2-CH_2-CH_2-$) in the CCP-PEI spectra. Adequate PEG grafting provides steric stabilization for SPIONs coated with CCP and moderates charge associated toxicity for PEI modified SPIONs.[159] The presence of multiple catechol groups on the chitosan backbone increases the affinity of polymer to the iron oxide core due to the multi-dentate effect.[160]

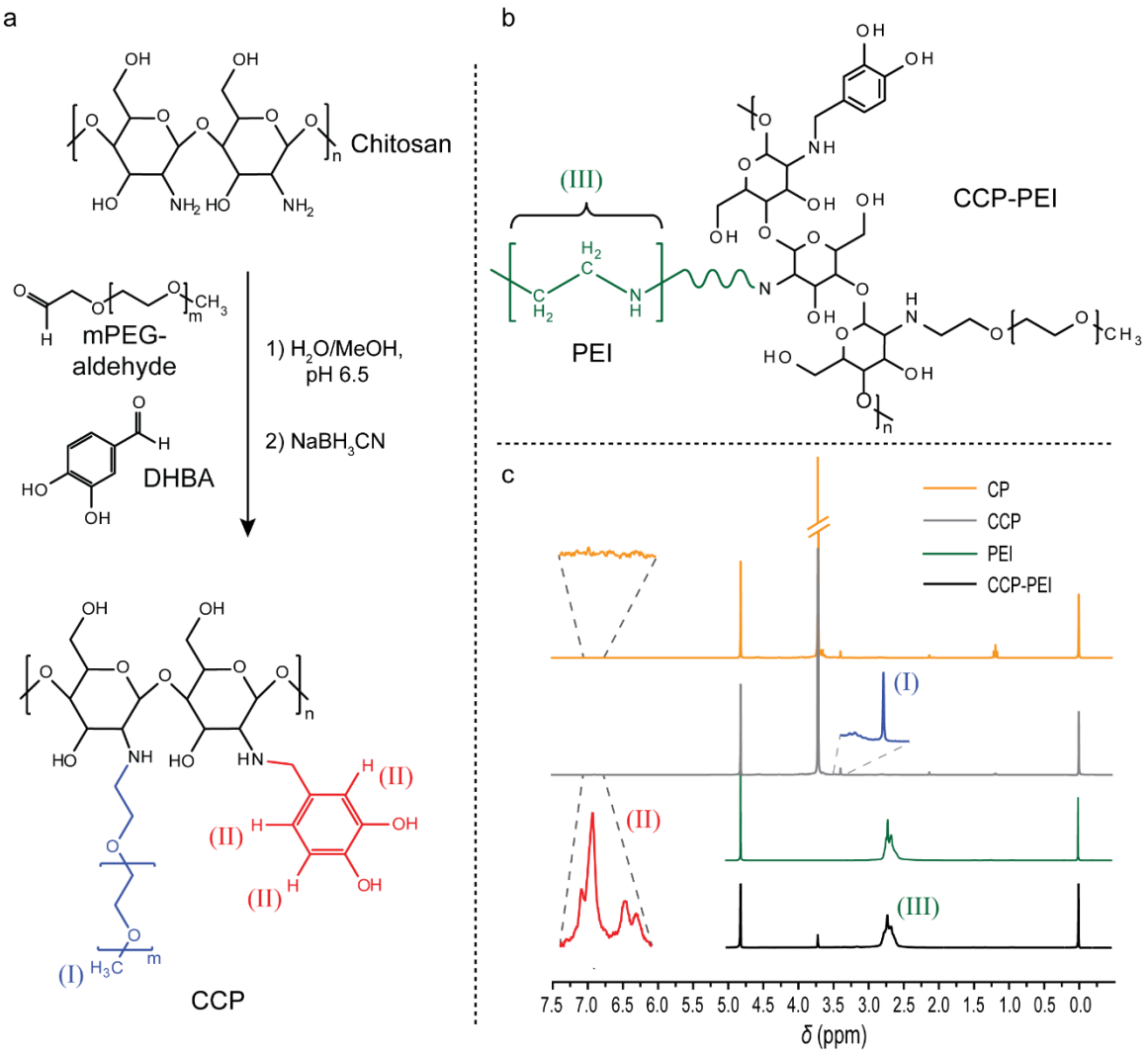

Figure 6-1. Synthesis and characterization of CCP and CCP-PEI. a) CCP synthesis via catechol and PEG modification of low molecular weight chitosan by reductive amination. b) Chemical structure of CCP-PEI and its characteristic ethylenimine group. c) Proton NMR analysis of CCP and CCP-PEI. The methoxy hydrogens of PEG (I) and the aromatic catechol hydrogens (II) were used to determine the extent of grafting on the chitosan backbone. Characteristic peaks associated with the ethylenimine group of PEI (III) confirm the presence of PEI on IOCCP-PEI. All samples were analyzed in D_2O in the presence of TSP.

6.3.2 Synthesis and characterization of IOCCP and IOCCP-PEI

SPION synthesis by co-precipitation of iron chlorides was carried out in the presence of low concentration CCP to produce a diffusely coated SPION (Intermediate IOCCP, **Figure 5-2a**). This initial step was followed by the addition of CCP to produce chitosan-PEG coated

SPIONs (IOCCP) or various ratios of CCP and CCP-PEI to produce PEI functionalized SPIONs (IOCCP-PEI) for gene delivery (**Figure 5-2b**). The cationic charge of PEI allows for efficient binding of DNA through electrostatic interaction with the negatively charged phosphate backbone (**Figure 5-2c**). An advantage of performing SPION synthesis in the presence of catechol-functionalized polymer is the avoidance of ligand exchange processes that can have deleterious effects on SPIONs magnetic properties due to incomplete ligand exchange.[161] The lack of competition for the SPION surface ensures unhindered catechol-iron interactions (**Figure 5-2d**).

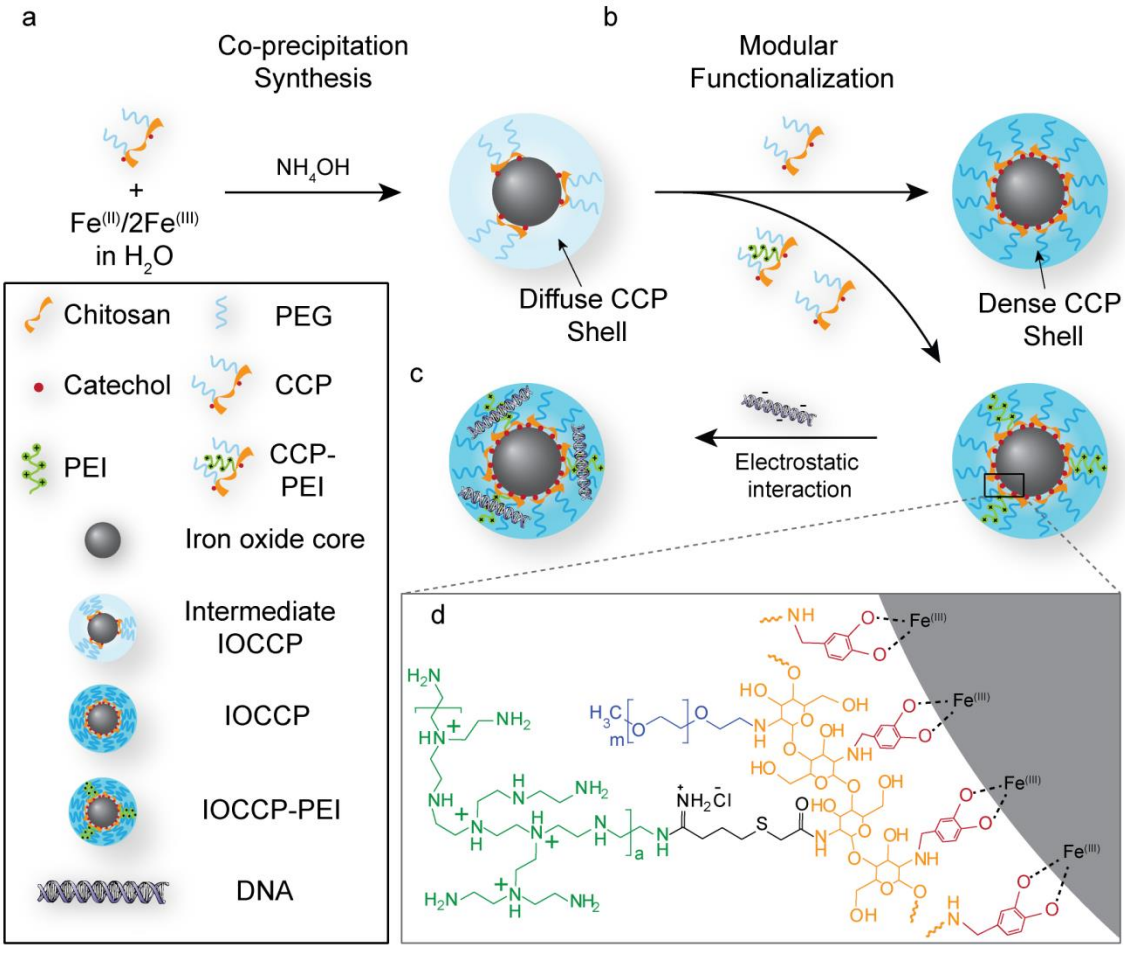

Figure 6-2. Synthesis and modular functionalization of IOCCP and IOCCP-PEI. a) Diffusely coated intermediate IOCCPs were initially synthesized in the presence of a low concentration of CCP then (b) supplemented with additional polymer (CCP or CCP-PEI) to add functionality to

the SPION and increase coating density. c) PEI functionalized SPIONs bind DNA through electrostatic interactions. d) Chemical detail of the SPION surface and catechol-polymer interface.

To determine the best ratio of CCP to CCP-PEI for gene delivery applications, ζ potential measurements of IOCCP-PEI produced at various polymer ratios were evaluated to optimize cationic surface charge to be between 15-20 mV based on our previous experience with similar SPIONs.[101] The surface charge of IOCCP-PEI was found to be highly tunable and repeatable from batch to batch with the modular addition of CCP-PEI (**Figure 5-3a**). IOCCP had a ζ potential of 5.8 ± 3 mV and increased to 21.2 ± 0.9 mV at 75% w/w feed ratio of CCP-PEI. Both the 25% CCP-PEI (17.3 ± 1.4 mV) and 50% CCP-PEI (19.9 ± 0.6 mV) ratio produced IOCCP-PEIs with ζ potentials in the 15-20 mV range, which warranted further screening of these two ratios *in vitro*. Pilot transfections studies indicated that the 50% w/w CCP-PEI ratio produced a far more efficient transfection agent than the 25% w/w CCP-PEI. For the remainder of this chapter, all references to IOCCP-PEI refer to those synthesized with 50% w/w CCP-PEI unless otherwise stated. A comparison of the ζ potential distributions of IOCCP and IOCCP-PEI at the 50% w/w ratio of CCP-PEI to CCP is shown in **Figure 5-3b**.

Hydrodynamic size is a primary factor in determining the *in vivo* fate of SPIONs, affecting uptake, retention and clearance.[59a, 146] IOCCP and IOCCP-PEI had an average hydrodynamic size of 35 ± 2 nm and 72 ± 3 nm, respectively, which falls well within the appropriate range for navigation and evasion of the mononuclear phagocyte system (**Figure 5-3c**).[59a] The increase in hydrodynamic size is likely due to the addition of relatively bulky PEI and increased organization of water along the polymer/water interface due to the high positive charge associated with PEI.

Thermal gravimetric analysis (TGA) was used to measure % weight loss to compare the polymer coating densities of the initial diffusely coated intermediate IOCCP, IOCCP, and IOCCP-PEI (**Figure 5-3d**). Since all SPIONs have a similar core diameter and iron oxide won't degrade at the evaluated temperatures, any differences in % weight loss are indicative of the density of the polymer surface coating. IOCCP showed a 20 % increase in % weight loss over intermediate IOCCP (black arrows). IOCCP-PEI had an additional 18 % increase in weight loss compared to IOCCP (dashed black arrows). The increase in polymer density for IOCCP-PEI is likely caused by the addition of highly branched PEI.

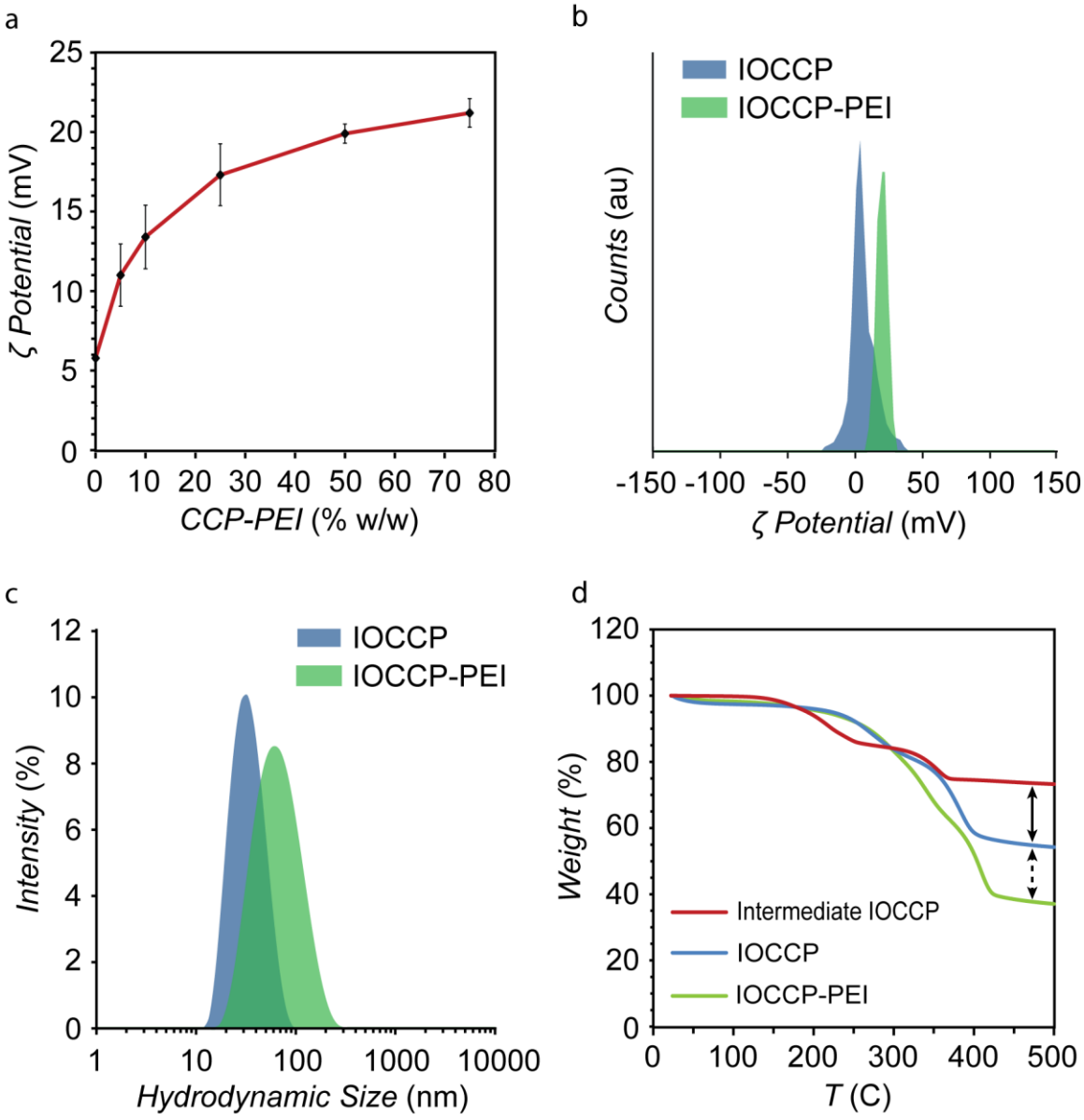

Figure 6-3. Characterization of size and surface properties of IOCCP and IOCCP-PEI. a) Evaluation of change in weight % CCP-PEI on ζ potential of IOCCP-PEI. The mean ζ potential for each ratio was determined from three separate batches of IOCCP-PEI. Error bars = standard deviation. b) ζ potential distributions of IOCCP (blue) and IOCCP-PEI (green) in 20mM HEPES, pH 7.4. c) Intensity based hydrodynamic size distributions of IOCCP (blue) and IOCCP-PEI (green) in 20mM HEPES, pH 7.4. d) TGA analysis showing increased polymer density for IOCCP and IOCCP-PEI (50% CCP-PEI w/w) as compared to intermediate IOCCPs.

Despite differences in hydrodynamic size, TEM analysis of IOCCP and IOCCP-PEI showed no marked difference in core morphology or size (**Figure 5-4a-d**). IOCCP and IOCCP-

PEI iron oxide cores had a roughly spherical shape and size distribution analysis revealed similar average core diameters of 5.2 ± 1.4 nm and 5.3 ± 1.7 nm for IOCCP and IOCCP-PEI, respectively. Similar size and morphology is expected since SPION core nucleation and growth phases were completed before additional CCP or CCP/CCP-PEI was added to increase the polymer surface density.

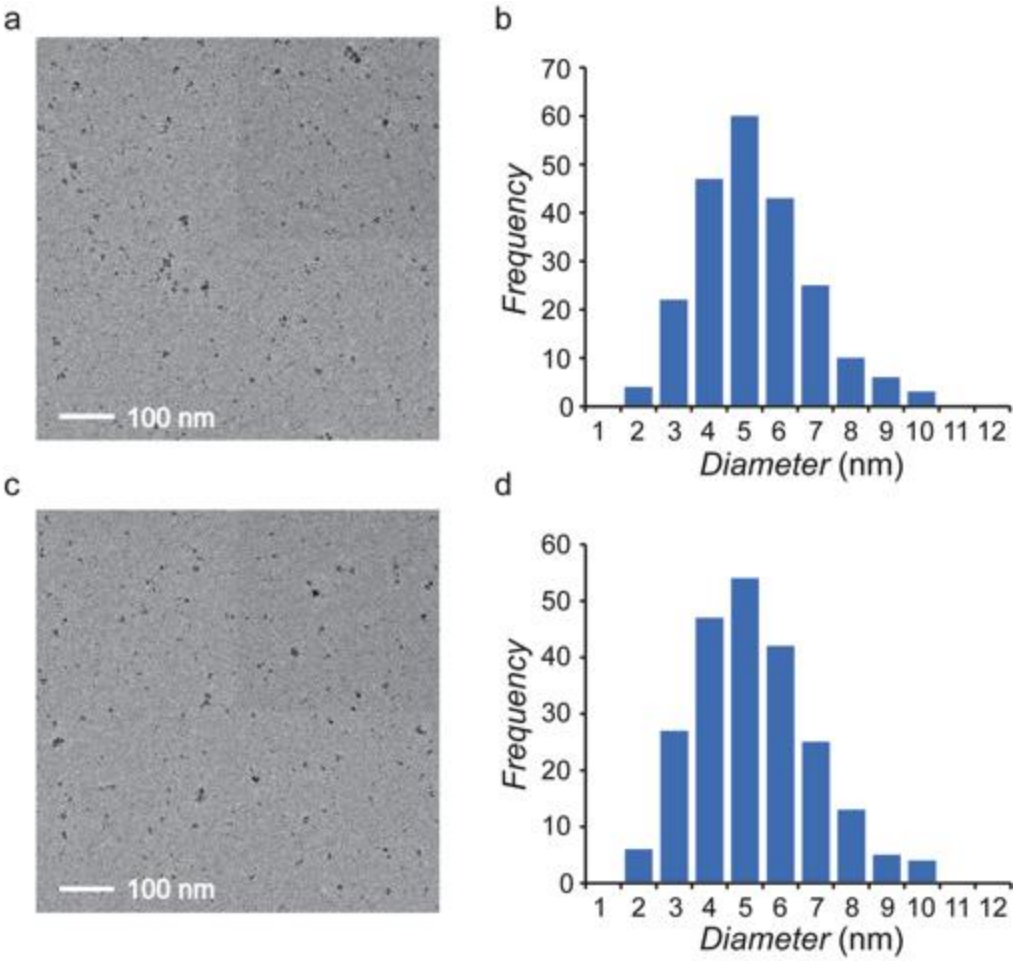

Figure 6-4. Determination of IOCCP and IOCCP-PEI core size. a) Representative TEM image of IOCCP. b) Distribution of IOCCP core diameter yielding a mean of 5.2 ± 1.4 nm. c) Representative TEM image of IOCCP-PEI. d) Distribution of IOCCP-PEI core diameter yielding a mean of 5.3 ± 1.7 nm. Histograms were produced from 200 independent core measurements using ImageJ software.

Atomic force microscopy (AFM) analysis provided size and morphology information of the non-hydrated polymer coated SPIONs (**Figure 5-5a-d**). IOCCP and IOCCP-PEI samples were prepared on a mica substrate and imaged in tapping mode. The spherical morphology is evident and the size in the x and y-planes is slightly smaller than the hydrodynamic size, which is expected given the lack of an associated water layer and subsequent drying effects. SPION height in the z-plane is less than that in the xy-plane most likely due to the collapse of the non-hydrated, highly flexible polymer coating and the affinity of the highly anionic mica substrate to the cationic polymer coatings.

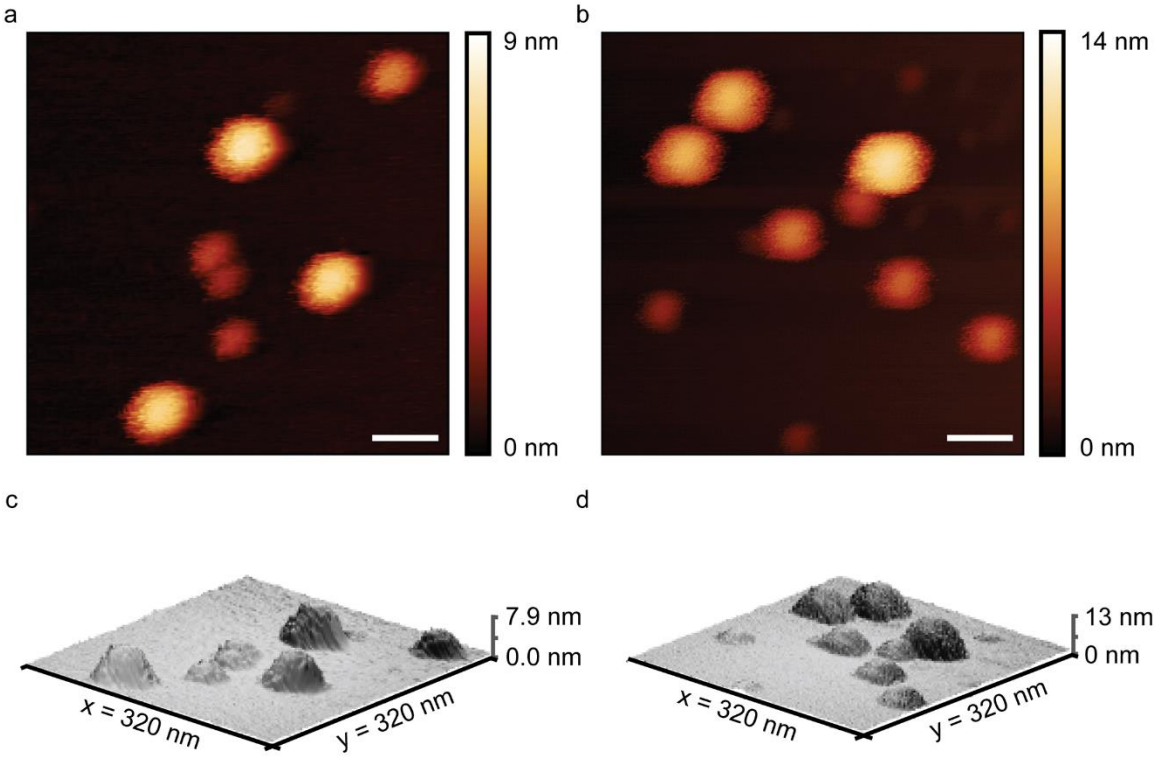

Figure 6-5. AFM images of IOCCP and IOCCP-PEI acquired in tapping mode. 2D color maps of (a) IOCCP and (b) IOCCP-PEI and corresponding 3D topography maps of (c) IOCCP and (d) IOCCP-PEI. Scale bar corresponds to 50 nm.

A major advantage to capping SPIONs with catechol-functionalized polymers is the improved magnetic properties,[162] which increases T_2 contrast enhancement in MR imaging.

SPIONs have a large proportion of under-coordinated atoms on the particle surface due to the large surface-area-to-volume ratio inherent to particles at this size. In addition, SPIONs have high curvature due to small particle radii resulting in canted spins and spin-glass-like behavior on the surface layer. These phenomena produce a magnetic dead surface layer[163] that reduce the magnetic diameter and the overall mass magnetization of SPIONs as compared to bulk magnetite, thereby reducing MR contrast enhancement. Catechol moieties, facilitated by their electron withdrawing structure, have shown to display spin-ordering behavior by satisfying under-coordinated $Fe^{(III)}$ atoms on SPION surfaces, rejuvenating the magnetic dead layer, producing a nonzero moment on the SPION surface, and drastically increasing magnetic susceptibility.[164] **Figure 5-6a** qualitatively illustrates the differences in spin alignment on catechol and non-catechol capped SPION surfaces and their effect on overall magnetic moments (μ).

A comparison of MR R_2 relaxivity ($1/T_2$) for IOCCP-PEI and IOCCP at field strength of 14 T reveals similar R_2 values of 85.7 and 82.6 $s^{-1}mM^{-1}$, respectively (**Figure 5-6b-c**). The effect of catechol capping is well demonstrated by comparing R_2 values for IOCCP-PEI and IOCCP with the R_2 value for a similar polymer coated SPION measured at the same field strength but with no catechol capping. CP coated SPIONs (IOCP) had a nearly 2-fold decrease in relaxivity with an R_2 value of 42.5 $s^{-1}mM^{-1}$, despite a slightly larger core diameter (~7.5 nm).[158] A decrease in core diameter is typically associated with decreased magnetic susceptibility due to the increased surface-area-to-volume ratio and the associated surface defects mentioned earlier. The drastic increase in relaxivity of catechol capped IOCCP-PEI and IOCCP as compared to IOCP demonstrates the catechol capping effect on the MR contrast enhancement capabilities of SPIONs.

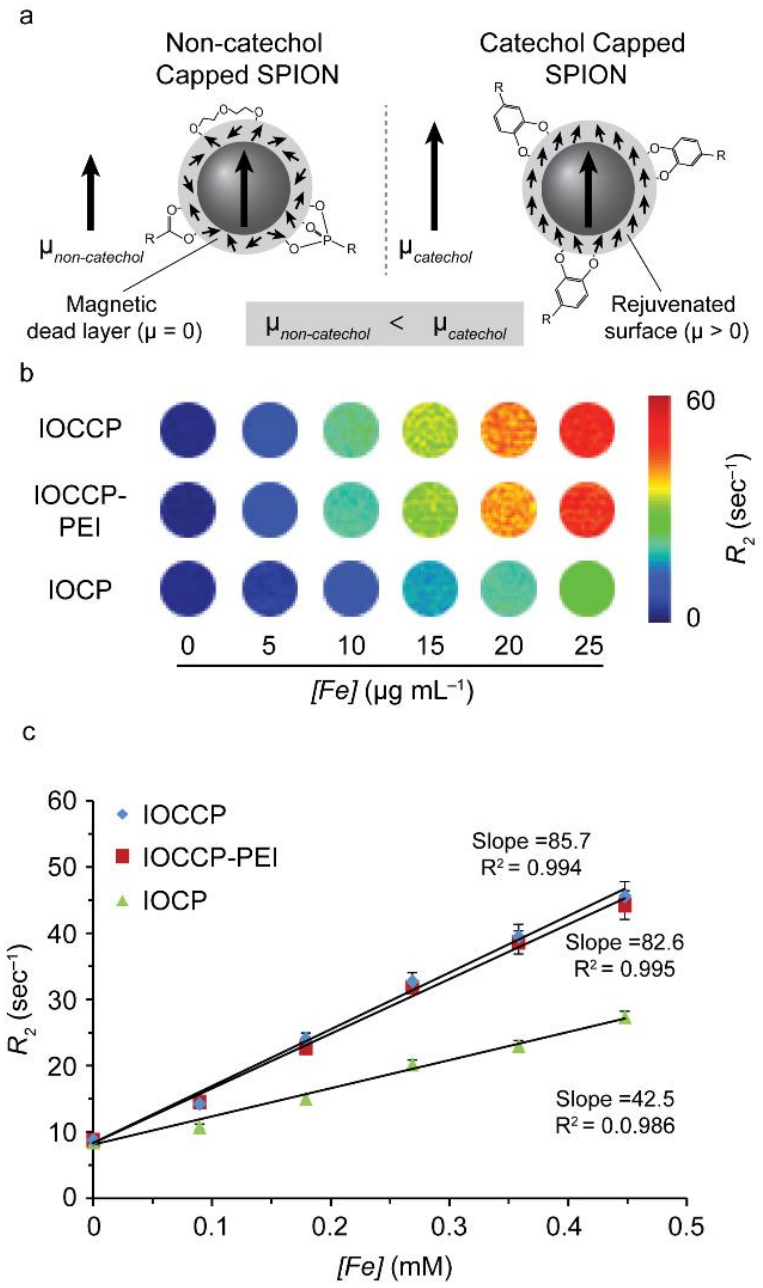

Figure 6-6. Characterization of MR relaxation properties for IOCCP-PEI and IOCCP. a) Illustration of the effect on the magnitude of magnetic moments of catechol capped SPION ($\mu_{catechol}$) compared to commonly utilized capping ligands, including carboxylates, phosphonates and ethylene glycol ($\mu_{non\text{-}catechol}$). b) Colorized R_2 maps of phantoms of IOCCP, IOCCP-PEI and IOCP at various iron concentrations. c) Magnetic R_2 relaxivity of IOCCP, IOCCP-PEI and IOCP was calculated to be 85.7, 82.6 and 42.5 $s^{-1}mM^{-1}$, respectively, at 14 T field strength.

6.3.3 IOCCP-PEI/DNA complex optimization

Gene delivery vectors must be able to efficiently condense DNA and maintain adequate size to traverse physiological barriers and reach target cells.[103b] Additionally, adequate cationic surface charge is needed to aid in cell binding and facilitate the proton sponge effect to encourage endosomal escape after cellular internalization.[165] SPION/DNA complexes at ratios (w/w) of 0, 2, 5, 10, and 20 to 1, SPION to red fluorescent protein encoding plasmid DNA (pRFP) were evaluated for their hydrodynamic size and ζ potential (**Figure 5-7a and b**). SPION/DNA complexed at a ratio of 10:1 produced the best combination of size (hydrodynamic size = 54.3 nm) and cationic surface charge (ζ potential = 16.2 mV) and were further evaluated *in vitro*. Cell toxicity was observed in pilot transfection studies using IOCCP-PEI at a 10:1 SPION/DNA ratio, consequently, IOCCP was further PEGylated (IOCCP-PEI-PEG) with amine reactive 12 unit PEG ($SMPEG_{12}$) at a 1:200 molar ratio of SPION to PEG to reduce charge and mitigate charge-induced toxicity.[166] The hydrodynamic size was not changed after the addition of PEG (54 nm) but the ζ potential was reduced slightly to 14.9 mV.

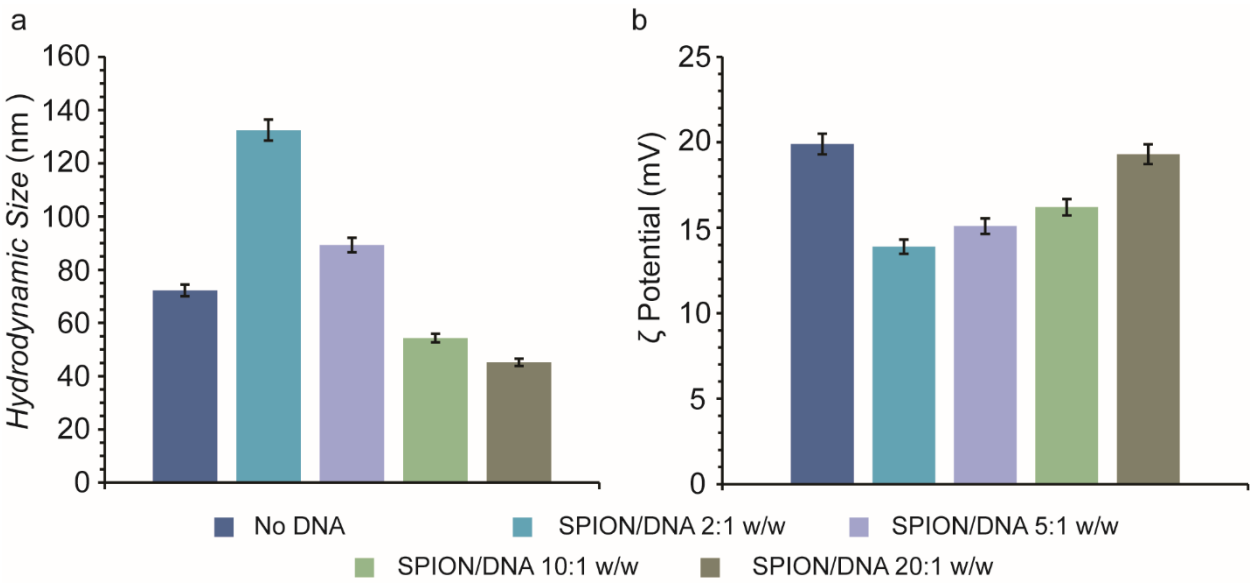

Figure 6-7. Physiochemical properties of IOCCP-PEI complexed at various SPION to DNA ratios. (a) Hydrodynamic size and (b) ζ potential in HEPES buffer pH 7.4 of IOCCP-PEI with no DNA and with DNA bound at a 2, 5, 10 or 20 to 1 SPION to DNA ratio.

6.3.4 In vitro evaluation of SPION complexed with pRFP DNA

SF767 cells treated with IOCCP, IOCCP-PEI, and IOCCP-PEI-PEG complexed with DNA at a 10:1 ratio were evaluated at doses of 0.1, 0.5, 1, 2, 3, and 4 µg pRFP using the alamarBlue reagent to assess any reduction in cell metabolic activity (**Figure 5-8a**). The results were normalized as a % of control cells to determine cell viability. To compare with commercially available and commonly used transfection agents, Lipofectamine and 25 kDa PEI were used as positive controls. Lipofectamine was complexed at the manufacturer's suggested ratio of 3:1 Lipofectamine to DNA, while PEI was complexed at a 10:1 ratio consistent with the SPION complexes. IOCCP showed no toxicity at all evaluated pRFP doses, which was expected given the lack of high cationic charge and subsequent modest ζ potential (5.8 mV). Lipofectamine complexes maintained high cell viability at dosages of 0.1 and 0.5 µg pRFP (97.4 ± 7.5 % and 91.7 ± 7.3 %, respectively) but showed significant toxicity at an elevated dosage of

4 µg pRFP (17.4% ± 2.6%). PEI was far more toxic exhibiting a cell viability of 72.9 ± 3.8 % at a dosage of 0.1 µg pRFP and 11.7 ± 0.8 % at a dosage of 4 µg pRFP. IOCCP-PEI exhibited similar cell viability to PEI at low dosages (69.5 ± 4.3 %, 0.1 µg pRFP), but maintained better cell viability with increased DNA dose (35.4 ± 2.9 %, 4 µg pRFP). The PEG modification to IOCCP-PEI-PEG mitigated toxicity, increasing viability from 69.5 ± 4.3 % to 85.5 ± 3.5 % at 0.1 µg pRFP and from 35.4 ± 2.9 % to 56.3 ± 7.1 % at 4 µg pRFP.

The transfection capabilities of IOCCP, IOCCP-PEI, and IOCCP-PEI-PEG were evaluated using RFP (1 µg) expression in SF767 cells and analyzed by flow cytometry (**Figure 5-8b**). IOCCP-PEI had the highest transfection efficiency with 93.4 ± 0.9 % of cells positive for RFP expression, followed by IOCCP-PEI-PEG (91.7 ± 0.5 %) and Lipofectamine (78.1 ± 3.6 %) as shown in the representative histogram overlays. To visualize RFP transfection of SF767 cells by IOCCP-PEI-PEG, cells were seeded on cover slips 24 h prior to 48 h incubation with SPIONs, nuclear stained (Dapi, blue), membrane stained (WGA-AF647, green) and evaluated by confocal fluorescence microscopy imaging (**Figure 5-8c**). IOCCP-PEI-PEG provides exceptional transfection efficiency with minimal toxicity as compared to PEI and commercially available Lipotectamine demonstrating potential as a gene delivery vector.

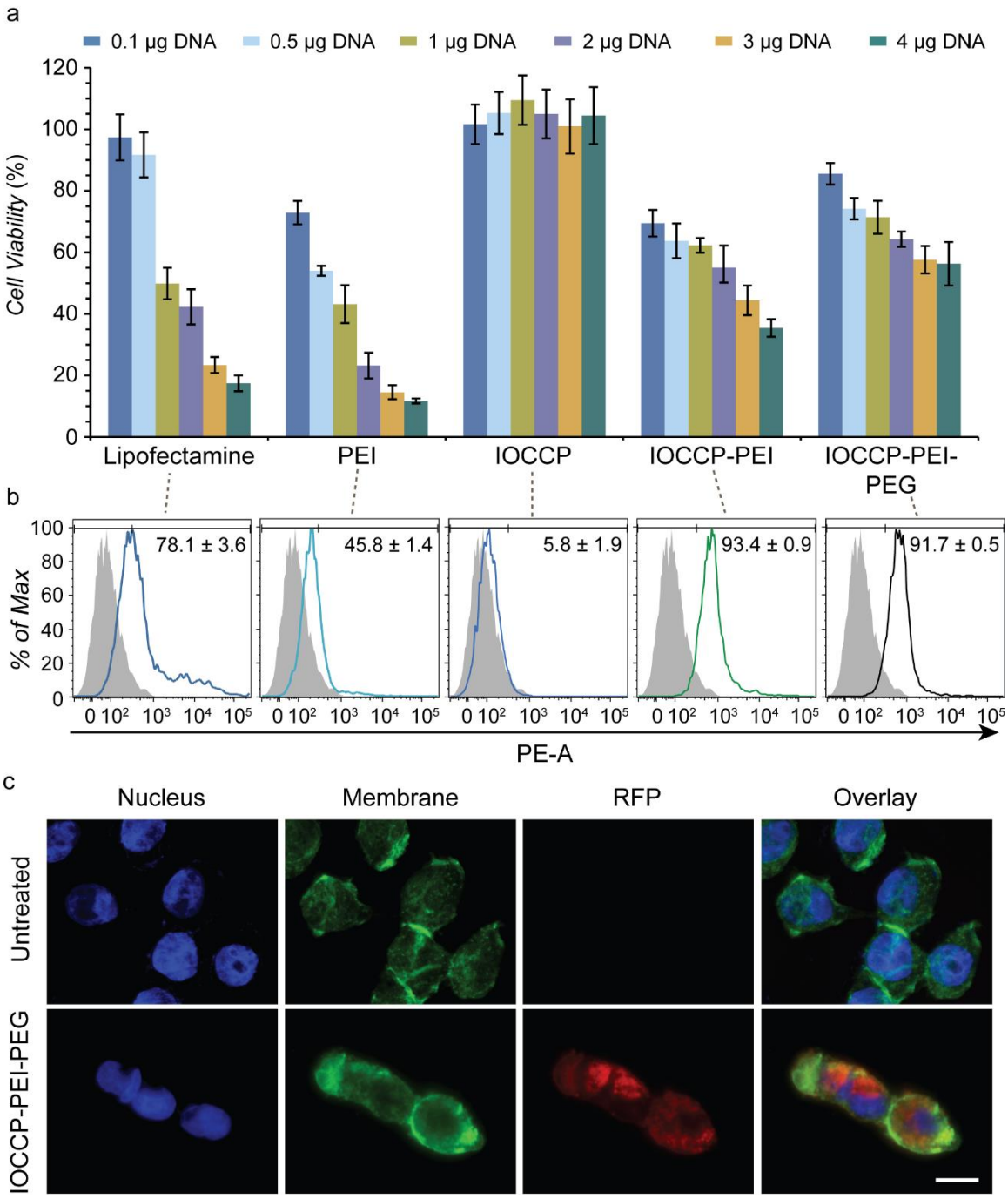

Figure 6-8. Assessment of cell viability and transfection efficiency in SF767 cells. (a) Evaluation of cytotoxicity by the alamarBlue assay after 48 h incubation with 0.1, 0.5, 1, 2, 3, or 4 µg of pRFP. IOCCP, IOCCP-PEI, IOCCP-PEI-PEG, and PEI were complexed at a 10:1 w/w ratio of DNA to transfection agent and Lipofectamine was complexed at a 3:1 w/w ratio. b) Representative histogram overlays of untreated SF767 cells compared with Lipofectamine, PEI, IOCCP, IOCCP-PEI, and IOCCP-PEI transfected cells at a dose of 1 µg pRFP. c) Confocal fluorescence microscopy imaging of untreated SF767 cells and SF767 cells treated with 1 µg pRFP complexed with IOCCP-PEI-PEG. The DAPI nuclear stain is shown in blue, the WGA-

AF647 membrane stain is shown in green and RFP expression is shown in red. The scale bar corresponds to 10 μm. 5000 cells analyzed; error bars indicate ± standard deviation.

6.4 Conclusions

In summary, the synthesis of multi-dentate catechol modified CP and CCP further modified with PEI permitted a rapid synthesis/coating/functionalization of theranostic SPIONs capable of efficient gene transfection. The modular approach allowed for fine-tuning of physiochemical properties by simply changing feed ratios of polymer constructs. The optimized PEI modified SPIONs displayed proper size and surface charge to navigate physiological barriers and successfully bind DNA. Catechol capping of the iron oxide surface lead to improved MR contrast enhancement over similar polymer coated SPIONs, demonstrating the potential utility of this SPION in real-time monitoring of gene delivery. Importantly, DNA loaded IOCCP-PEIs had excellent transfection efficiency *in vitro* and further modification with PEG greatly reduced toxicity without significantly hindering transfection efficiency.

7 Summary of Major Findings

Nanotechnology has the potential to drastically change current approaches to clinical cancer treatment and improve patient survival and quality of life. The goal of this thesis was to rationally design theranostic SPIONs following design parameters that provide optimal diagnostic capabilities, develop methods for administration that improve delivery of agents to brain tumors, improve the pharmacokinetics of delivered chemotherapeutics to address current cancer targeting limitations and poor pharmacokinetic of hydrophobic chemotherapeutics that lead to unacceptable side effects, and develop new synthesis/functionalization strategies to improve consistency and streamline production of theranostics SPIONs.

SPIONs modified with redox responsive cross-linked chitosan- PEG copolymer, functionalized with targeting agent CTX, and further modified with MGMT inhibitor, BG, to improve TMZ based GBM treatment strategies was evaluated as a targeted nanovector for CED to brain tumors in Chapter 3. These SPIONs had excellent solubility and physicochemical properties, and demonstrated a redox-responsive drug release profile. *In vitro* suppression of MGMT in human GBM cells treated with BG modified SPIONs significantly potentiated sensitivity to TMZ. Co-treatment of BG labeled SPION and TMZ in wild type mice showed a significant reduction in bone marrow toxicity when compared to free BG/TMZ treatments. This favorable toxicity profile was attributed to improved pharmacokinetics of BG when formulated with the SPION. Importantly, *in vivo* CED of the BG nanoformulation increased survival in human GBM animal models 3-fold over untreated mice.

To improve upon the drug loading of MGMT inhibitor presented in Chapter 4, BG analogs were modified to allow polymerization of drug on the SPION surface to increase drug loading and provide a pH responsive release mechanism in Chapter 5. BGS and DA-BGS were

evaluated *in vitro* as MGMT inhibitors and were shown to be to as effective as their BG counterpart. DA-BGS was successfully polymerized on the base SPION and achieved high drug loading and controlled drug released through hydrazone linkages that favored release of drug intracellularly. Importantly, suppression of MGMT in human GBM cells was on par with free BG. The increased drug loading of the BG nanoformulation should allow for less invasive administration of therapeutics and lead to a more tolerable treatment option for patients.

Chapter 6 presented a rapid synthesis/coating/functionalization approach for a PEI modified theranostic SPIONs for gene delivery to improve control over functionalization and increase batch to batch consistency. The modular approach allowed for fine-tuning of physiochemical properties by changing feed ratios of polymer modules, and allowed for simple, reproducible functionalization. Magnetic properties of the catechol capped SPION where drastically improved through spin-ordering on the surface of the iron oxide core and led to improved MR contrast enhancement over similar polymer coated SPIONs, demonstrating the potential utility of this SPION in real-time monitoring of therapeutic delivery. Importantly, DNA loaded, functionalized SPIONs exhibited improved transfection efficiency *in vitro* over commercially available Lipofectamine. Extrapolation of this synthesis approach by replacing PEI with therapeutics and/or targeting functionalities would allow for rapid production of customizable theranostic agents tailored to individual patient needs.

8 References

1. *World Cancer Report 2014*. WHO Press: 2014; p 630.
2. Kohler, B. A.; Sherman, R. L.; Howlader, N.; Jemal, A.; Ryerson, A. B.; Henry, K. A.; Boscoe, F. P.; Cronin, K. A.; Lake, A.; Noone, A.-M.; Henley, S. J.; Eheman, C. R.; Anderson, R. N.; Penberthy, L., Annual Report to the Nation on the Status of Cancer, 1975-2011, Featuring Incidence of Breast Cancer Subtypes by Race/Ethnicity, Poverty, and State. *Journal of the National Cancer Institute* **2015,** *107* (6).
3. Bregoli, L.; Movia, D.; Gavigan-Imedio, J. D.; Lysaght, J.; Reynolds, J.; Prina-Mello, A., Nanomedicine applied to translational oncology: A future perspective on cancer treatment. *Nanomedicine: Nanotechnology, Biology and Medicine* **2016,** *12* (1), 81-103.
4. Edelman, R. D., et al, *MRI: Clinical Magnetic Resonance Imaging*. 2 ed.; W. B. Saunders Company: Philadelphia, Pennsylvania, 1996; Vol. 1, p 1150.
5. Ferrari, M., Cancer nanotechnology: opportunities and challenges. *Nat Rev Cancer* **2005,** *5* (3), 161-71.
6. Wickline, S. A.; Neubauer, A. M.; Winter, P. M.; Caruthers, S. D.; Lanza, G. M., Molecular imaging and therapy of atherosclerosis with targeted nanoparticles. *J. Magn. Reson. Imaging* **2007,** *25* (4), 667-680.
7. Corot, C.; Petry, K. G.; Trivedi, R.; Saleh, A.; Jonkmanns, C.; Le Bas, J. F.; Blezer, E.; Rausch, M.; Brochet, B.; Foster-Gareau, P.; Baleriaux, D.; Gaillard, S.; Dousset, V., Macrophage imaging in central nervous system and in carotid atherosclerotic plaque using ultrasmall superparamagnetic iron oxide in magnetic resonance imaging. *Invest. Radiol.* **2004,** *39* (10), 619-625.
8. Sun, C.; Lee, J. S. H.; Zhang, M. Q., Magnetic nanoparticles in MR imaging and drug delivery. *Adv. Drug Deliv. Rev.* **2008,** *60* (11), 1252-1265.
9. Sun, C.; Du, K.; Fang, C.; Bhattarai, N.; Veiseh, O.; Kievit, F.; Stephen, Z.; Lee, D.; Ellenbogen, R. G.; Ratner, B.; Zhang, M., PEG-mediated synthesis of highly dispersive multifunctional superparamagnetic nanoparticles: their physicochemical properties and function in vivo. *ACS nano* **2010,** *4* (4), 2402-10.
10. Weissleder, R.; Stark, D. D.; Engelstad, B. L.; Bacon, B. R.; Compton, C. C.; White, D. L.; Jacobs, P.; Lewis, J., Superparamagnetic Iron-Oxide - Pharmacokinetics And Toxicity. *Am. J. Roentgenol.* **1989,** *152* (1), 167-173.
11. Wang, Y.-X.; Hussain, S.; Krestin, G., Superparamagnetic iron oxide contrast agents: physicochemical characteristics and applicatons in MR imaging. *European Radiology* **2001,** *11* (11), 2319-2331.
12. Bonnemain, B., Superparamagnetic agents in magnetic resonance imaging: Physicochemical characteristics and clinical applications - A review. *J. Drug Target.* **1998,** *6* (3), 167-174.
13. Harisinghani, M. G.; Barentsz, J.; Hahn, P. F.; Deserno, W. M.; Tabatabaei, S.; van de Kaa, C. H.; de la Rosette, J.; Weissleder, R., Noninvasive detection of clinically occult lymph-node metastases in prostate cancer. *New England Journal of Medicine* **2003,** *348* (25), 2491-U5.
14. Veiseh, O.; Gunn, J. W.; Zhang, M., Design and fabrication of magnetic nanoparticles for targeted drug delivery and imaging. *Adv. Drug Deliv. Rev.* **2010,** *62* (3), 284-304.

15. Berry, E., Bulpitt, A., *Fundamentals of MRI*. CRC Press: Boca Raton, 2009; p 298.
16. Westbrook, C., Roth, C., Talbot, J., *MRI in Practice*. 3 ed.; Wiley-Blackwell: Hoboken, NJ, 2005; p 424.
17. Na, H. B.; Song, I. C.; Hyeon, T., Inorganic Nanoparticles for MRI Contrast Agents. *Advanced Materials* **2009,** *21* (21), 2133.
18. (a) Clarkson, R. B., Blood-pool MRI contrast agents: Properties and characterization. In *Contrast Agents I*, 2002; Vol. 221, pp 201-235; (b) Terreno, E.; Castelli, D. D.; Viale, A.; Aime, S., Challenges for Molecular Magnetic Resonance Imaging. *Chemical Reviews* **2010,** *110* (5), 3019.
19. Bedanta, S.; Kleemann, W., Supermagnetism. *Journal of Physics D: Applied Physics* **2009,** *42* (1), 013001.
20. (a) Gossuin, Y.; Gillis, P.; Hocq, A.; Vuong, Q. L.; Roch, A., Magnetic resonance relaxation properties of superparamagnetic particles. *Wiley Interdisciplinary Reviews: Nanomedicine and Nanobiotechnology* **2009,** *1* (3), 299; (b) Mathew, D. S.; Juang, R.-S., An overview of the structure and magnetism of spinel ferrite nanoparticles and their synthesis in microemulsions. *Chemical Engineering Journal* **2007,** *129* (1-3), 51; (c) Krishnan, K., Biomedical Nanomagnetics: A Spin Through Possibilities in Imaging, Diagnostics, and Therapy. *IEEE Transactions on Magnetics* **2010,** *46* (7), 2523 - 2558.
21. Butler, R. F.; Banerjee, S. K., Theoretical Single-Domain Grain-Size Range in Magnetite and Titatnomagnetite. *Journal of Geophysical Research* **1975,** *80* (29), 4049-4058.
22. Holz, M., L. Banci, L. Bertini and C. Luchinat. Nuclear and electron relaxation. The magnetic nucleus-unpaired electron coupling in solution. VCH, Weinheim, New York, Basel, Cambridge, 1991, pp. 216, DM 118. ISBN 3-527-28306-4. *Magnetic Resonance in Chemistry* **1993,** *31* (13), S154.
23. (a) Lipinski, M. J.; Briley-Saebo, K. C.; Mani, V.; Fayad, Z. A., "Positive Contrast" Inversion-Recovery With Oxide Nanoparticles-Resonant Water Suppression Magnetic Resonance Imaging: A Change for the Better? *Journal of the American College of Cardiology* **2008,** *52* (6), 492; (b) Branca, R. T.; Cleveland, Z. I.; Fubara, B.; Kumar, C. S. S. R.; Maronpot, R. R.; Leuschner, C.; Warren, W. S.; Driehuys, B., Molecular MRI for sensitive and specific detection of lung metastases. *Proceedings of the National Academy of Sciences* **2010,** *107* (8), 3693-3697.
24. Senpan, A.; Caruthers, S. D.; Rhee, I.; Mauro, N. A.; Pan, D.; Hu, G.; Scott, M. J.; Fuhrhop, R. W.; Gaffney, P. J.; Wickline, S. A.; Lanza, G. M., Conquering the Dark Side: Colloidal Iron Oxide Nanoparticles. *ACS Nano* **2009,** *3* (12), 3917-3926.
25. (a) Park, J. Y.; Daksha, P.; Lee, G. H.; Woo, S.; Chang, Y. M., Highly water-dispersible PEG surface modified ultra small superparamagnetic iron oxide nanoparticles useful for target-specific biomedical applications. *Nanotechnology* **2008,** *19* (36), 7; (b) Di Marco, M., Sadun, C., Port, M., Guilber, I., Couveur, P., Dubernet, C., Physicochemical characterization of ultrasmall superparamagnetic iron oxide particles (USPIO) for biomedical application as MRI contrast agents. *Interanational Journal of Nanomedicine* **2007,** *2* (4), 609-622.
26. Jun, Y.-w.; Huh, Y.-M.; Choi, J.-s.; Lee, J.-H.; Song, H.-T.; KimKim; Yoon, S.; Kim, K.-S.; Shin, J.-S.; Suh, J.-S.; Cheon, J., Nanoscale Size Effect of Magnetic Nanocrystals and Their Utilization for Cancer Diagnosis via Magnetic Resonance Imaging. *Journal of the American Chemical Society* **2005,** *127* (16), 5732-5733.

27. Bae, K., Kim, BY, Lee, Y, Hwang, JY, Park, HW, Park, TG, Bioinspired Synthesis and Characterization of Gadolinium-Labeled

Magnetite Nanoparticles for Dual Contrast *T*1- and *T*2-Weighted Magnetic

Resonance Imaging. *Bioconjugate Chemistry* **2010,** *21*, 505-512.
28. (a) Ding, D.; Kanaly, C. W.; Bigner, D. D.; Cummings, T. J.; Herndon, J. E.; Pastan, I.; Raghavan, R.; Sampson, J. H., Convection-enhanced delivery of free gadolinium with the recombinant immunotoxin MR1-1. *J. Neuro-Oncol.* **2010,** *98* (1), 1-7; (b) Ding, D.; Kanaly, C. W.; Cummings, T. J.; Herndon, J. E.; Raghavan, R.; Sampson, J. H., Long-term safety of combined intracerebral delivery of free gadolinium and targeted chemotherapeutic agent PRX321. *Neurol. Res.* **2010,** *32* (8), 810-815.
29. (a) Veiseh, O.; Sun, C.; Fang, C.; Bhattarai, N.; Gunn, J.; Kievit, F.; Du, K.; Pullar, B.; Lee, D.; Ellenbogen, R. G.; Olson, J.; Zhang, M. Q., Specific Targeting of Brain Tumors with an Optical/Magnetic Resonance Imaging Nanoprobe across the Blood-Brain Barrier. *Cancer Res.* **2009,** *69* (15), 6200-6207; (b) Sun, C.; Fang, C.; Stephen, Z.; Veiseh, O.; Hansen, S.; Lee, D.; Ellenbogen, R. G.; Olson, J.; Zhang, M., Tumor-targeted drug delivery and MRI contrast enhancement by chlorotoxin-conjugated iron oxide nanoparticles. *Nanomed* **2008,** *3* (4), 495-505.
30. Veiseh, O.; Kievit, F. M.; Fang, C.; Mu, N.; Jana, S.; Leung, M. C.; Mok, H.; Ellenbogen, R. G.; Park, J. O.; Zhang, M., Chlorotoxin bound magnetic nanovector tailored for cancer cell targeting, imaging, and siRNA delivery. *biomaterials* **2010,** *31* (31), 8032-42.
31. Veiseh, O.; Kievit, F. M.; Gunn, J. W.; Ratner, B. D.; Zhang, M., A ligand-mediated nanovector for targeted gene delivery and transfection in cancer cells. *biomaterials* **2009,** *30* (4), 649-57.
32. (a) Moffat, B. A., Ramachandra Reddy, G., McConville, P., Hall, D., Chenevert., T.L., Kopelman, R.R., Philber, M., Weissleder, R., Rehemtulla, A., Ross, B.D., A Novel Polyacrylamide Magnetic Nanoparticle Contrast Agent for Molecular Imaging using MRI. *Molecular Imaging* **2003,** *2* (4), 324-332; (b) Heyn, C.; Bowen, C. V.; Rutt, B. K.; Foster, P. J., Detection threshold of single SPIO-labeled cells with FIESTA. *Magnetic Resonance in Medicine* **2005,** *53* (2), 312; (c) Cole, A. J.; David, A. E.; Wang, J.; Galbán, C. J.; Hill, H. L.; Yang, V. C., Polyethylene glycol modified, cross-linked starch-coated iron oxide nanoparticles for enhanced magnetic tumor targeting. *Biomaterials* **2010,** *32* (8), 2183.
33. (a) Moteki, T.; Sekine, T., Echo planar MR imaging of the liver: Comparison of images with and without motion probing gradients. *J. Magn. Reson. Imaging* **2004,** *19* (1), 82-90; (b) Kumano, S.; Murakami, T.; Kim, T.; Hori, M.; Okada, A.; Sugiura, T.; Noguchi, Y.; Kawata, S.; Tomoda, K.; Nakamura, H., Using superparamagnetic iron oxide-enhanced MRI to differentiate metastatic hepatic tumors and nonsolid benign lesions. *Am. J. Roentgenol.* **2003,** *181* (5), 1335-1339.
34. Phelps, M. E., PET: The Merging of Biology and Imaging into Molecular Imaging. *J Nucl Med* **2000,** *41* (4), 661-681.
35. Fukukura, Y.; Kamiyama, T.; Takumi, K.; Shindo, T.; Higashi, R.; Nakajo, M., Comparison of ferucarbotran-enhanced fluid-attenuated inversion-recovery echo-planar, T2-weighted turbo spin-echo, T2*-weighted gradient-echo, and diffusion-weighted echo-planar imaging for detection of malignant liver lesions. *Journal of Magnetic Resonance Imaging* **2010,** *31* (3), 607-616.

36. (a) Stuber, M.; Gilson, W. D.; Schär, M.; Kedziorek, D. A.; Hofmann, L. V.; Shah, S.; Vonken, E.-J.; Bulte, J. W. M.; Kraitchman, D. L., Positive contrast visualization of iron oxide-labeled stem cells using inversion-recovery with ON-resonant water suppression (IRON). *Magnetic Resonance in Medicine* **2007,** *58* (5), 1072; (b) Korosoglou, G.; Weiss, R. G.; Kedziorek, D. A.; Walczak, P.; Gilson, W. D.; Schär, M.; Sosnovik, D. E.; Kraitchman, D. L.; Boston, R. C.; Bulte, J. W. M.; Weissleder, R.; Stuber, M., Noninvasive Detection of Macrophage-Rich Atherosclerotic Plaque in Hyperlipidemic Rabbits Using "Positive Contrast" Magnetic Resonance Imaging. *Journal of the American College of Cardiology* **2008,** *52* (6), 483; (c) Suzuki, Y.; Cunningham, C. H.; Noguchi, K.-i.; Chen, I. Y.; Weissman, I. L.; Yeung, A. C.; Robbins, R. C.; Yang, P. C., In vivo serial evaluation of superparamagnetic iron-oxide labeled stem cells by off-resonance positive contrast. *Magnetic Resonance in Medicine* **2008,** *60* (6), 1269.

37. Mani, V.; Briley-Saebo, K. C.; Itskovich, V. V.; Samber, D. D.; Fayad, Z. A., Gradient echo acquisition for superparamagnetic particles with positive contrast (GRASP): Sequence characterization in membrane and glass superparamagnetic iron oxide phantoms at 1.5T and 3T. *Magnetic Resonance in Medicine* **2006,** *55* (1), 126.

38. Cunningham, C. H.; Arai, T.; Yang, P. C.; McConnell, M. V.; Pauly, J. M.; Conolly, S. M., Positive contrast magnetic resonance imaging of cells labeled with magnetic nanoparticles. *Magnetic Resonance in Medicine* **2005,** *53* (5), 999.

39. (a) Posse, S., DIRECT IMAGING OF MAGNETIC-FIELD GRADIENTS BY GROUP SPIN-ECHO SELECTION. *Magnetic Resonance in Medicine* **1992,** *25* (1), 12-29; (b) Reichenbach, J. R.; Venkatesan, R.; Yablonskiy, D. A.; Thompson, M. R.; Lai, S.; Haacke, E. M., Theory and application of static field inhomogeneity effects in gradient-echo imaging. *Jmri-Journal of Magnetic Resonance Imaging* **1997,** *7* (2), 266-279.

40. Liu, W.; Dahnke, H.; Jordan, E. K.; Schaeffter, T.; Frank, J. A., In vivo MRI using positive-contrast techniques in detection of cells labeled with superparamagnetic iron oxide nanoparticles. *Nmr In Biomedicine* **2008,** *21* (3), 242-250.

41. (a) Yoo, M. K.; Park, I. Y.; Kim, I. Y.; Park, I. K.; Kwon, J. S.; Jeong, H. J.; Jeong, Y. Y.; Cho, C. S., Superparamagnetic Iron Oxide Nanoparticles Coated with Mannan for Macrophage Targeting. *J. Nanosci. Nanotechnol.* **2008,** *8* (10), 5196-5202; (b) Forge, D.; Roch, A.; Laurent, S.; Tellez, H.; Gossuin, Y.; Renaux, F.; Vander Elst, L.; Muller, R. N., Optimization of the Synthesis of Superparamagnetic Contrast Agents by the Design of Experiments Method. *J. Phys. Chem. C* **2008,** *112* (49), 19178-19185; (c) Finotelli, P. V.; Sampaio, D. A.; Morales, M. A.; Rossi, A. M.; Rocha-Leao, M. H., Ca ALGINATE AS SCAFFOLD FOR IRON OXIDE NANOPARTICLES SYNTHESIS. *Braz. J. Chem. Eng.* **2008,** *25* (4), 759-764.

42. (a) Meledandri, C. J.; Stolarczyk, J. K.; Ghosh, S.; Brougham, D. F., Nonaqueous Magnetic Nanoparticle Suspensions with Controlled Particle Size and Nuclear Magnetic Resonance Properties. *Langmuir* **2008,** *24* (24), 14159-14165; (b) Maity, D.; Ding, J.; Xue, J. M., SYNTHESIS OF MAGNETITE NANOPARTICLES BY THERMAL DECOMPOSITION: TIME, TEMPERATURE, SURFACTANT AND SOLVENT EFFECTS. *Funct. Mater. Lett.* **2008,** *1* (3), 189-193.

43. Gupta, A. K.; Gupta, M., Synthesis and surface engineering of iron oxide nanoparticles for biomedical applications. *Biomaterials* **2005,** *26* (18), 3995-4021.

44. Sjögren, C. E.; Johansson, C.; Nævestad, A.; Sontum, P. C.; Briley-Sæbø, K.; Fahlvik, A. K., Crystal size and properties of superparamagnetic iron oxide (SPIO) particles. *Magnetic Resonance Imaging* **1997,** *15* (1), 55-67.

45. Nedkov, I.; Merodiiska, T.; Slavov, L.; Vandenberghe, R. E.; Kusano, Y.; Takada, J., Surface oxidation, size and shape of nano-sized magnetite obtained by co-precipitation. *Journal of Magnetism and Magnetic Materials* **2006,** *300* (2), 358.
46. Park, J.; An, K. J.; Hwang, Y. S.; Park, J. G.; Noh, H. J.; Kim, J. Y.; Park, J. H.; Hwang, N. M.; Hyeon, T., Ultra-large-scale syntheses of monodisperse nanocrystals. *Nat. Mater.* **2004,** *3* (12), 891-895.
47. Sun, S.; Zeng, H.; Robinson, D. B.; Raoux, S.; Rice, P. M.; Wang, S. X.; Li, G., Monodisperse MFe2O4 (M = Fe, Co, Mn) Nanoparticles. *Journal of the American Chemical Society* **2003,** *126* (1), 273.
48. Lu, A.-H.; Salabas, E. L.; Schüth, F., Magnetic Nanoparticles: Synthesis, Protection, Functionalization, and Application. *Angewandte Chemie International Edition* **2007,** *46* (8), 1222.
49. Daou, T. J.; Greneche, J. M.; Pourroy, G.; Buathong, S.; Derory, A.; Ulhaq-Bouillet, C.; Donnio, B.; Guillon, D.; Begin-Colin, S., Coupling agent effect on magnetic properties of functionalized magnetite-based nanoparticles. *Chem. Mat.* **2008,** *20* (18), 5869-5875.
50. Zhang, Y.; Sun, C.; Kohler, N.; Zhang, M., Self-assembled coatings on individual monodisperse magnetite nanoparticles for efficient intracellular uptake. *Biomed Microdevices* **2004,** *6* (1), 33-40.
51. Berry, C. C.; Curtis, A. S. G., Functionalisation of magnetic nanoparticles for applications in biomedicine. *Journal of Physics D-Applied Physics* **2003,** *36* (13), R198-R206.
52. Otsuka, H.; Nagasaki, Y.; Kataoka, K., PEGylated nanoparticles for biological and pharmaceutical applications. *Adv. Drug Deliv. Rev.* **2003,** *55* (3), 403-419.
53. Jia, G. W.; Cao, Z. Q.; Xue, H.; Xu, Y. S.; Jiang, S. Y., Novel Zwitterionic-Polymer-Coated Silica Nanoparticles. *Langmuir* **2009,** *25* (5), 3196-3199.
54. (a) Fang, C.; Zhang, M. Q., Multifunctional magnetic nanoparticles for medical imaging applications. *Journal of materials chemistry* **2009,** *19* (35), 6258-6266; (b) Veiseh, O.; Sun, C.; Fang, C.; Bhattarai, N.; Gunn, J.; Kievit, F.; Du, K.; Pullar, B.; Lee, D.; Ellenbogen, R. G.; Olson, J.; Zhang, M., Specific targeting of brain tumors with an optical/magnetic resonance imaging nanoprobe across the blood-brain barrier. *Cancer Res* **2009,** *69* (15), 6200-7.
55. Duan, H.; Kuang, M.; Wang, X.; Wang, Y. A.; Mao, H.; Nie, S., Reexamining the Effects of Particle Size and Surface Chemistry on the Magnetic Properties of Iron Oxide Nanocrystals: New Insights into Spin Disorder and Proton Relaxivity. *The Journal of Physical Chemistry C* **2008,** *112* (22), 8127.
56. LaConte, L. E. W.; Nitin, N.; Zurkiya, O.; Caruntu, D.; O'Connor, C. J.; Hu, X.; Bao, G., Coating thickness of magnetic iron oxide nanoparticles affects R2 relaxivity. *J. Magn. Reson. Imaging* **2007,** *26* (6), 1634.
57. Hu, F.; Joshi, H. M.; Dravid, V. P.; Meade, T. J., High-performance nanostructured MR contrast probes. *Nanoscale* **2010,** *2* (10), 1884.
58. Vergara, A.; Paduano, L.; Vitagliano, V.; Sartorio, R., Mutual diffusion in aqueous solution of poly(ethyleneglycol) samples. Some comments on the effect of chain length and polydispersity. *Physical Chemistry Chemical Physics* **1999,** *1* (23), 5377-5383.
59. (a) Longmire, M.; Choyke, P. L.; Kobayashi, H., Clearance properties of nano-sized particles and molecules as imaging agents: considerations and caveats. *Nanomedicine* **2008,** *3* (5), 703-717; (b) Kievit, F. M.; Veiseh, O.; Bhattarai, N.; Fang, C.; Gunn, J. W.; Lee, D.; Ellenbogen, R. G.; Olson, J. M.; Zhang, M., PEI-PEG-Chitosan Copolymer Coated Iron Oxide

Nanoparticles for Safe Gene Delivery: synthesis, complexation, and transfection. *Adv Funct Mater* **2009,** *19* (14), 2244-2251.
60. Sunderland, C. J.; Steiert, M.; Talmadge, J. E.; Derfus, A. M.; Barry, S. E., Targeted nanoparticles for detecting and treating cancer. *Drug Development Research* **2006,** *67* (1), 70-93.
61. Alexis, F.; Rhee, J. W.; Richie, J. P.; Radovic-Moreno, A. F.; Langer, R.; Farokhzad, O. C., New frontiers in nanotechnology for cancer treatment. *Urol Oncol* **2008,** *26* (1), 74-85.
62. Sun, C.; Veiseh, O.; Gunn, J.; Fang, C.; Hansen, S.; Lee, D.; Sze, R.; Ellenbogen, R. G.; Olson, J.; Zhang, M., In vivo MRI detection of gliomas by chlorotoxin-conjugated superparamagnetic nanoprobes. *Small* **2008,** *4* (3), 372-9.
63. (a) Fang, C.; Veiseh, O.; Kievit, F.; Bhattarai, N.; Wang, F.; Stephen, Z.; Li, C.; Lee, D.; Ellenbogen, R. G.; Zhang, M., Functionalization of iron oxide magnetic nanoparticles with targeting ligands: their physicochemical properties and in vivo behavior. *Nanomedicine* **2010,** *5* (9), 1357-1369; (b) Kumar, M.; Medarova, Z.; Pantazopoulos, P.; Dai, G.; Moore, A., Novel membrane-permeable contrast agent for brain tumor detection by MRI. *Magnetic Resonance in Medicine* **2010,** *63* (3), 617.
64. (a) Larsen, B., Haag, MA, Serkova, NJ, Shroyer, KR, Stoldt, CR, Controlled aggregation of superparamagnetic iron oxide nanoparticles for the development of molecular magnetic resonance imaging probes. *Nanotechnology* **2008,** *19* (26); (b) Roch, A.; Gossuin, Y.; Muller, R. N.; Gillis, P., Superparamagnetic colloid suspensions: Water magnetic relaxation and clustering. *Journal of Magnetism and Magnetic Materials* **2005,** *293* (1), 532-539.
65. (a) Kievit, F. M.; Veiseh, O.; Fang, C.; Bhattarai, N.; Lee, D.; Ellenbogen, R. G.; Zhang, M., Chlorotoxin Labeled Magnetic Nanovectors for Targeted Gene Delivery to Glioma. *ACS Nano* **2010,** *4* (8), 4587; (b) Bartlett, D. W.; Su, H.; Hildebrandt, I. J.; Weber, W. A.; Davis, M. E., Impact of Tumor-Specific Targeting on the Biodistribution and Efficacy of siRNA Nanoparticles Measured by Multimodality in vivo Imaging. *Proceedings of the National Academy of Sciences of the United States of America* **2007,** *104* (39), 15549-15554; (c) Choi, C. H. J.; Alabi, C. A.; Webster, P.; Davis, M. E., Mechanism of active targeting in solid tumors with transferrin-containing gold nanoparticles. *Proceedings of the National Academy of Sciences* **2010,** *107* (3), 1235-1240.
66. (a) Veiseh, O.; Sun, C.; Gunn, J.; Kohler, N.; Gabikian, P.; Lee, D.; Bhattarai, N.; Ellenbogen, R.; Sze, R.; Hallahan, A.; Olson, J.; Zhang, M., Optical and MRI multifunctional nanoprobe for targeting gliomas. *Nano Lett* **2005,** *5* (6), 1003-8; (b) Lee, M. J. E.; Veiseh, O.; Bhattarai, N.; Sun, C.; Hansen, S. J.; Ditzler, S.; Knoblaugh, S.; Lee, D.; Ellenbogen, R.; Zhang, M. Q.; Olson, J. M., Rapid Pharmacokinetic and Biodistribution Studies Using Cholorotoxin-Conjugated Iron Oxide Nanoparticles: A Novel Non-Radioactive Method. *PLoS One* **2010,** *5* (3), 8.
67. (a) Lee, H. Y.; Li, Z.; Chen, K.; Hsu, A. R.; Xu, C. J.; Xie, J.; Sun, S. H.; Chen, X. Y., PET/MRI dual-modality tumor imaging using arginine-glycine-aspartic (RGD) - Conjugated radiolabeled iron oxide nanoparticles. *J. Nucl. Med.* **2008,** *49* (8), 1371-1379; (b) Xie, J.; Chen, K.; Huang, J.; Lee, S.; Wang, J. H.; Gao, J.; Li, X. G.; Chen, X. Y., PET/NIRF/MRI triple functional iron oxide nanoparticles. *Biomaterials* **2010,** *31* (11), 3016-3022.
68. (a) Cizek, J.; Herholz, K.; Vollmar, S.; Schrader, R.; Klein, J.; Heiss, W. D., Fast and robust registration of PET and MR images of human brain. *Neuroimage* **2004,** *22* (1), 434-442; (b) Myers, R., The application of PET-MR image registration in the brain. *British Journal of Radiology* **2002,** *75*, S31-S35.

69. Sharma, H.; Mishra, P. K.; Talegaonkar, S.; Vaidya, B., Metal nanoparticles: a theranostic nanotool against cancer. *Drug Discov Today* **2015,** *20* (9), 1143-51.
70. Laurent, S.; Saei, A. A.; Behzadi, S.; Panahifar, A.; Mahmoudi, M., Superparamagnetic iron oxide nanoparticles for delivery of therapeutic agents: opportunities and challenges. *Expert Opin. Drug Deliv.* **2014,** *11* (9), 1449-1470.
71. Cole, J. T.; Holland, N. B., Multifunctional nanoparticles for use in theranostic applications. *Drug Deliv. Transl. Res.* **2015,** *5* (3), 295-309.
72. Sharma, H.; Mishra, P. K.; Talegaonkar, S.; Vaidya, B., Metal nanoparticles: a theranostic nanotool against cancer. *Drug Discov. Today* **2015,** *20* (9), 1143-1151.
73. Li, J.; Gupta, S.; Li, C., Research perspectives: gold nanoparticles in cancer theranostics. *Quantitative imaging in medicine and surgery* **2013,** *3* (6), 284-91.
74. Patil, U. S.; Adireddy, S.; Jaiswal, A.; Mandava, S.; Lee, B. R.; Chrisey, D. B., In Vitro/In Vivo Toxicity Evaluation and Quantification of Iron Oxide Nanoparticles. *Int J Mol Sci* **2015,** *16* (10), 24417-50.
75. Lee, M. J.; Veiseh, O.; Bhattarai, N.; Sun, C.; Hansen, S. J.; Ditzler, S.; Knoblaugh, S.; Lee, D.; Ellenbogen, R.; Zhang, M.; Olson, J. M., Rapid pharmacokinetic and biodistribution studies using cholorotoxin-conjugated iron oxide nanoparticles: a novel non-radioactive method. *PLoS One* **2010,** *5* (3), e9536.
76. (a) Liu, W.; Frank, J. A., Detection and quantification of magnetically labeled cells by cellular MRI. *European journal of radiology* **2009,** *70* (2), 258-64; (b) Liu, Y.; Yang, Y.; Zhang, C., A concise review of magnetic resonance molecular imaging of tumor angiogenesis by targeting integrin alphavbeta3 with magnetic probes. *International journal of nanomedicine* **2013,** *8*, 1083-93.
77. (a) Young, I. R.; Cox, I. J.; Bryant, D. J.; Bydder, G. M., The benefits of increasing spatial resolution as a means of reducing artifacts due to field inhomogeneities. *Magn Reson Imaging* **1988,** *6* (5), 585-90; (b) Frahm, J.; Merboldt, K. D.; Hanicke, W., Direct FLASH MR imaging of magnetic field inhomogeneities by gradient compensation. *Magn Reson Med* **1988,** *6* (4), 474-80; (c) Kuhlpeter, R.; Dahnke, H.; Matuszewski, L.; Persigehl, T.; von Wallbrunn, A.; Allkemper, T.; Heindel, W. L.; Schaeffter, T.; Bremer, C., R2 and R2* mapping for sensing cell-bound superparamagnetic nanoparticles: in vitro and murine in vivo testing. *Radiology* **2007,** *245* (2), 449-57; (d) Walczak, P.; Kedziorek, D. A.; Gilad, A. A.; Barnett, B. P.; Bulte, J. W., Applicability and limitations of MR tracking of neural stem cells with asymmetric cell division and rapid turnover: the case of the shiverer dysmyelinated mouse brain. *Magn Reson Med* **2007,** *58* (2), 261-9.
78. (a) Bowen, C. V.; Zhang, X.; Saab, G.; Gareau, P. J.; Rutt, B. K., Application of the static dephasing regime theory to superparamagnetic iron-oxide loaded cells. *Magn Reson Med* **2002,** *48* (1), 52-61; (b) Yablonskiy, D. A.; Haacke, E. M., Theory of NMR signal behavior in magnetically inhomogeneous tissues: the static dephasing regime. *Magn Reson Med* **1994,** *32* (6), 749-63; (c) Simon, G. H.; Bauer, J.; Saborovski, O.; Fu, Y.; Corot, C.; Wendland, M. F.; Daldrup-Link, H. E., T1 and T2 relaxivity of intracellular and extracellular USPIO at 1.5T and 3T clinical MR scanning. *Eur Radiol* **2006,** *16* (3), 738-45.
79. (a) Gutierrez, L.; Mejias, R.; Barber, D. F.; Veintemillas-Verdaguer, S.; Serna, C. J.; Lazaro, F. J.; Morales, M. P., Ac magnetic susceptibility study of in vivo nanoparticle biodistribution. *Journal of Physics D-Applied Physics* **2011,** *44* (25), 9; (b) Mejias, R.; Gutierrez, L.; Salas, G.; Perez-Yague, S.; Zotes, T. M.; Lazaro, F. J.; Morales, M. P.; Barber, D. F., Long term biotransformation and toxicity of dimercaptosuccinic acid-coated magnetic

nanoparticles support their use in biomedical applications. *Journal of Controlled Release* **2013,** *171* (2), 225-233.
80. Ferguson, R. M.; Khandhar, A. P.; Kemp, S. J.; Arami, H.; Saritas, E. U.; Croft, L. R.; Konkle, J.; Goodwill, P. W.; Halkola, A.; Rahmer, J.; Borgert, J.; Conolly, S. M.; Krishnan, K. M., Magnetic particle imaging with tailored iron oxide nanoparticle tracers. *IEEE transactions on medical imaging* **2015,** *34* (5), 1077-84.
81. (a) Weizenecker, J.; Borgert, J.; Gleich, B., A simulation study on the resolution and sensitivity of magnetic particle imaging. *Physics in medicine and biology* **2007,** *52* (21), 6363-74; (b) Goodwill, P. W.; Saritas, E. U.; Croft, L. R.; Kim, T. N.; Krishnan, K. M.; Schaffer, D. V.; Conolly, S. M., X-space MPI: magnetic nanoparticles for safe medical imaging. *Advanced materials (Deerfield Beach, Fla.)* **2012,** *24* (28), 3870-7; (c) Weizenecker, J.; Gleich, B.; Rahmer, J.; Dahnke, H.; Borgert, J., Three-dimensional real-time in vivo magnetic particle imaging. *Physics in medicine and biology* **2009,** *54* (5), L1-l10.
82. (a) Goodwill, P. W.; Tamrazian, A.; Croft, L. R.; Lu, C. D.; Johnson, E. M.; Pidaparthi, R.; Ferguson, R. M.; Khandhar, A. P.; Krishnan, K. M.; Conolly, S. M., Ferrohydrodynamic relaxometry for magnetic particle imaging. *Appl. Phys. Lett.* **2011,** *98* (26), 3; (b) Ferguson, R. M.; Minard, K. R.; Krishnan, K. M., Optimization of nanoparticle core size for magnetic particle imaging. *Journal of Magnetism and Magnetic Materials* **2009,** *321* (10), 1548-1551.
83. Pineiro, Y.; Vargas, Z.; Rivas, J.; Lopez-Quintela, M. A., Iron Oxide Based Nanoparticles for Magnetic Hyperthermia Strategies in Biological Applications. *Eur. J. Inorg. Chem.* **2015,** (27), 4495-4509.
84. Lima-Tenorio, M. K.; Pineda, E. A. G.; Ahmad, N. M.; Fessi, H.; Elaissari, A., Magnetic nanoparticles: In vivo cancer diagnosis and therapy. *International Journal of Pharmaceutics* **2015,** *493* (1-2), 313-327.
85. Dutz, S.; Hergt, R., Magnetic particle hyperthermia-a promising tumour therapy? *Nanotechnology* **2014,** *25* (45), 28.
86. www.magforce.com.
87. Fantechi, E.; Innocenti, C.; Zanardelli, M.; Fittipaldi, M.; Falvo, E.; Carbo, M.; Shullani, V.; Mannelli, L. D.; Ghelardini, C.; Ferretti, A. M.; Ponti, A.; Sangregorio, C.; Ceci, P., A Smart Platform for Hyperthermia Application in Cancer Treatment: Cobalt-Doped Ferrite Nanoparticles Mineralized in Human Ferritin Cages. *Acs Nano* **2014,** *8* (5), 4705-4719.
88. Zhou, Z. G.; Sun, Y. A.; Shen, J. C.; Wei, J.; Yu, C.; Kong, B.; Liu, W.; Yang, H.; Yang, S. P.; Wang, W., Iron/iron oxide core/shell nanoparticles for magnetic targeting MRI and near-infrared photothermal therapy. *Biomaterials* **2014,** *35* (26), 7470-7478.
89. Caldorera-Moore, M. E.; Liechty, W. B.; Peppas, N. A., Responsive theranostic systems: integration of diagnostic imaging agents and responsive controlled release drug delivery carriers. *Acc Chem Res* **2011,** *44* (10), 1061-70.
90. Kohler, N.; Sun, C.; Fichtenholtz, A.; Gunn, J.; Fang, C.; Zhang, M. Q., Methotrexate-immobilized poly(ethylene glycol) magnetic nanoparticles for MR imaging and drug delivery. *Small* **2006,** *2* (6), 785-792.
91. Hsiao, M. H.; Mu, Q. X.; Stephen, Z. R.; Fang, C.; Zhang, M. Q., Hexanoyl-Chitosan-PEG Copolymer Coated Iron Oxide Nanoparticles for Hydrophobic Drug Delivery. *ACS Macro Lett.* **2015,** *4* (4), 403-407.
92. Chen, Q.; Ke, H. T.; Dai, Z. F.; Liu, Z., Nanoscale theranostics for physical stimulus-responsive cancer therapies. *Biomaterials* **2015,** *73*, 214-230.

93. Zou, P.; Yu, Y. K.; Wang, Y. A.; Zhong, Y. Q.; Welton, A.; Galban, C.; Wang, S. M.; Sun, D. X., Superparamagnetic Iron Oxide Nanotheranostics for Targeted Cancer Cell Imaging and pH-Dependent Intracellular Drug Release. *Mol. Pharm.* **2010,** *7* (6), 1974-1984.
94. Pourjavadi, A.; Hosseini, S. H.; Alizadeh, M.; Bennett, C., Magnetic pH-responsive nanocarrier with long spacer length and high colloidal stability for controlled delivery of doxorubicin. *Colloid Surf. B-Biointerfaces* **2014,** *116*, 49-54.
95. Kievit, F. M.; Wang, F. Y.; Fang, C.; Mok, H.; Wang, K.; Silber, J. R.; Ellenbogen, R. G.; Zhang, M. Q., Doxorubicin loaded iron oxide nanoparticles overcome multidrug resistance in cancer in vitro. *Journal of Controlled Release* **2011,** *152* (1), 76-83.
96. (a) Fang, C.; Kievit, F. M.; Veiseh, O.; Stephen, Z. R.; Wang, T. Z.; Lee, D. H.; Ellenbogen, R. G.; Zhang, M. Q., Fabrication of magnetic nanoparticles with controllable drug loading and release through a simple assembly approach. *Journal of Controlled Release* **2012,** *162* (1), 233-241; (b) Meenach, S. A.; Otu, C. G.; Anderson, K. W.; Hilt, J. Z., Controlled synergistic delivery of paclitaxel and heat from poly(beta-amino ester)/iron oxide-based hydrogel nanocomposites. *International Journal of Pharmaceutics* **2012,** *427* (2), 177-184.
97. (a) Chen, L. D.; Xue, Y. A.; Xia, X. Y.; Song, M. F.; Huang, J.; Zhang, H.; Yu, B.; Long, S. H.; Liu, Y. P.; Liu, L.; Huang, S. W.; Yu, F. Q., A redox stimuli-responsive superparamagnetic nanogel with chemically anchored DOX for enhanced anticancer efficacy and low systemic adverse effects. *J. Mat. Chem. B* **2015,** *3* (46), 8949-8962; (b) Zou, H.; Yuan, W. Z., Temperature- and redox-responsive magnetic complex micelles for controlled drug release. *J. Mat. Chem. B* **2015,** *3* (2), 260-269.
98. Estelrich, J.; Escribano, E.; Queralt, J.; Busquets, M. A., Iron Oxide Nanoparticles for Magnetically-Guided and Magnetically-Responsive Drug Delivery. *Int. J. Mol. Sci.* **2015,** *16* (4), 8070-8101.
99. Amstad, E.; Kohlbrecher, J.; Muller, E.; Schweizer, T.; Textor, M.; Reimhult, E., Triggered Release from Liposomes through Magnetic Actuation of Iron Oxide Nanoparticle Containing Membranes. *Nano Letters* **2011,** *11* (4), 1664-1670.
100. Xing, R. J.; Liu, G.; Zhu, J. H.; Hou, Y. L.; Chen, X. Y., Functional Magnetic Nanoparticles for Non-Viral Gene Delivery and MR Imaging. *Pharm. Res.* **2014,** *31* (6), 1377-1389.
101. Kievit, F. M.; Veiseh, O.; Fang, C.; Bhattarai, N.; Lee, D.; Ellenbogen, R. G.; Zhang, M. Q., Chlorotoxin Labeled Magnetic Nanovectors for Targeted Gene Delivery to Glioma. *Acs Nano* **2010,** *4* (8), 4587-4594.
102. Wang, K.; Kievit, F. M.; Jeon, M.; Silber, J. R.; Ellenbogen, R. G.; Zhang, M. Q., Nanoparticle-Mediated Target Delivery of TRAIL as Gene Therapy for Glioblastoma. *Adv. Healthc. Mater.* **2015,** *4* (17), 2719-2726.
103. (a) Veiseh, O.; Kievit, F. M.; Ellenbogen, R. G.; Zhang, M., Cancer cell invasion: treatment and monitoring opportunities in nanomedicine. *Adv. Drug Deliv. Rev.* **2011,** *63* (8), 582-96; (b) Kievit, F. M.; Zhang, M., Cancer nanotheranostics: improving imaging and therapy by targeted delivery across biological barriers. *Advanced materials* **2011,** *23* (36), H217-47; (c) Veiseh, O.; Gunn, J. W.; Zhang, M., Design and fabrication of magnetic nanoparticles for targeted drug delivery and imaging. *Adv Drug Deliv Rev* **2010,** *62* (3), 284-304.
104. Madabhushi, A.; Doyle, S.; Lee, G.; Basavanhally, A.; Monaco, J.; Masters, S.; Tomaszewski, J.; Feldman, M., Integrated diagnostics: a conceptual framework with examples. *Clin Chem Lab Med* **2010,** *48* (7), 989-98.

105. (a) Jain, R. K.; Stylianopoulos, T., Delivering nanomedicine to solid tumors. *Nat Rev Clin Oncol* **2010**; (b) Davis, M. E.; Chen, Z. G.; Shin, D. M., Nanoparticle therapeutics: an emerging treatment modality for cancer. *Nat Rev Drug Discov* **2008,** *7* (9), 771-82.
106. Patil, R.; Portilla-Arias, J.; Ding, H.; Inoue, S.; Konda, B.; Hu, J.; Wawrowsky, K. A.; Shin, P. K.; Black, K. L.; Holler, E.; Ljubimova, J. Y., Temozolomide Delivery to Tumor Cells by a Multifunctional Nano Vehicle Based on Poly(beta-L-malic acid). *Pharm Res* **2010**.
107. Mrugala, M. M.; Chamberlain, M. C., Mechanisms of disease: temozolomide and glioblastoma--look to the future. *Nat Clin Pract Oncol* **2008,** *5* (8), 476-86.
108. (a) Bobola, M. S.; Tseng, S. H.; Blank, A.; Berger, M. S.; Silber, J. R., Role of O6-methylguanine-DNA methyltransferase in resistance of human brain tumor cell lines to the clinically relevant methylating agents temozolomide and streptozotocin. *Clin Cancer Res* **1996,** *2* (4), 735-41; (b) Bobola, M. S.; Silber, J. R.; Ellenbogen, R. G.; Geyer, J. R.; Blank, A.; Goff, R. D., O6-methylguanine-DNA methyltransferase, O6-benzylguanine, and resistance to clinical alkylators in pediatric primary brain tumor cell lines. *Clin Cancer Res* **2005,** *11* (7), 2747-55; (c) Bobola, M. S.; Kolstoe, D. D.; Blank, A.; Silber, J. R., Minimally cytotoxic doses of temozolomide produce radiosensitization in human glioblastoma cells regardless of MGMT expression. *Mol Cancer Ther* **2010,** *9* (5), 1208-18.
109. (a) Silber, J. R.; Bobola, M. S.; Blank, A.; Schoeler, K. D.; Haroldson, P. D.; Huynh, M. B.; Kolstoe, D. D., The apurinic/apyrimidinic endonuclease activity of Ape1/Ref-1 contributes to human glioma cell resistance to alkylating agents and is elevated by oxidative stress. *Clin Cancer Res* **2002,** *8* (9), 3008-18; (b) Bobola, M. S.; Varadarajan, S.; Smith, N. W.; Goff, R. D.; Kolstoe, D. D.; Blank, A.; Gold, B.; Silber, J. R., Human glioma cell sensitivity to the sequence-specific alkylating agent methyl-lexitropsin. *Clin Cancer Res* **2007,** *13* (2 Pt 1), 612-20.
110. Quinn, J. A.; Jiang, S. X.; Reardon, D. A.; Desjardins, A.; Vredenburgh, J. J.; Rich, J. N.; Gururangan, S.; Friedman, A. H.; Bigner, D. D.; Sampson, J. H.; McLendon, R. E.; Herndon, J. E., 2nd; Walker, A.; Friedman, H. S., Phase II trial of temozolomide plus o6-benzylguanine in adults with recurrent, temozolomide-resistant malignant glioma. *J Clin Oncol* **2009,** *27* (8), 1262-7.
111. (a) Berg, S. L.; Gerson, S. L.; Godwin, K.; Cole, D. E.; Liu, L.; Balis, F. M., Plasma and cerebrospinal fluid pharmacokinetics of O6-benzylguanine and time course of peripheral blood mononuclear cell O6-methylguanine-DNA methyltransferase inhibition in the nonhuman primate. *Cancer Res.* **1995,** *55* (20), 4606-10; (b) Roy, S. K.; Gupta, E.; Dolan, M. E., Pharmacokinetics of O6-benzylguanine in rats and its metabolism by rat liver microsomes. *Drug Metab Dispos* **1995,** *23* (12), 1394-9.
112. (a) Boiardi, A.; Eoli, M.; Salmaggi, A.; Lamperti, E.; Botturi, A.; Solari, A.; Di Meco, F.; Broggi, G.; Silvani, A., Local drug delivery in recurrent malignant gliomas. *Neurol Sci* **2005,** *26* (1), s37-s39; (b) Wang, P. P.; Frazier, J.; Brem, H., Local drug delivery to the brain. *Adv. Drug Deliv. Rev.* **2002,** *54* (7), 987-1013.
113. Allhenn, D.; Shetab Boushehri, M. A.; Lamprecht, A., Drug delivery strategies for the treatment of malignant gliomas. *International Journal of Pharmaceutics* **2012,** *436* (1–2), 299-310.
114. Juratli, T. A.; Schackert, G.; Krex, D., Current status of local therapy in malignant gliomas — A clinical review of three selected approaches. *Pharmacology & Therapeutics* **2013,** *139* (3), 341-358.
115. Allard, E.; Passirani, C.; Benoit, J.-P., Convection-enhanced delivery of nanocarriers for the treatment of brain tumors. *Biomaterials* **2009,** *30* (12), 2302-2318.

116. Saito, R.; Krauze, M. T.; Noble, C. O.; Tamas, M.; Drummond, D. C.; Kirpotin, D. B.; Berger, M. S.; Park, J. W.; Bankiewicz, K. S., Tissue affinity of the infusate affects the distribution volume during convection-enhanced delivery into rodent brains: implications for local drug delivery. *Journal of neuroscience methods* **2006,** *154* (1-2), 225-32.
117. Silber, J. R.; Bobola, M. S.; Ghatan, S.; Blank, A.; Kolstoe, D. D.; Berger, M. S., O6-Methylguanine-DNA Methyltransferase Activity in Adult Gliomas: Relation to Patient and Tumor Characteristics. *Cancer Res.* **1998,** *58* (5), 1068-1073.
118. Blank, A.; Bobola, M. S.; Gold, B.; Varadarajan, S.; D. Kolstoe, D.; Meade, E. H.; Rabinovitch, P. S.; Loeb, L. A.; Silber, J. R., The Werner syndrome protein confers resistance to the DNA lesions N3-methyladenine and O6-methylguanine: implications for WRN function. *DNA Repair* **2004,** *3* (6), 629-638.
119. Burton, K., A study of the conditions and mechanism of the diphenylamine reaction for the colorimetric estimation of deoxyribonucleic acid. *The Biochemical journal* **1956,** *62* (2), 315-23.
120. Carlson, B. L.; Pokorny, J. L.; Schroeder, M. A.; Sarkaria, J. N., Establishment, maintenance and in vitro and in vivo applications of primary human glioblastoma multiforme (GBM) xenograft models for translational biology studies and drug discovery. *Current protocols in pharmacology / editorial board, S.J. Enna (editor-in-chief) ... [et al.]* **2011,** *Chapter 14*, Unit 14.16.
121. MacKay, J. A.; Deen, D. F.; Szoka Jr, F. C., Distribution in brain of liposomes after convection enhanced delivery; modulation by particle charge, particle diameter, and presence of steric coating. *Brain Research* **2005,** *1035* (2), 139-153.
122. Kim, B.; Han, G.; Toley, B. J.; Kim, C. K.; Rotello, V. M.; Forbes, N. S., Tuning payload delivery in tumour cylindroids using gold nanoparticles. *Nature nanotechnology* **2010,** *5* (6), 465-72.
123. (a) Zhou, L.; He, B.; Zhang, F., Facile One-Pot Synthesis of Iron Oxide Nanoparticles Cross-linked Magnetic Poly(vinyl alcohol) Gel Beads for Drug Delivery. *ACS Appl Mater Interfaces* **2012,** *4* (1), 192-9; (b) Luo, Z.; Cai, K.; Hu, Y.; Li, J.; Ding, X.; Zhang, B.; Xu, D.; Yang, W.; Liu, P., Redox-Responsive Molecular Nanoreservoirs for Controlled Intracellular Anticancer Drug Delivery Based on Magnetic Nanoparticles. *Advanced materials* **2011**; (c) Ge, J.; Neofytou, E.; Cahill, T. J.; Beygui, R. E.; Zare, R. N., Drug release from electric-field-responsive nanoparticles. *ACS nano* **2012,** *6* (1), 227-33.
124. Feener, E. P.; Shen, W. C.; Ryser, H. J., Cleavage of disulfide bonds in endocytosed macromolecules. A processing not associated with lysosomes or endosomes. *J Biol Chem* **1990,** *265* (31), 18780-5.
125. Veiseh, M.; Gabikian, P.; Bahrami, S. B.; Veiseh, O.; Zhang, M.; Hackman, R. C.; Ravanpay, A. C.; Stroud, M. R.; Kusuma, Y.; Hansen, S. J.; Kwok, D.; Munoz, N. M.; Sze, R. W.; Grady, W. M.; Greenberg, N. M.; Ellenbogen, R. G.; Olson, J. M., Tumor paint: a chlorotoxin:Cy5.5 bioconjugate for intraoperative visualization of cancer foci. *Cancer Res.* **2007,** *67* (14), 6882-8.
126. Kesavan, K.; Ratliff, J.; Johnson, E. W.; Dahlberg, W.; Asara, J. M.; Misra, P.; Frangioni, J. V.; Jacoby, D. B., Annexin A2 is a molecular target for TM601, a peptide with tumor-targeting and anti-angiogenic effects. *J Biol Chem* **2010,** *285* (7), 4366-74.
127. (a) Soroceanu, L.; Gillespie, Y.; Khazaeli, M. B.; Sontheimer, H., Use of chlorotoxin for targeting of primary brain tumors. *Cancer Res.* **1998,** *58* (21), 4871-4879; (b) Lyons, S. A.;

O'Neal, J.; Sontheimer, H., Chlorotoxin, a scorpion-derived peptide, specifically binds to gliomas and tumors of neuroectodermal origin. *Glia* **2002,** *39* (2), 162-73.
128. Veiseh, O.; Gunn, J. W.; Kievit, F. M.; Sun, C.; Fang, C.; Lee, J. S.; Zhang, M., Inhibition of tumor-cell invasion with chlorotoxin-bound superparamagnetic nanoparticles. *Small* **2009,** *5* (2), 256-64.
129. Deshane, J.; Garner, C. C.; Sontheimer, H., Chlorotoxin inhibits glioma cell invasion *via* matrix metalloproteinase-2. *J Biol Chem* **2003,** *278* (6), 4135-44.
130. Silber, J. R.; Bobola, M. S.; Blank, A.; Chamberlain, M. C., O6-Methylguanine-DNA methyltransferase in glioma therapy: Promise and problems. *Biochimica et Biophysica Acta (BBA) - Reviews on Cancer* (0).
131. Frosina, G., DNA repair and resistance of gliomas to chemotherapy and radiotherapy. *Mol Cancer Res* **2009,** *7* (7), 989-99.
132. Carlson, B. L.; Grogan, P. T.; Mladek, A. C.; Schroeder, M. A.; Kitange, G. J.; Decker, P. A.; Giannini, C.; Wu, W.; Ballman, K. A.; James, C. D.; Sarkaria, J. N., Radiosensitizing Effects of Temozolomide Observed in vivo only in a Subset of O6-Methylguanine-DNA Methyltransferase Methylated Glioblastoma Multiforme Xenografts. *International Journal of Radiation Oncology*Biology*Physics* **2009,** *75* (1), 212-219.
133. Frederick, L.; Wang, X. Y.; Eley, G.; James, C. D., Diversity and frequency of epidermal growth factor receptor mutations in human glioblastomas. *Cancer Res* **2000,** *60* (5), 1383-7.
134. Pegg, A. E., Mammalian O6-alkylguanine-DNA alkyltransferase: regulation and importance in response to alkylating carcinogenic and therapeutic agents. *Cancer Res* **1990,** *50* (19), 6119-29.
135. (a) Mardor, Y.; Rahav, O.; Zauberman, Y.; Lidar, Z.; Ocherashvilli, A.; Daniels, D.; Roth, Y.; Maier, S. E.; Orenstein, A.; Ram, Z., Convection-enhanced drug delivery: increased efficacy and magnetic resonance image monitoring. *Cancer Res* **2005,** *65* (15), 6858-63; (b) Vogelbaum, M. A., Convection enhanced delivery for treating brain tumors and selected neurological disorders: symposium review. *J Neurooncol* **2007,** *83* (1), 97-109.
136. Juratli, T. A.; Schackert, G.; Krex, D., Current status of local therapy in malignant gliomas--a clinical review of three selected approaches. *Pharmacol Ther* **2013,** *139* (3), 341-58.
137. (a) Moore, A.; Marecos, E.; Bogdanov, A., Jr.; Weissleder, R., Tumoral distribution of long-circulating dextran-coated iron oxide nanoparticles in a rodent model. *Radiology* **2000,** *214* (2), 568-74; (b) Medarova, Z.; Pham, W.; Farrar, C.; Petkova, V.; Moore, A., In vivo imaging of siRNA delivery and silencing in tumors. *Nat Med* **2007,** *13* (3), 372-7.
138. Warren, K. E.; Gururangan, S.; Geyer, J. R.; McLendon, R. E.; Poussaint, T. Y.; Wallace, D.; Balis, F. M.; Berg, S. L.; Packer, R. J.; Goldman, S.; Minturn, J. E.; Pollack, I. F.; Boyett, J. M.; Kun, L. E., A phase II study of O6-benzylguanine and temozolomide in pediatric patients with recurrent or progressive high-grade gliomas and brainstem gliomas: a Pediatric Brain Tumor Consortium study. *J. Neuro-Oncol.* **2012,** *106* (3), 643-9.
139. NCI Common Terminology Criteria for Adverse Events V3.0. http://ctep.cancer.gov/ProtocolDevelopment/electronic_applications/docs/ctcaev3.pdf (accessed March 2, 2012).
140. Sarkaria, J. N.; Kitange, G. J.; James, C. D.; Plummer, R.; Calvert, H.; Weller, M.; Wick, W., Mechanisms of chemoresistance to alkylating agents in malignant glioma. *Clin. Cancer Res.* **2008,** *14* (10), 2900-2908.

141. (a) Krex, D.; Klink, B.; Hartmann, C.; von Deimling, A.; Pietsch, T.; Simon, M.; Sabel, M.; Steinbach, J. P.; Heese, O.; Reifenberger, G.; Weller, M.; Schackert, G.; German Glioma, N., Long-term survival with glioblastoma multiforme. *Brain* **2007,** *130*, 2596-2606; (b) Stupp, R.; Mason, W. P.; van den Bent, M. J.; Weller, M.; Fisher, B.; Taphoorn, M. J. B.; Belanger, K.; Brandes, A. A.; Marosi, C.; Bogdahn, U.; Curschmann, J.; Janzer, R. C.; Ludwin, S. K.; Gorlia, T.; Allgeier, A.; Lacombe, D.; Cairncross, J. G.; Eisenhauer, E.; Mirimanoff, R. O.; Van Den Weyngaert, D.; Kaendler, S.; Krauseneck, P.; Vinolas, N.; Villa, S.; Wurm, R. E.; Maillot, M. H. B.; Spagnolli, F.; Kantor, G.; Malhaire, J. P.; Renard, L.; De Witte, O.; Scandolaro, L.; Vecht, C. J.; Maingon, P.; Lutterbach, J.; Kobierska, A.; Bolla, M.; Souchon, R.; Mitine, C.; Tzuk-Shina, T.; Kuten, A.; Haferkamp, G.; de Greve, J.; Priou, F.; Menten, J.; Rutten, I.; Clavere, P.; Malmstrom, A.; Jancar, B.; Newlands, E.; Pigott, K.; Twijnstra, A.; Chinot, O.; Reni, M.; Boiardi, A.; Fabbro, M.; Campone, M.; Bozzino, J.; Frenay, M.; Gijtenbeek, J.; Brandes, A. A.; Delattre, J. Y.; Bogdahn, U.; De Paula, U.; van den Bent, M. J.; Hanzen, C.; Pavanato, G.; Schraub, S.; Pfeffer, R.; Soffietti, R.; Weller, M.; Kortmann, R. D.; Taphoorn, M.; Torrecilla, J. L.; Marosi, C.; Grisold, W.; Huget, P.; Forsyth, P.; Fulton, D.; Kirby, S.; Wong, R.; Fenton, D.; Fisher, B.; Cairncross, G.; Whitlock, P.; Belanger, K.; Burdette-Radoux, S.; Gertler, S.; Saunders, S.; Laing, K.; Siddiqui, J.; Martin, L. A.; Gulavita, S.; Perry, J.; Mason, W.; Thiessen, B.; Pai, H.; Alam, Z. Y.; Eisenstat, D.; Mingrone, W.; Hofer, S.; Pesce, G.; Curschmann, J.; Dietrich, P. Y.; Stupp, R.; Mirimanoff, R. O.; Thum, P.; Baumert, B.; Ryan, G.; European Org Res Treatment Canc, B., Radiotherapy plus concomitant and adjuvant temozolomide for glioblastoma. *New England Journal of Medicine* **2005,** *352* (10), 987-996.

142. Chiarelli, P. A.; Kievit, F. M.; Zhang, M.; Ellenbogen, R. G., Bionanotechnology and the future of glioma. *Surgical neurology international* **2015,** *6* (Suppl 1), S45-58.

143. Stephen, Z. R.; Kievit, F. M.; Veiseh, O.; Chiarelli, P. A.; Fang, C.; Wang, K.; Hatzinger, S. J.; Ellenbogen, R. G.; Silber, J. R.; Zhang, M. Q., Redox-Responsive Magnetic Nanoparticle for Targeted Convection-Enhanced Delivery of O-6-Benzylguanine to Brain Tumors. *Acs Nano* **2014,** *8* (10), 10383-10395.

144. (a) Hamblett, K. J.; Senter, P. D.; Chace, D. F.; Sun, M. M.; Lenox, J.; Cerveny, C. G.; Kissler, K. M.; Bernhardt, S. X.; Kopcha, A. K.; Zabinski, R. F.; Meyer, D. L.; Francisco, J. A., Effects of drug loading on the antitumor activity of a monoclonal antibody drug conjugate. *Clin Cancer Res* **2004,** *10* (20), 7063-70; (b) Chu, K. S.; Schorzman, A. N.; Finniss, M. C.; Bowerman, C. J.; Peng, L.; Luft, J. C.; Madden, A. J.; Wang, A. Z.; Zamboni, W. C.; DeSimone, J. M., Nanoparticle drug loading as a design parameter to improve docetaxel pharmacokinetics and efficacy. *Biomaterials* **2013,** *34* (33), 8424-9.

145. (a) Cheng, C.; Jiang-Ling, Z.; Xue, H.; Fei, S.; Xiu-Li, W.; Yu-Zhong, W., A prodrug strategy based on chitosan for efficient intracellular anticancer drug delivery. *Nanotechnology* **2014,** *25* (25), 255101; (b) Duan, X.; Xiao, J.; Yin, Q.; Zhang, Z.; Yu, H.; Mao, S.; Li, Y., Smart pH-Sensitive and Temporal-Controlled Polymeric Micelles for Effective Combination Therapy of Doxorubicin and Disulfiram. *ACS Nano* **2013,** *7* (7), 5858-5869; (c) Xiong, X.-B.; Lavasanifar, A., Traceable Multifunctional Micellar Nanocarriers for Cancer-Targeted Co-delivery of MDR-1 siRNA and Doxorubicin. *ACS Nano* **2011,** *5* (6), 5202-5213; (d) Yang, X.; Grailer, J. J.; Rowland, I. J.; Javadi, A.; Hurley, S. A.; Matson, V. Z.; Steeber, D. A.; Gong, S., Multifunctional Stable and pH-Responsive Polymer Vesicles Formed by Heterofunctional Triblock Copolymer for Targeted Anticancer Drug Delivery and Ultrasensitive MR Imaging. *ACS Nano* **2010,** *4* (11), 6805-6817.

146. Faure, A.-C.; Dufort, S.; Josserand, V.; Perriat, P.; Coll, J.-L.; Roux, S.; Tillement, O., Control of the in vivo Biodistribution of Hybrid Nanoparticles with Different Poly(ethylene glycol) Coatings. *Small* **2009,** *5* (22), 2565-2575.
147. Willis, A. L.; Turro, N. J.; O'Brien, S., Spectroscopic characterization of the surface of iron oxide nanocrystals. *Chem. Mat.* **2005,** *17* (24), 5970-5975.
148. Korringa, J.; Seevers, D. O.; Torrey, H. C., THEORY OF SPIN PUMPING AND RELAXATION IN SYSTEMS WITH A LOW CONCENTRATION OF ELECTRON SPIN RESONANCE CENTERS. *Physical Review* **1962,** *127* (4), 1143-&.
149. Park, K., Facing the Truth about Nanotechnology in Drug Delivery. *Acs Nano* **2013,** *7* (9), 7442-7447.
150. (a) Hwang, A. A.; Lee, B. Y.; Clemens, D. L.; Dillon, B. J.; Zink, J. I.; Horwitz, M. A., pH-Responsive Isoniazid-Loaded Nanoparticles Markedly Improve Tuberculosis Treatment in Mice. *Small* **2015,** *11* (38), 5066-78; (b) Ruan, S.; He, Q.; Gao, H., Matrix metalloproteinase triggered size-shrinkable gelatin-gold fabricated nanoparticles for tumor microenvironment sensitive penetration and diagnosis of glioma. *Nanoscale* **2015,** *7* (21), 9487-96.
151. (a) Dirksen, A.; Dirksen, S.; Hackeng, T. M.; Dawson, P. E., Nucleophilic catalysis of hydrazone formation and transimination: implications for dynamic covalent chemistry. *J Am Chem Soc* **2006,** *128* (49), 15602-3; (b) Kalia, J.; Raines, R. T., Hydrolytic stability of hydrazones and oximes. *Angewandte Chemie (International ed. in English)* **2008,** *47* (39), 7523-6; (c) Kool, E. T.; Park, D. H.; Crisalli, P., Fast hydrazone reactants: electronic and acid/base effects strongly influence rate at biological pH. *J Am Chem Soc* **2013,** *135* (47), 17663-6.
152. Stephen, Z. R.; Kievit, F. M.; Zhang, M. Q., Magnetite nanoparticles for medical MR imaging. *Mater. Today* **2011,** *14* (7-8), 330-338.
153. Kievit, F. M.; Zhang, M., Surface engineering of iron oxide nanoparticles for targeted cancer therapy. *Acc Chem Res* **2011,** *44* (10), 853-62.
154. Kievit, F. M.; Zhang, M., Cancer nanotheranostics: improving imaging and therapy by targeted delivery across biological barriers. *Advanced materials* **2011,** *23* (36), H217-47.
155. Hermanson, G. T., *Bioconjugate Techniques*. 2nd ed.; Elsevier Inc.: Oxford UK, 2008.
156. Karpishin, T. B.; Gebhard, M. S.; Solomon, E. I.; Raymond, K. N., SPECTROSCOPIC STUDIES OF THE ELECTRONIC-STRUCTURE OF IRON(III) TRIS(CATECHOLATES). *Journal of the American Chemical Society* **1991,** *113* (8), 2977-2984.
157. (a) Amstad, E.; Gillich, T.; Bilecka, I.; Textor, M.; Reimhult, E., Ultrastable Iron Oxide Nanoparticle Colloidal Suspensions Using Dispersants with Catechol-Derived Anchor Groups. *Nano Letters* **2009,** *9* (12), 4042-4048; (b) Saville, S. L.; Stone, R. C.; Qi, B.; Mefford, O. T., Investigation of the stability of magnetite nanoparticles functionalized with catechol based ligands in biological media. *Journal of Materials Chemistry* **2012,** *22* (47), 24909-24917; (c) Mondini, S.; Drago, C.; Ferretti, A. M.; Puglisi, A.; Ponti, A., Colloidal stability of iron oxide nanocrystals coated with a PEG-based tetra-catechol surfactant. *Nanotechnology* **2013,** *24* (10).
158. Stephen, Z. R.; Kievit, F. M.; Veiseh, O.; Chiarelli, P. A.; Fang, C.; Wang, K.; Hatzinger, S. J.; Ellenbogen, R. G.; Silber, J. R.; Zhang, M., Redox-responsive magnetic nanoparticle for targeted convection-enhanced delivery of O6-benzylguanine to brain tumors. *ACS Nano* **2014,** *8* (10), 10383-95.

159. Kievit, F. M.; Veiseh, O.; Bhattarai, N.; Fang, C.; Gunn, J. W.; Lee, D.; Ellenbogen, R. G.; Olson, J. M.; Zhang, M. Q., PEI-PEG-Chitosan-Copolymer-Coated Iron Oxide Nanoparticles for Safe Gene Delivery: Synthesis, Complexation, and Transfection. *Adv. Funct. Mater.* **2009,** *19* (14), 2244-2251.
160. Na, H. B.; Palui, G.; Rosenberg, J. T.; Ji, X.; Grant, S. C.; Mattoussi, H., Multidentate Catechol-Based Polyethylene Glycol Oligomers Provide Enhanced Stability and Biocompatibility to Iron Oxide Nanoparticies. *Acs Nano* **2012,** *6* (1), 389-399.
161. Smolensky, E. D.; Park, H. Y. E.; Berquo, T. S.; Pierre, V. C., Surface functionalization of magnetic iron oxide nanoparticles for MRI applications - effect of anchoring group and ligand exchange protocol. *Contrast Media Mol. Imaging* **2011,** *6* (4), 189-199.
162. Yuen, A. K. L.; Hutton, G. A.; Masters, A. F.; Maschmeyer, T., The interplay of catechol ligands with nanoparticulate iron oxides. *Dalton Transactions* **2012,** *41* (9), 2545-2559.
163. (a) Borges, R. P.; Guichard, W.; Lunney, J. G.; Coey, J. M. D.; Ott, F., Magnetic and electric "dead" layers in (La0.7Sr0.3)MnO3 thin films. *J. Appl. Phys.* **2001,** *89* (7), 3868-3873; (b) Oguz, K.; Jivrajka, P.; Venkatesan, M.; Feng, G.; Coey, J. M. D., Magnetic dead layers in sputtered Co(40)Fe(40)B(20) films. *J. Appl. Phys.* **2008,** *103* (7), 3.
164. Nagesha, D. K.; Plouffe, B. D.; Phan, M.; Lewis, L. H.; Sridhar, S.; Murthy, S. K., Functionalization-induced improvement in magnetic properties of Fe3O4 nanoparticles for biomedical applications. *J. Appl. Phys.* **2009,** *105* (7), 3.
165. Behr, J. P., The proton sponge: A trick to enter cells the viruses did not exploit. *Chimia* **1997,** *51* (1-2), 34-36.
166. Takae, S.; Miyata, K.; Oba, M.; Ishii, T.; Nishiyama, N.; Itaka, K.; Yamasaki, Y.; Koyama, H.; Kataoka, K., PEG-detachable polyplex micelles based on disulfide-linked block catiomers as bioresponsive nonviral gene vectors. *Journal of the American Chemical Society* **2008,** *130* (18), 6001-6009.